NASA/TM-2009-215766

Development of Methods to Predict the Effects of Test Media in Ground-Based Propulsion Testing

J. Philip Drummond, Paul M. Danehy, Richard L. Gaffney, Jr., Peter A. Parker, and Sarah A. Tedder
NASA Langley Research Center, Hampton, Virginia

Harsha K. Chelliah
University of Virginia, Charlottesville, Virginia

Andrew D. Cutler and Daniel Bivolaru
The George Washington University, Newport News, Virginia

Peyman Givi
University of Pittsburgh, Pittsburgh, Pennsylvania

Hassan A. Hassan
North Carolina State University, Raleigh, North Carolina

June 2009

NASA STI Program . . . in Profile

Since its founding, NASA has been dedicated to the advancement of aeronautics and space science. The NASA scientific and technical information (STI) program plays a key part in helping NASA maintain this important role.

The NASA STI program operates under the auspices of the Agency Chief Information Officer. It collects, organizes, provides for archiving, and disseminates NASA's STI. The NASA STI program provides access to the NASA Aeronautics and Space Database and its public interface, the NASA Technical Report Server, thus providing one of the largest collections of aeronautical and space science STI in the world. Results are published in both non-NASA channels and by NASA in the NASA STI Report Series, which includes the following report types:

- TECHNICAL PUBLICATION. Reports of completed research or a major significant phase of research that present the results of NASA programs and include extensive data or theoretical analysis. Includes compilations of significant scientific and technical data and information deemed to be of continuing reference value. NASA counterpart of peer-reviewed formal professional papers, but having less stringent limitations on manuscript length and extent of graphic presentations.

- TECHNICAL MEMORANDUM. Scientific and technical findings that are preliminary or of specialized interest, e.g., quick release reports, working papers, and bibliographies that contain minimal annotation. Does not contain extensive analysis.

- CONTRACTOR REPORT. Scientific and technical findings by NASA-sponsored contractors and grantees.

- CONFERENCE PUBLICATION. Collected papers from scientific and technical conferences, symposia, seminars, or other meetings sponsored or co-sponsored by NASA.

- SPECIAL PUBLICATION. Scientific, technical, or historical information from NASA programs, projects, and missions, often concerned with subjects having substantial public interest.

- TECHNICAL TRANSLATION. English-language translations of foreign scientific and technical material pertinent to NASA's mission.

Specialized services also include creating custom thesauri, building customized databases, and organizing and publishing research results.

For more information about the NASA STI program, see the following:

- Access the NASA STI program home page at *http://www.sti.nasa.gov*

- E-mail your question via the Internet to help@sti.nasa.gov

- Fax your question to the NASA STI Help Desk at 443-757-5803

- Phone the NASA STI Help Desk at 443-757-5802

- Write to:
  NASA STI Help Desk
  NASA Center for AeroSpace Information
  7115 Standard Drive
  Hanover, MD 21076-1320

NASA/TM-2009-215766

Development of Methods to Predict the Effects of Test Media in Ground-Based Propulsion Testing

J. Philip Drummond, Paul M. Danehy, Richard L. Gaffney, Jr., Peter A. Parker, and Sarah A. Tedder
NASA Langley Research Center, Hampton, Virginia

Harsha K. Chelliah
University of Virginia, Charlottesville, Virginia

Andrew D. Cutler and Daniel Bivolaru
The George Washington University, Newport News, Virginia

Peyman Givi
University of Pittsburgh, Pittsburgh, Pennsylvania

Hassan A. Hassan
North Carolina State University, Raleigh, North Carolina

National Aeronautics and
Space Administration

Langley Research Center
Hampton, Virginia 23681-2199

June 2009

Acknowledgments

The authors express their appreciation to Mr. George Rumford, Program Manager of the Defense Test Resource Management Center (DTRMC) Test and Evaluation/Science and Technology (T&E/S&T) Program, for funding this effort under the Hypersonic Test Focus Area. The authors also express their appreciation to the NASA Fundamental Aerodynamics Program, Hypersonic Project, Propulsion and Experimental Capabilities Disciplines for support and funding during the final two years of this program.

Available from:

NASA Center for AeroSpace Information
7115 Standard Drive
Hanover, MD 21076-1320
443-757-5802

Abstract

This report discusses work that began in mid-2004 sponsored by the Office of the Secretary of Defense (OSD) Test & Evaluation/Science & Technology (T&E/S&T) Program. The work was undertaken to improve the state of the art of CFD capabilities for predicting the effects of the test media on the flameholding characteristics in scramjet engines. The program had several components including the development of advanced algorithms and models for simulating engine flowpaths as well as a fundamental experimental and diagnostic development effort to support the formulation and validation of the mathematical models. This report provides details of the completed work, involving the development of phenomenological models for Reynolds averaged Navier-Stokes codes, large-eddy simulation techniques and reduced-kinetics models. Experiments that provided data for the modeling efforts are also described, along with with the associated nonintrusive diagnostics used to collect the data.

Contents

1 Project Introduction

The design and development of a scramjet engine is accomplished with several levels of analytic tools, ground-based testing and finally flight. To achieve the flight conditions encountered by a scramjet propelled hypersonic vehicle in a ground facility, the test gas must be heated to high temperatures before being introduced into the engine flowpath. One method for heating the test gas involves mixing fuel, for example hydrogen or butane, with the air and allowing it to combust in a facility heater prior to use. Prior to being burned, additional oxygen is added to the test gas to make up for the oxygen depleted during combustion. As a consequence of chemical reaction, combustion products, or vitiates, are also added to the test gas. These products can affect the performance of the engine being tested by altering the chemical reactions taking place in the engine. Vitiates can change the rates of chemical reactions or, in the extreme, the ability of the reaction to persist in the engine combustor. In order to translate the performance of an engine in a ground based facility to the expected performance in flight, the effects of facility vitiates must be determined.

This report discusses work that began in mid-2004, sponsored by the Office of the Secretary of Defense (OSD) Test & Evaluation/Science & Technology (T&E/S&T) Program. Contributors included the NASA Langley Research Center, George Washington University, North Carolina State University, the University of Pittsburgh, and the University of Virginia. The purpose of the work was to improve the state of the art of Computational Fluid Dynamics (CFD) capabilities for predicting the effects of the test media on the flameholding characteristics in scramjet engine combustors. The program had several components including the development of advanced algorithms and models for simulating engine flowpaths as well as a fundamental experimental and diagnostic development effort to support the formulation and validation of the mathematical models. This report provides details of completed work involving the development of phenomenological models for Reynolds averaged Navier-Stokes codes, large-eddy simulation techniques, reduced-kinetics models, and two experiments with the associated nonintrusive diagnostics that provided data for the modeling efforts. A detailed description of each of these activities along with the results determined by the research are given in the following seven sections of this final project report.

2 Supersonic Combusting Jet Experiments for Code Development and Validation

Computational fluid dynamics methods based on the Reynolds averaged Navier- Stokes (RANS) equations are extensively employed in the design of hypersonic airbreathing engines. A fundamental weakness in these methods is the accurate mathematical modeling of turbulence and turbulence-combustion interactions. This section of the report along with sections 4 and 5, which describe the use of the combined dual pump CARS and the newly developed interferometric Rayleigh scattering optical system, discuss the work to acquire time-accurate turbulence and mixing data to aid calibration and verification of current turbulence models [1].

This test program consisted of a pilot laboratory-scale experiment used to develop the optical system and data acquisition techniques, and a significantly larger experiment to acquire the necessary turbulence data. The flow is an axially-symmetric, supersonic, combusting, free jet that provides good optical access, consisting of a central jet of hot vitiated air and a coflow jet of hydrogen or ethylene fuel. In this section the development of both experiments is described. Facility and flow visualization data are presented for various types of flames, including the flames selected for detailed study with the CARS/Rayleigh optical

techniques.

2.1 Introduction

Computational fluid dynamics (CFD) methods that employ the Reynolds-averaged Navier-Stokes (RANS) equations are widely used in the design and analysis of hypersonic airbreathing engine flow paths. These methods require models for various statistical properties of the turbulent fluctuations in flow variables. While models for the Reynolds shear stress are relatively well developed for low speed flows, these models are less well-developed for high speed, and new models are required for turbulent transport of chemical species and energy (Reynolds heat and mass flux), as well as for turbulence-chemistry interactions [2].

Turbulence models are mathematical approximations to very complex physical processes, and require experimental data for developing the form and for setting the constants. Due to experimental difficulties, high quality data suitable for this development are lacking in supersonic combustion. Available data sets are limited to a subset of the important variables (temperature, composition, and velocity) and data sets that include accurate Reynolds stress, heat and mass fluxes do not exist. Even in subsonic reacting flows the simultaneous acquisition of temperature, composition, and velocity is experimentally very challenging. The situation is further complicated in supersonic flows where pressure becomes a variable, where experimental facilities become much more difficult and expensive to build and operate, and where often hostile environments are encountered (noise, heat, safety issues, etc.).

At NASA Langley Research Center, a sustained effort has been made to obtain experimental data for supersonic combustion model development. Data sets have been acquired in a H_2 fueled supersonic combustor using the coherent anti-Stokes Raman spectroscopy (CARS) technique [3] and the dual-pump CARS technique, originally developed by Robert Lucht and coworkers [4, 5] and extended at Langley [6, 7]. The standard CARS technique is used to acquire temperature only whereas the dual-pump CARS technique is used to acquire both temperature and composition. Both mean flow and turbulence statistics (variances and covariances) were derived from the data, although the uncertainty in the latter was high due both to instrument error and to the small number of measurements with which to base the statistics on. Other work includes Goyne, et al. [8] who report measurements of mean streamwise velocity in a dual-mode scramjet using the particle-imaging velocimetry technique. International work in this area includes measurements in scramjet combustors conducted at ONERA (France) and DLR (Germany) using CARS [9], and other non-intrusive techniques.

Under sponsorship of the Office of the Secretary of Defense, and NASAs Fundamental Aeronautics Program, a program of experimental research has been undertaken to provide data suitable for model development and validation in both H_2 and hydrocarbon fueled supersonic combustors [10–12]. Of particular interest is the development of models able to predict combustion and flame holding for scramjet/ramjet engines both in flight and tested in ground test facilities, and to enable ground test data to be extrapolated to flight. In these ground test facilities, the air entering the combustor is often replaced by vitiated air, which is constituted to the same total sensible enthalpy as the air entering the engine in flight (in the frame of reference of the vehicle). Vitiated air is the product of combustion in air of either H_2 or a hydrocarbon that is enriched with O_2 to the same content (by mole or by mass) as standard air. This product approximately reproduces the pressure rise and thrust of the engine in air, but may not reproduce flame holding and other properties involving chemical kinetics in the engine flow field. The program includes instrumentation development, experimental facility and test technique development, data acquisition and analysis.

The previously developed dual-pump CARS system provides simultaneous instantaneous measurements of temperature and composition at a single point at a rate of 20 Hz. A new

technique, interferometric Rayleigh scattering (IRS), has been developed to meet the need for simultaneous velocity measurements [13–16]. This technique collects Rayleigh scattered light from one of the CARS laser beams and by spectral analysis to find Doppler shift, measures velocity in the same instant as the CARS measurement. Taken together, these measurements can be used to compute many of the statistical quantities of interest to the modeler, including terms relating to turbulent transport of species and energy. Experiments have also been developed to provide suitable flows for study. An axisymmetric free jet was selected. This flow is geometrically simple, minimizing the number of spatial measurement points required to define the flow, and is accessible to optical instrumentation. There are several possible configurations: (i) a supersonic jet of fuel into stagnant air or low speed air coflow, (ii) a supersonic jet of fuel into supersonic air coflow, or (iii) a supersonic jet of air into low speed fuel coflow. Because of the requirement to study a high speed flow, one or both of the flows must be heated to ensure combustion. In some earlier work, a laboratory burner was developed to provide a supersonic jet of combustion heated (vitiated) air coflow and a sonic jet of H_2 (or other fuel) at the axis - similar to (ii) above [17]. Such a flow seemed ideal, but encountered many practical difficulties. The nozzle was not designed for uniform flow at the exit and consequently the jet contained a diamond shock system, forming Mach disks at the axis where the jet of H_2 was located. Mixing and combustion was dominated by these shocks. Additionally, the hardware was complex, and it was hard to maintain geometrical fidelity (the central jet of H_2 often was not on axis).

For the present research the flow is a heated sonic or supersonic center jet into an unheated low speed coflow. This flow was chosen since the apparatus to produce it is simpler than for a heated coflow. The center jet comprises the products of combustion of H_2, and can (at least in principle) be constituted to have excess unreacted H_2 or to have excess O_2 (i.e., be vitiated air). The coflow is low speed, unheated and can be either fuel or air. In either case the center jet is uniform and pressure matched to the atmosphere at the nozzle exit to avoid formation of shock waves in the external flow. Early computational studies focused on cases with a H_2 rich center jet, and designs were developed to ensure flame attachment at the nozzle exit [18]. Subsequently, studies focused on cases in which the center jet was vitiated air and the coflow was a fuel, either H_2 or C_2H_4, or a mixture of these fuels. This change was, in part, because of an interest in studying combustion of a hydrocarbon fuel; if a hydrocarbon had been reacted to form the center jet flow, and the flow was fuel rich, then there would have been sooting which would have made the flow more complex than desired and interfered with the optical diagnostics. Operation with vitiated air is also the normal mode of operation of one of the facilities used in the experiments.

The main flow feature of interest, for the purposes of CFD model development, is the developing mixing layer between the center jet, the coflow and the surrounding ambient air, where combustion takes place. This layer thickness varies from near zero at the nozzle exit to roughly a nozzle exit diameter in thickness far downstream. In order to adequately resolve the turbulence in the layer, the measurement volume should probably be less than 0.1, the thickness of the mixing layer. Turbulence fluctuations exist at much smaller scales than this, but the majority of the turbulence stress, and heat and mass flux are produced by the larger scales of the flow. The smaller scales are important in turbulent combustion since they are responsible for mixing of fuel and air to the molecular level, but cannot be resolved in a high speed (hence high Reynolds number) flow with the instrumentation available to us. Since the CARS measurement volume is approximately 1.5 mm long, this crude analysis suggests that the nozzle exit needs to be at least 15 mm diameter to resolve the turbulence far downstream, and much greater to resolve it near the nozzle exit.

Two different sizes of experimental hardware were developed. The first hardware was developed for the laboratory and is the largest that can safely be operated in that environment. This laboratory burner has a center jet nozzle exit diameter of 10 mm and was used to conduct preliminary flame studies and to verify the CARS-IRS techniques in the laboratory.

The capstone experiments of this project, the large-scale facility tests, were performed in NASA Langleys Direct Connect Supersonic Combustion Test Facility (DCSCTF) [19], with a flow field that is essentially the same, but the nozzle exit diameter is 63.5 mm. This report briefly describes the laboratory burner and some results in that burner, but is focused on the design, facility measurements and flame visualization studies of the large scale tests. Section 4 of this report describes the CARS-IRS measurements in this facility.

2.2 Laboratory Experiment

Figure 1a shows the laboratory-scale burner, sectioned along the axis, with bolts, gas supply lines, spark plug and other fittings not shown. It consists of a water-cooled combustion chamber, an annulus and a nozzle. The nozzle, with 10 mm exit diameter, is interchangeable; convergent ($M \leq 1$), or supersonic convergent-divergent (M =1.6 and M =2), designed using the method of characteristics. An annular coflow nozzle is formed between the nozzle and the annulus. The coflow nozzle is convergent with exit width (in the radial direction) of 1 mm. The annular base at the exit, between the central jet and coflow, is normal to the axis and 3 mm wide. Reactants at ambient temperature are delivered to the burner by the injector, a central tube through which gaseous fuel flows, and a concentric passage through which a mixture of O_2 (or sometimes N_2) with air flows. Various combinations of H_2 or C_2H_4 fuel, air, and O_2 are reacted in the combustion chamber to provide hot products at various temperatures and compositions (dependent on flow rates). The coflow may be of unheated fuel (H_2 or C_2H_4) or air. The resulting coaxial jet flow will mix and may react. If reaction does take place, then the flame may be held at the burner or stand off from it, depending on temperature and Mach number. Figure 1b is an image of the burner near the nozzle exit during operation showing a Mach 2 jet of vitiated air (air coflow, so no flame) and the laser beams of the CARS-Rayleigh system.

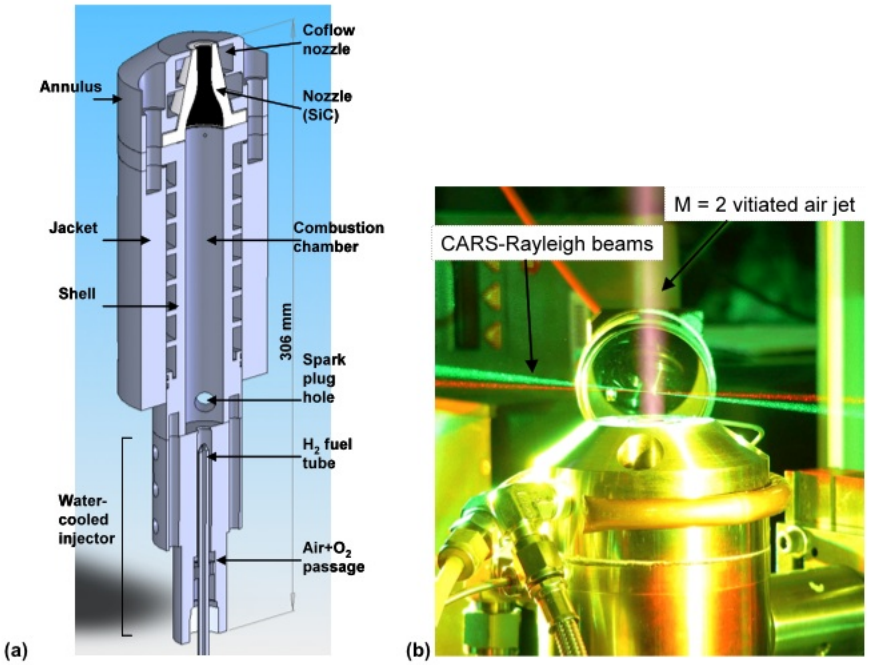

Figure 1. Laboratory scale burner: (a) vertical section view, (b) burner in operation showing laser beams (but no coflow flame).

Reference 21 provides a detailed description and analysis of this burner, and visualization studies of the various flames. Edge attached flames were the result in cases with excess O_2 in the hot center jet (vitiated air) and H_2 coflow: these flames started at the interface between the ambient air and the H_2 coflow very close to the nozzle exit, and extended downstream. Flames detached from the nozzle exit if the centerjet Mach number was raised from 1.6 to 2. Base attached flames were the result in cases with excess H_2 in the center jet and air coflow: these flames started in the recirculating flow region at the nozzle base (i.e., at the interface between the coflow and the centerjet). Flames detached from the nozzle exit if the centerjet enthalpy was reduced below a certain threshold. Weak detached flames or no flames were the result in cases with vitiated air center jet and C_2H_4 coflow. Several of these flames will be discussed in section Flame Visualizations below.

2.3 Large Scale Facility Tests

2.3.1 Nozzle and Facility Descriptions and Instrumentation

The nozzle for the large scale tests, which is axisymmetric except for bolts, instrumentation, etc., is illustrated in Figure 2. It consists of a water-cooled nickel mating flange, a water-cooled copper nozzle block, and a stainless steel cone. The heated center flow nozzle is formed within the copper block, and its contour was designed by the method of characteristics to provide a uniform Mach 1.6 flow at the exit, at the nominal test point. A coflow nozzle is formed by the space between the copper block and the steel cone. A sintered mesh porous plate is trapped between the cone and the block, forming the coflow plenum. The coflow gas (typically H_2 and/or C_2H_4) is supplied, unheated, to the coflow plenum; the gas passes through the porous plate, which distributes the flow uniformly around the circumference, and is accelerated in the nozzle. Mach number at the coflow nozzle exit is low, approximately 0.07, and the pressure in the coflow plenum (upstream of the porous plate) is approximately 650 kPa for the nominal test case studied with the CARS-IRS system (B.b in Table 2). The nozzle is instrumented with three spring-loaded thermocouples at the bottom of 6.35 mm diameter blind holes (from the outside) in the copper block. The bottom of these holes is located such that the thermocouple approximately measures the unperturbed nozzle surface temperature [3]. A fourth thermocouple is attached with ceramic glue to the base of the nozzle the base is defined as the forward facing exterior surface between the center jet and coflow nozzle exits. A pressure tap is located in the nozzle ahead of the contraction.

The nozzle is attached to the vitiated air heater of the Direct Connect Supersonic Combustion Test Facility. The heater provides the products of combustion of H_2, O_2 and air to the nozzle. The combustion chamber of the heater is 229 mm internal diameter and approximately 1.32 m long. At the upstream end, 12 injectors are distributed on a 127 mm diameter. Air and O_2 are premixed upstream and are made to enter the combustion chamber around the outside of each injector, while H_2 is made to enter through the center of each injector. The minimum flow area at each injector is 101 mm^2 for the air-O_2 mixture and is 1.37 mm^2 for the H_2.

Mass flow rates are measured with an uncertainty of $\pm 3\%$ using standard ASME, sharp-edged orifice plates, pressures are measured with an uncertainty of $\pm 1\%$ using strain gauge type pressure transducers, and temperatures are measured with an uncertainty of ± 2 K or $\pm 0.75\%$ (whichever is greater) using type K thermocouples.

In addition to facility instrumentation, the free jet flow near the nozzle exit is monitored with an infrared light (IR) digital video camera, FLIR Model SC4000-MWIR, with sensitivity in the 3-5 μm range and electronic shutter exposure time set nominally to 12 μs. Video is also acquired in some runs with commercial grade visible light video cameras, which had a relatively long image integration time (1/30 s). Additionally, for certain cases the flow was extensively probed with the dual-pump CARS-interferometric Rayleigh scattering

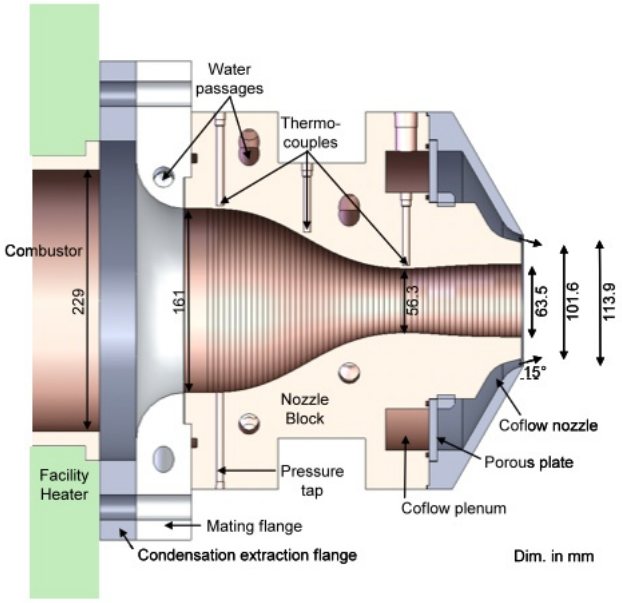

Figure 2. Horizontal section of large scale nozzle.

(CARS-IRS) optical system (these results have been reported separately) [20]. The nozzle installed in the facility is shown in Figure 3. Inset in this figure is an IR image of a case in which there is combustion of H_2 coflow. The flow is from left to right in this image as with all flame images, while the color is false (there is no spectral content in the image), and the brightness is in proportion to temperature. The brightness scale generally differs from one IR image to the next, so comparisons of brightness between images should not be made. Also, a few of the elements of the optical system may be seen in the picture.

2.3.2 Test Conditions and Nozzle Wall Temperatures

Test cases were for vitiated air in the center jet and either no coflow, or a coflow of a fuel. In principle, the facility could be operated to provide excess H_2 in the center jet, as in the laboratory. However, under normal operation the facility provides vitiated air: operation with excess H_2 would have been a new mode of operation requiring minor modifications to the combustor and testing to verify. Additionally, the rates of H_2 flow were high, raising safety concerns. Time constraints did not allow for these issues to be addressed, and this mode was not attempted.

Tests were conducted over a range of test gas temperatures, at enthalpy Mach numbers (M_h) from 5 to 7. (The enthalpy Mach number is the Mach number of flight for which the air in the reference frame of the vehicle has the same sensible total enthalpy as the test gas.) Facility flow rates were set to provide vitiated air with nominally the same mass fraction of unreacted O_2 in the products as is contained in air (23%). Facility flow rates for nominal conditions, as well as computations of the total pressure and temperature in the combustion chamber are provided in Table 1. Computations assume quasi-1D flow and that the heat loss from the combustion products to the facility (structure and cooling water) is 20% of the sensible enthalpy of the products, referenced to the reactant inflow temperature [3]. Flow rates of coflow are expressed in terms of an overall equivalence ratio between the coflow and the center jet ϕ; an equivalence ratio of one implies that the unreacted fuel in one flow and

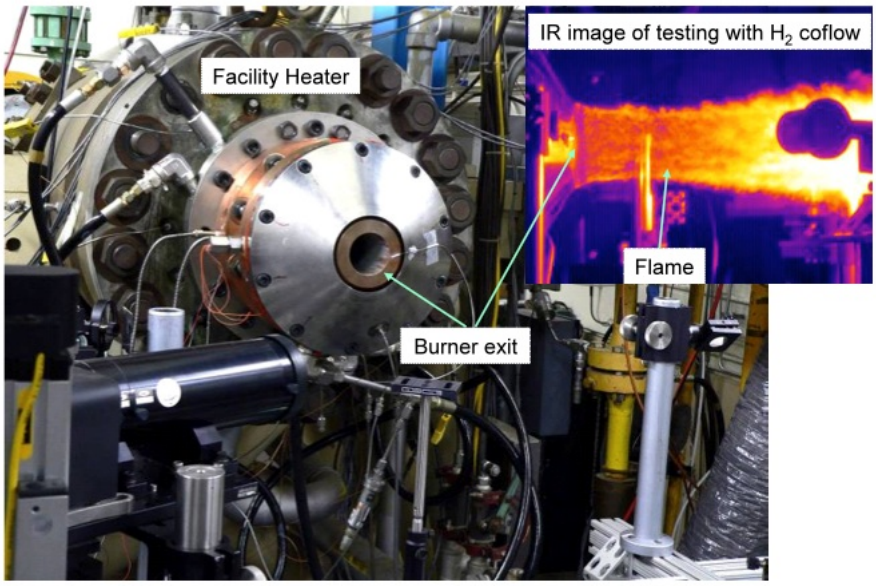

Figure 3. Image of nozzle installed in LaRCs Direct Connect Supersonic Combustion Test Facility; inset is IR image of flame.

Nominal condition			Flow rate (kg/s)		
M_h	p_t (kPa)	T_t (K)	*air*	H_2	O_2
5	424	1163	1.038	0.0128	0.1358
5.5	419	1327	0.920	0.0144	0.1535
6	414	1504	0.816	0.0161	0.1712
7	405	1842	0.644	0.0195	0.2070

Table 1. DCSCTF flow rates at nominal operating conditions.

the unreacted O_2 in the other could react completely to form H_2O (and CO_2) products.

Nozzle wall temperatures at enthalpy Mach numbers from 5 to 7, both with and without coflow, are shown in Figure 4. Data for three thermocouples are shown: the first and second, from left to right in the nozzle (see Figure 2), and at the base. The third thermocouple in the nozzle (near the throat) failed early on in the testing but, where data was obtained, indicated temperatures similar to the second thermocouple. Wall temperatures are between 300 K and 435 K for the first and base thermocouples, and between 300 K and 350 K for the second. Temperature generally tends to increase at a decreasing rate with time, but steady state is not nearly reached by 60 s of run time. The rate of temperature rise for all thermocouples tends to be greater at greater enthalpy. For the $M_h = 7$ data, the first thermocouple indicates a temperature drop 5 s - 15 s into the run that is attributed to the arrival of small amounts of liquid water, flowing on the surface of the nozzle from the heater (see section below Water Condensation in the Heater). After two runs at $M_h = 7$, some oxidation was noticed near the nozzle throat and no additional runs were performed at this condition. For cases with coflow, the coflow is switched on 5 s - 10 s into the run and ends shortly before the end of the run. Coflow does not significantly affect the first and

second thermocouple temperatures. The thermocouple at the base indicates a temperature drop immediately after the coflow is switched on, and thereafter it rises more slowly; coflow reduces the base temperature by 25 K 50 K.

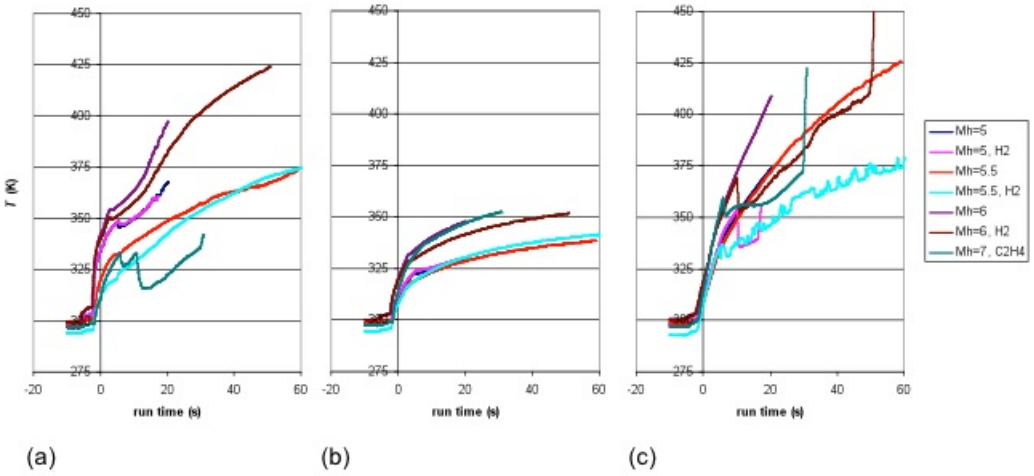

Figure 4. Nozzle wall temperatures: (a) first, (b) second, (c) base thermocouple.

2.3.3 Water Condensation in the Heater

During early phases of the testing, liquid water was observed in video images, such as Figure 5, discharging from the nozzle exit during facility operation. Water was observed for all test points (M_h=5, 6, and 7) with an M=2 nozzle installed, being greater at the higher enthalpy. This water discharge was unacceptable from the standpoint of the experiment as it interferes with the CARS-IRS optical system, and it would enter into the flow at the mixing layer between the vitiated air center jet and the fuel coflow, altering this most important region of the flow. Two hypotheses were advanced for the source of this water: leakage from the heater cooling circuits and condensation from the combustion products on the relatively cool heater inner liner. No water was discharged when the facility was operated with cooling flow and with flow of gases (air), but with no combustion. Nor was water leakage observed when the nozzle was removed and the heater inspected, with cooling flow on. For normal rates of cooling flow at the M_h=6 test point, thermocouples installed in the heater liner indicated temperatures at the end of a 30 s facility run of 364 K at 0.94 m from the end of the heater and 315 K at 0.23 m from the end. These temperatures increased to 440 K and 349 K, respectively, when the cooling water was reduced to approximately 1/5th of the normal rate: however, the temperature was rising steadily during the run and was not near the steady state by the end. At this test point the temperature at which the water vapor in the combustion products becomes saturated is approximately 375 K, above the temperature of the liner, at least at the downstream end. Thus, it was tentatively concluded that the source of the water is condensation, and further, that the problem could not be eliminated by reducing the cooling flow to the heater. A water extraction flange was installed between the nozzle and the heater, which contains two 6 mm drain holes at the bottom to collect and drain condensate from the heater during a facility test, before it enters the nozzle region. Tubes ran from these holes to a bucket where liquid is collected: typical rate of collection is 115 ml 150 ml per 30 second test. In addition to the liquid water, some gas is discharged from the drain holes, but the amount is considered small in comparison to the total rate of

Figure 5. Condensation water discharge from facility prior to installation of extraction flange.

flow in the heater. After installation of these drain holes, video images similar to Figure 5 showed only a small amount of liquid water flow, occurring during the early part of the test on the nozzle surface upstream of the throat. No liquid water flow could be seen on the surface downstream of the throat, nor could any discharge into the jet flow be seen. This configuration was used for all subsequent tests. A chemical analysis of the discharge lent further weight to the hypothesis that the discharge was water that had condensed on the relatively cool inner liner of the heater, not cooling water, since certain dissolved chemical constituents expected in the cooling tower water were not present in the discharge.

2.4 Flame Visualizations

2.4.1 Laboratory Flames

Flame imaging results for the laboratory flames have been presented previously for a wide range of flames. More recent images are presented in Figure 6 and Figure 7, to provide a direct comparison between the flames in the laboratory and at the large scale.

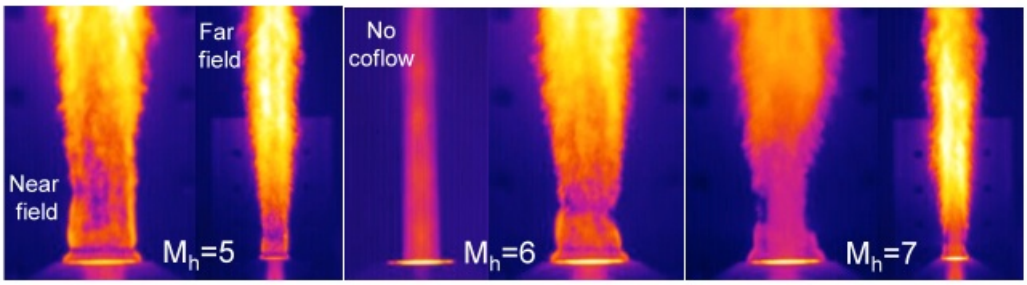

Figure 6. Laboratory flames imaged in the IR with coflow of H_2 at ϕ =1: near field and far field views at M_h=5, 7; near field closeup with and without coflow at M_h=6.

Figure 6 shows IR images with H_2 coflow and M_h equal to 5, 6, and 7 (from left to right). At M_h equal to 5 and 7, close up images near the nozzle exit and images of the complete flame are shown. At M_h equal to 6, an image without coflow combustion and a close up image near the nozzle exit are shown. Flow is from bottom to top. There is a very pronounced difference between the images with coflow combustion and without. With H_2 coflow, an edge attached flame is formed, attached to the nozzle exit and following the interface between the coflow and the surrounding ambient air. There is no visual evidence in the IR or visible light images with H_2 coflow (e.g., Figure 7a) of combustion within the region of flow recirculation at the base. Turbulent flow structures appear to be sharply resolved at

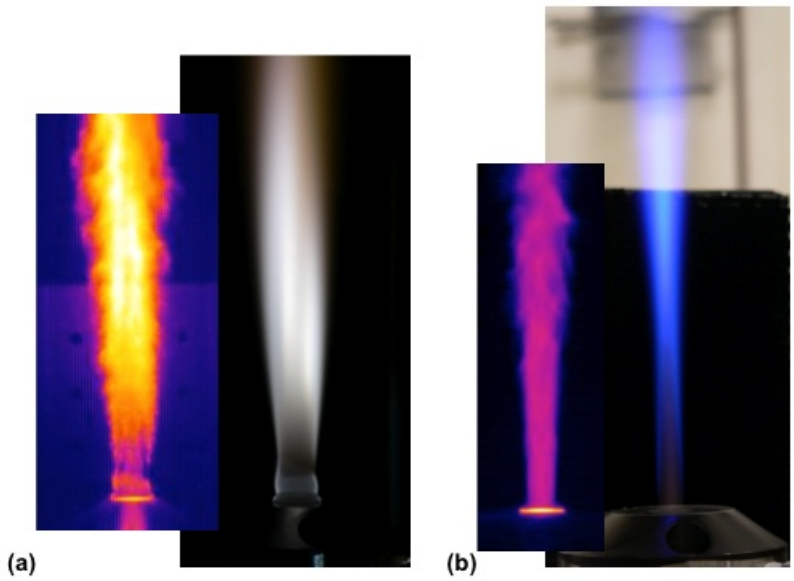

Figure 7. Laboratory flames imaged in the visible and IR: (a) coflow of H_2 at ϕ =1, M$_h$=6; (b) coflow of C_2H_4 at ϕ=1, M$_h$=7.

the outer boundary of the flame. The flow velocity of the center jet is approximately 1000 m/s (at $M_h = 5.5$). So, in the exposure time of the camera, structures moving at this speed would be expected to move approximately 12 mm and would therefore result in a blurred image. These edge structures must therefore move at much lower speed than the center jet. As the enthalpy Mach number is increased, the flame appears to weaken near the nozzle exit and begin to detach from the nozzle. This trend must be due to the increase in velocity of the centerjet which increases the strain rate at the coflow- ambient air interface, tending to extinguish the flame there. Without coflow, the centerjet is clearly visible, although structures at its edge are blurred due to the speed of the jet and the exposure time of the camera.

Figure 7 shows IR and visible light images with (a) coflow of H_2 at ϕ =1, M_h=6, and (b) coflow of C_2H_4 at ϕ =1, M_h=7. With H_2 coflow, the visible light image shows the flame to be pale bluish-white color due to emission from the OH radical; the long exposure time of the camera results in a smooth appearance of the flame. With C_2H_4 coflow there is very distinctive blue flame due to emission from CH radicals, indicating some chemical reaction does take place; however, the IR emission as compared to the jet with no coflow shows very little additional IR emission, indicating little heat release and therefore incomplete reaction. In comparison with the H_2 flame, the C_2H_4 is narrower, except near the downstream end.

Case	M_h	ϕ_{H2}	ϕ_{C2H4}	flame state
A	5	1.1	0	none
B.a	5.5	0	0	none
B.b	5.5	1	0	attached
C.a	5.5	0.55	0	detached
C.b		0.55	0.43	further detach
D	6	1.31	0	attached
E.a	6	0.7	0	attached
E.b		0.7	0.53	attached
F.a	6	0.49	0	detached
F.b		0.49	0.47	further detach
G.a	6	0.64	0	attached
G.b		0.64	0.49	attached
G.c		<0.4	0.49	detached
H	6	0	0.9	none
I	7	0	1	detached

Table 2. Large scale facility test cases, nominal operating conditions, and corresponding flame states.

2.4.2 Large Scale Flames

Flame imaging results for the large scale flows are shown in Figure 8 - Figure 13: the centerjet enthalpy, coflow fuel type, coflow equivalence ratio, and flame state for these cases are summarized in Table 2. A more detailed discussion of these figures follows.

Figure 8 shows a sequence of images from a single run with M_h=5.5 and a stoichiometric H_2 coflow ($\phi_{H_2} = 1$). The first image shows the center jet during facility startup, just before the facility heater has achieved final flow rates, and before the coflow is started: a diamond shock pattern, typical of a supersonic jet with exit pressure below atmospheric, may be observed. The main purpose of this image is to show that the IR technique shows clearly the presence of the diamond shock pattern, if such a pattern exists. The second image

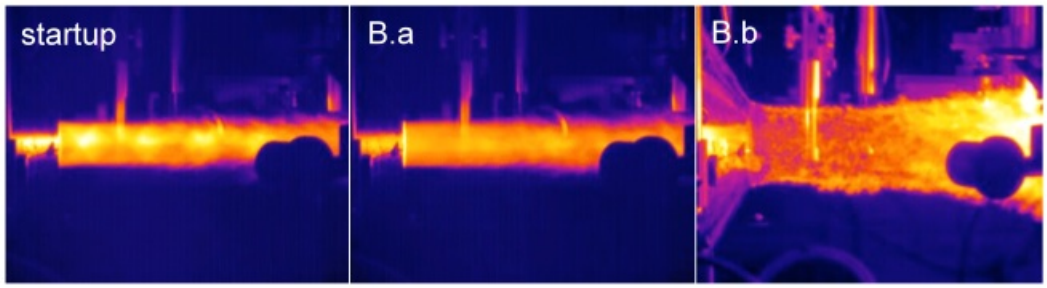

Figure 8. IR images of large scale flame during facility startup, Cases B.a (M_h=5.5), and B.b (M_h=5.5, H_2 coflow at ϕ =1)

(B.a) was taken shortly after final flow rates have been established, but before the coflow. A smooth shock-free jet flow is visible, with some larger turbulent flow structures towards the downstream end of the field of view. The third image (B.b) is after the coflow has been established and shows an attached flame at the coflow-atmospheric air interface, very similar

to the flames observed for the laboratory burner in Figure 6. As with the laboratory burner, turbulent flow structures are clearly visible at the outer boundary of the flame, although many of these are smaller relative to the nozzle diameter than in the laboratory. This may be because either the smallest scales of turbulence are relatively smaller at higher Reynolds number or the smallest structures in the smaller flow are more blurred by the effects of motion and the finite exposure time of the camera.

Figure 9 shows visible and IR light images for two cases with M_h=6: the left-hand images (E.a) have H_2 coflow and the right (E.b) have a mixture of H_2 (at the same flow rate) and C_2H_4. In both cases, attached flames are observed. The second case is blue in color due to emission from CH radicals and, although not evident in the images, is much brighter in the visible light (the camera exposure adjusted automatically). Turbulent structures at the edge of the flame are smoothed out in these images due to the long integration time of this camera. The corresponding IR light images are shown directly above the visible at approximately the same scale. The images show essentially the same features except that turbulent structures are resolved. Note that differences in the appearance of beams and optical components between the visible and IR images are due to differences in the viewing angle (visible views vertically down and IR views horizontally).

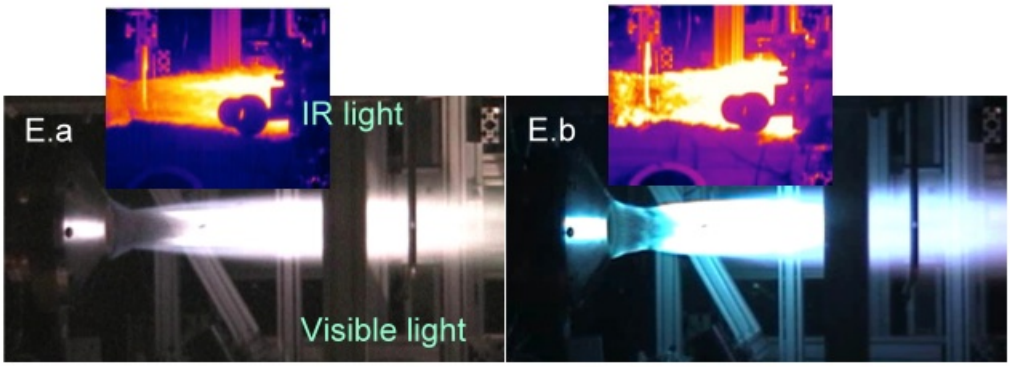

Figure 9. IR images of large scale flame during facility startup, Cases B.a (M_h=5.5), and B.b (M_h=5.5, H_2 coflow at ϕ=1)

Figure 10 shows several visible and IR images for two cases with M_h=5.5: the left-hand images (C.a) have H_2 coflow and the right (C.b) have a mixture of H_2 (at the same rate) and C_2H_4. In both cases the flames are detached from the nozzle exit, being detached further downstream in the second case. Sequences of images in the IR (C.a) and in the visible (C.b) show that in both cases the flame is unsteady at large scale, moving up and downstream over a significant distance at relatively low frequency (approximately 10 Hz 100 Hz). (The frequency is known to be this low since some of this motion is resolved by the visible camera.) Figure 11 shows IR images for two cases with M_h=6.0: the left-hand image (F.a) has H_2 coflow and the right (F.b) has a mixture of H_2 (at the same rate) and C_2H_4. Figure 12 shows IR images for three cases with M_h=6.0: the first image (G.a) has H_2 coflow, the second (G.b) has a mixture of H_2 (at the same rate) and C_2H_4, and the third (G.c) is in the process of reducing H_2. The first two cases are similar to the cases in Figure 9, and show attached flames; the third image shows the flame in the process of detachment from the nozzle, and may be compared to the right hand images in Figure 6 which show a similar process in the laboratory burner. In summary, inspection of the image sequences, typified by the images shown, indicate a trend toward detachment and downstream movement of the flame as the flow of H_2 is reduced, and as C_2H_4 is added to the H_2.

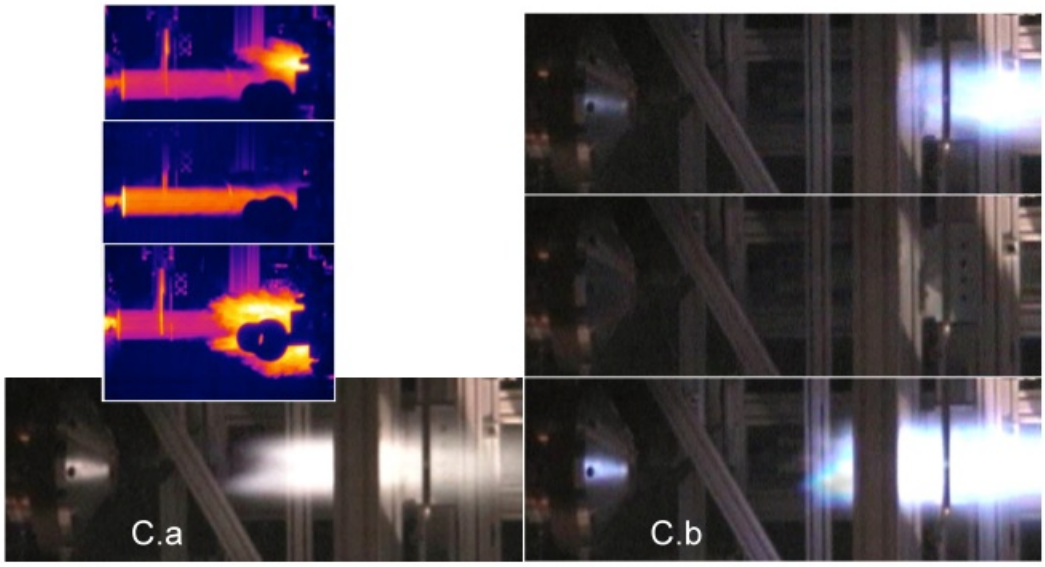

Figure 10. Visible and IR light images of Cases C.a and C.b, M_h=5.5 and H_2 or mixed H_2 - C_2H_4 coflow, showing detached, unsteady flames.

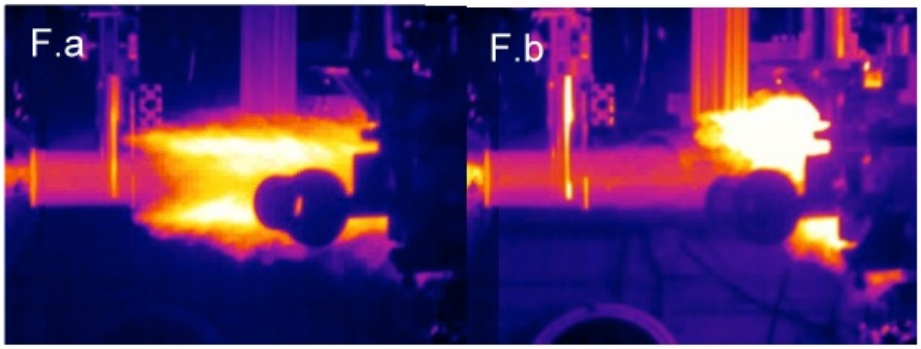

Figure 11. Cases F.a and F.b, M_h=6 and H_2 or mixed H_2-C_2H_4 coflow, showing detached, unsteady flames.

No flame was observed at all with M_h=6 and pure C_2H_4 coflow (H — see Table 2). Figure 13 shows a single visible image for M_h=7 and C_2H_4 coflow (I): a very intense detached flame is observed in this case. This image may be contrasted with Figure 7b, which shows relatively little combustion in the laboratory flame for the same nominal condition.

2.5 Test Cases for CARS-IRS Studies

Three test cases are identified for study with the CARS-IRS optical system to provide detailed data for CFD model development. These cases represent a sequence of increasing complexity which together allow several models to be calibrated.

The first case is an $M = 1.6$ $M_h = 5.5$ center jet of vitiated air with no coflow and no jet combustion (Figure 8 B.a). Temperature gradients in the mixing layer with the surrounding

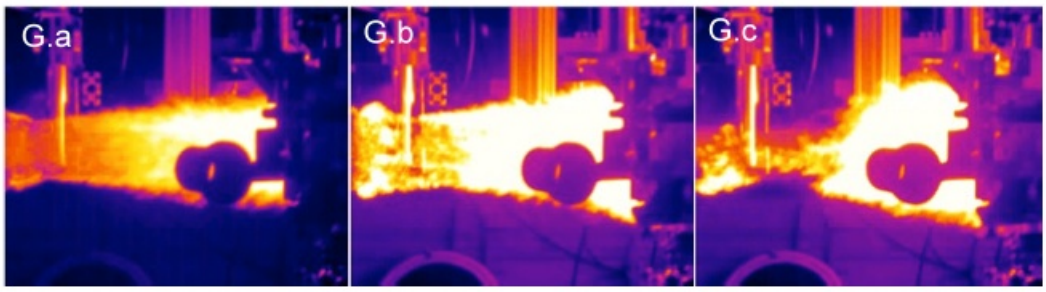

Figure 12. Cases G.a, G.b, G.c, M_h=6 and H_2 or mixed H_2-C_2H_4 coflow, showing detachment as H rate is decreased.

Figure 13. Visible light image for Case I, M_h=7 and H_2-C_2H_4 coflow, showing intense detached flame.

air are large but composition gradients are not very large. Important turbulence models in this flow are the models for Reynolds shear stress and Reynolds heat flux. The CARS-IRS data set has been acquired and results are presented in section 4 of this report.

The second case is a $M_h = 5.5$ center jet of vitiated air with H_2 coflow and $\phi_{H_2} = 1$ (Figure 8 B.b). This case has an attached flame. In addition to the turbulence models above, the model for Reynolds mass flux is important. Also, the flow is complicated by heat release in the shear layer that should provide a more rigorous test of the heat flux model. CARS-IRS data has been acquired for this case, but the data set is not complete.

The third case is a $M_h = 5.5$ center jet of vitiated air with a coflow mixture of H_2 and C_2H_4 (Figure 9 E.b). This case also has an attached flame. It is similar to the previous case but has a more complicated chemistry. This case is of interest because of the importance of hydrocarbon fuels in scramjets.

Prior to the flame visualization studies, it was believed that a detached flame would be a suitable test case for detailed study with CARS-IRS since it would be sensitive to chemistry and turbulence chemistry interaction models. Thus, it would fit into the logical progression of increasing complexity. However, the detached flames are unsteady with time scales much longer than the characteristic turbulence fluctuation time scale of the mixing layer. It is not possible to separate the fluctuations in measured flow properties due to this unsteadiness from fluctuations due to turbulence with available techniques, so it is not possible to measure the statistical properties of the turbulence fluctuations in this flow. Also, this flow would have to be computed with a time-accurate method, so would be more computationally intensive. Finally, these unsteady flames are accompanied by significant (acoustic) noise which poses a structural-vibration problem for the optical systems.

The measured conditions for the CARS-IRS tests accomplished in the DCSCTF at this time follows. The average and the standard deviation of facility flow rates (statistics formed including variation within runs and from run to run) are for air flow, O_2 flow, and H_2 flow respectively: 0.920±0.012 kg/s, 0.155±0.005 kg/s, and 0.0147±0.0004 kg/s. The total pressure measured in the facility combustion chamber is p_t = 414±27 kPa. For the second case the H_2 coflow is 0.032±0.004 kg/s. (Uncertainties are given for the 95% probability limits.)

2.6 Summary and Conclusions

Experiments are described to provide data for development and validation of computational models of turbulent mixing and combustion in scramjet engines. A laboratory scale burner was developed which provides a 10 mm diameter supersonic center jet of combustion products, containing either excess H_2 or excess O_2; and, an unheated coflow of air or fuel (H_2 or C_2H_4), respectively. Both cases result in a supersonic flame. This burner was used to test newly developed CARS-IRS optical techniques for flow measurement, and to evaluate flames for more detailed study. A nozzle was developed and integrated with NASA Langleys Direct Connect Supersonic Combustion Test Facility to create a large scale flow similar to the laboratory flow, but scaled by × 6.35. The turbulent flow structures of this larger flow could be better resolved by the optical instrumentation. The center jet in these experiments consisted of combustion products of H_2 in air and O_2, with O_2 content the same as standard air, and the coflow was of H_2, or C_2H_4, or a mixture of both. Facility data and visualization of various flames in this facility, using infrared and visible light cameras, are presented. Test cases for more detailed examination using CARS-IRS were selected based on this visualization. These cases, in order of increasing complexity, are: a case with no coflow and no jet combustion; a case with H_2 coflow and flame attached to the nozzle exit; and a case with an H_2 and C_2H_4 mixture and attached flame. In certain cases, detached flames were observed, but these were unsteady and probably too complex to be useful for the current computational model developments.

3 Numerical Simulations for Design of the Full-Scale Supersonic Combusting Jet Experiment

CFD calculations using the Reynolds-averaged Navier-Stokes equations coupled with species continuity equations have been made for the supersonic combusting jet experiment to determine the sensitivity of the external flowfield to the main-nozzle exit profile [22]. Four different nozzle exit profiles were used in the study: a uniform profile, one computed using only the nozzle geometry, one computed using the nozzle geometry and part of the upstream facility combustor, and one using the nozzle and the full facility combustor. Two cases were examined using the four profiles: a non-reacting case without coflow and a reacting case with hydrogen coflow. Results show that the nozzle exit profile has a significant effect on the external flowfield. The uniform profile produced the longest jet while the profile created with the full combustor produced the shortest jet. The nozzle-only and part-combustor profiles fell between the other two profiles. The reacting flow was found to be more sensitive to the nozzle exit profile since it affects the downstream mixing and combustion. These calculations indicate the importance of properly setting the nozzle-exit profile for this type of calculation.

3.1 Introduction

The numerical simulation of high-speed, chemically-reacting flow fields is very challenging due to the large number of physical phenomena involved in these types of flows. The development and validation of the physical models in the CFD codes used for these simulations is also challenging due, in part, to the lack of detailed and complete experimental data sets in supersonic combusting flows. To address this second challenge, a co-axial supersonic-combusting free-jet experiment in which simultaneous, instantaneous, co-located measurements of a number of flow properties have been taken [23–30]. CFD using the Reynolds-averaged Navier-Stokes equations coupled with species continuity equations was used to help design the experiment and identify CFD validation needs [31].

During the design phase of the experiment, the importance of properly specifying the CFD boundary conditions was recognized. However, it was also recognized that not every property could be measured to the degree needed to accurately set boundary conditions. To be a proper validation experiment, the flowfield parameters of interest should not be sensitive to assumptions made to set the boundary conditions, otherwise the comparison between CFD and data depends too much on the cleverness of the person setting the boundary conditions. This may require the boundary conditions to be moved to a location where assumptions have a minimum effect on the solution. This, in turn, may increase the size of the computational domain, increase geometric complexity and/or add additional physical processes. In spite of this, if the required experimental data is lacking, then a numerical study must be undertaken to determine the sensitivity of the CFD solution to assumptions made in setting boundary conditions. Towards that end, this section presents CFD results of both a non-reacting, mixing-only case and a chemically-reacting case, and includes an investigation of the importance of including the facility combustor and the internal nozzle flows in the calculations.

3.2 Geometry and Grids

The experiment was conducted in the Direct-Connect Supersonic-Combustion Test Facility (DCSCTF) [32] at NASA Langley Research Center. The co-axial jet hardware, shown installed in the DCSCTF in Figure 14, is mated to the facility combustor, which provides hot vitiated air for the main jet. The flow from the main and coflow nozzles exhaust directly into the ambient air of the test cell. At the downstream end of the test cell, an open pipe connected to a 70-foot diameter vacuum sphere, draws jet gases out of the room. To prevent the inadvertent buildup of combustible gases during operation, a large fan draws outside air into the room and vents it to the roof. Further details of the experiment are given in section 2.

To simplify the numerical simulations, the computational domain was divided into internal and external parts. The internal geometry consists of the facility combustor and the main-jet nozzle. In the facility combustion-heater, oxygen is mixed with air in a plenum upstream of the combustor. From this plenum it flows through 12 holes in a baffle plate into the combustor. Hydrogen is injected into the combustor through 12 injectors that are positioned with their tips in the center of the baffle-plate holes. The injectors are smaller than the holes so that the oxygen-rich air surrounds the injected hydrogen as they enter the combustor. The axisymmetric water-cooled combustor is 51.75 inches long and has an inner diameter of 9 inches. There is a 5.75 inch long, 6.875 inch inner-diameter burner-can positioned just inside of the combustor which creates a 1.0625 inch rearward facing step downstream of the baffle plate. At the target test point, some of the steam generated in the combustion process condensed on the water-cooled combustor surface. To prevent liquid water from spraying into the test flow, a condensate trap was created by adding a 1.25 inch wide spacer with an 11.5 inch inner diameter between the combustor and the nozzle. Several

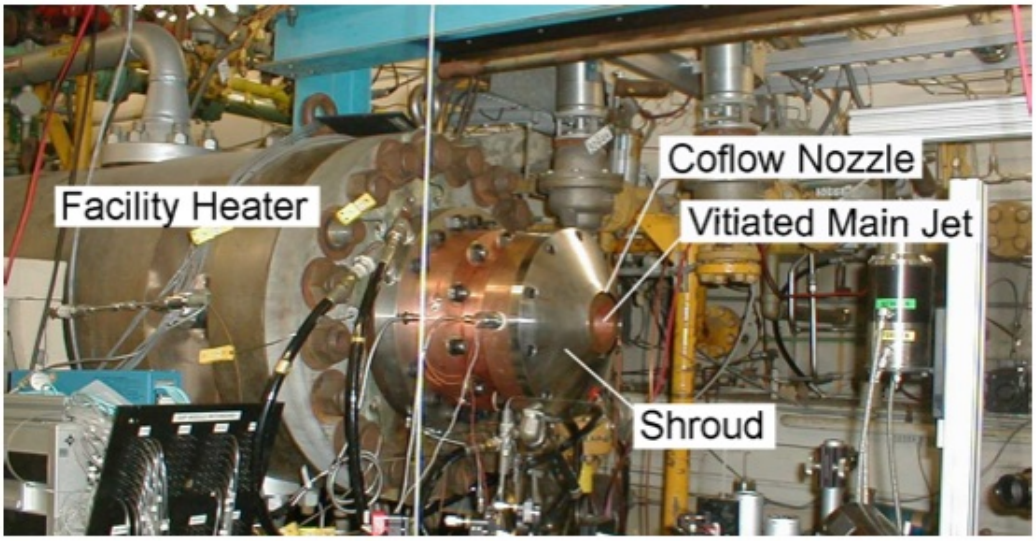

Figure 14. Experiment in the Langley Direct-Connect Supersonic-Combustion Test Facility

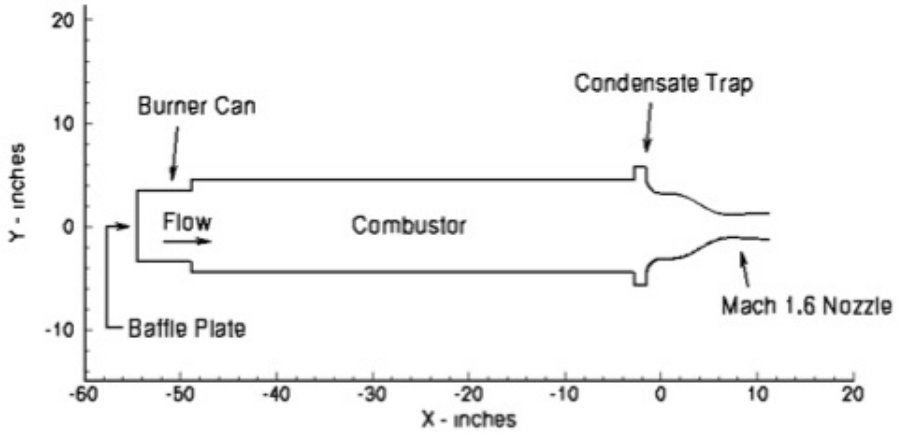

Figure 15. Internal Geometry

small holes at the bottom of the trap allowed water to be removed during operation. The internal geometry ends with the Mach 1.6 water-cooled nozzle. This nozzle has a relatively large exit diameter (2.5 inches) to provide a large enough scale for good spacial resolution with the measurement technique. A schematic of the internal geometry is provided in Figure 15.

Because the geometry is axisymmetric, the grid is limited to a planar region extending from the axis of symmetry to either the solid walls forming the internal surfaces or the outer boundary. (Note that some figures show the solution domain and its mirror image for clarity.) The grid for the internal geometry consisted of 5 blocks. The first block filled the volume of the burner can. The second filled the volume between the burner can and the condensate trap. The third and forth blocks filled the volume of the condensate trap,

while the fifth block filled the volume of the nozzle. The block boundaries were made so that the geometry could be easily subdivided, as will be discussed further in the section on internal flow calculations. Coarse, medium and fine grids were generated for the internal geometry.The medium grid was created from the fine grid by halving the number of points in each of the two computational directions (1/4 the total number of cells). The grid spacing was adjusted on each grid level to maintain a reasonable near wall spacing (y+ in the range of 25 to 40 with peaks no greater than 90). The coarse grid was created from the medium grid in a similar fashion, with the exception of block 4, which had 85 points instead of 77 points in one of the directions. This was done to prevent a portion of the grid from being overly coarse while maintaining the target near wall spacing. Grid sizes are provided in Table 3.

Block	Fine Grid	Medium Grid	Coarse Grid
1	129 x 209	65 x 105	33 x 53
2	257 x 273	129 x 137	65 x 69
3	97 x 129	49 x 65	25 x 33
4	305 x 65	153 x 33	85 x 17
5	193 x 193	97 x 97	49 x 49
Num Points	166,709	42,141	10,905

Table 3. Internal Geometry Grid Dimensions

The external solution domain starts at the exit of the main nozzle and extends 150 inches downstream (60 jet diameters). The outflow plane extends radially outward 100 inches (40 jet diameters). In the nozzle exit plane, there is a 0.75 inch rearward facing surface which separates the nozzle exit flow from the coflow. The exit of the coflow extends from a radius of 2.0 to 2.25 inches. A shroud covers the hardware and extends radially outward from the outer edge of the coflow to a point with a radius of 7.5 inches and 3 inches upstream of the nozzle exit plane. The ambient-air inflow plane is 6.28 inches upstream of this point. The inflow plane extends from a radius of 7.5 inches to 125 inches. The outer boundary is sloped and connects the inflow plane at a 125 inch radius to the 100 inch radius outflow plane. The internal flowpath of the coflow is included in the external solution domain due to the subsonic injection of the coflow. The exit of the coflow is angled 15 degrees downwards towards the nozzle exit. Figure 16 shows a close-up of the nozzle-exit near-field flowpath, while Figure 17 shows the full geometry (internal and external).

The external geometry is composed of 4 blocks. The first block is the coflow plenum, while the second block is the coflow nozzle. Block 3 is a rectangular region that extends from the ambient-air inflow boundary to the corner point of the shroud and extends radially outward from the outermost portion of the shroud to the outer boundary. Block 4 is the remainder of the external flow. As with the internal flow, coarse, medium and fine grids were created for the external geometry. Also, as with the internal grids, some of the medium and coarse grid dimensions were adjusted to prevent the near wall grid spacing from becoming too large. The external grid dimensions are given in Table 4.

Grid points are clustered near the jet exit to resolve near-field flow features. The fine grid has 926 evenly spaced points in the axial direction in the first 5 jet diameters downstream of the nozzle exit. In the next 5 jet diameters there are another 330 points with a small stretching factor. The remaining 629 points in the axial direction stretch from 10 jet diameters to the outflow boundary at 60 jet diameters.

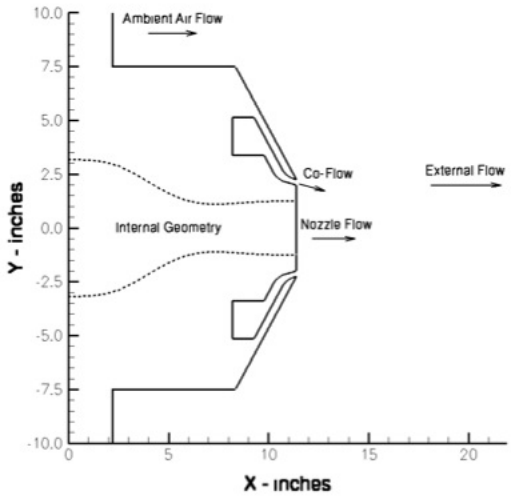

Figure 16. External Geometry Near Nozzle Exit (Dashed Internal Geometry Included For Clarity)

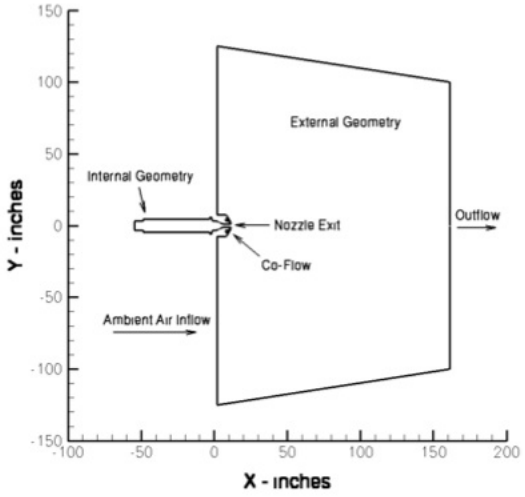

Figure 17. Full (Internal and External) Geometry

Block	Fine Grid	Medium Grid	Coarse Grid
1	49 x 129	25 x 81	25 x 41
2	65 x 65	65 x 33	33 x 17
3	65 x 385	65 x 193	33 x 97
4	1921 x 993	961 x 497	481 x 249
Num Points	1,943,124	494,332	124,556

Table 4. External Geometry Grid Dimensions

3.3 Non-Reacting Cases

The first case investigated was a single-jet-into-ambient-air mixing-only case with no coflow injection. The facility combustion-heater was operated to provide hot vitiated air with a nozzle exit pressure of one atmosphere. Post-combustion properties in the facility combustor were computed from the mass flow rates of gases (air, O_2, H_2) into the heater, assuming equilibrium chemical reaction. The gas properties and chemical composition from this calculation are given in Tables 5 and 6. To minimize computational time, minor species (NO, NO_2) were included in the equilibrium calculation for combustor properties but were neglected in the CFD calculations.

All the calculations presented in this section were made using the VULCAN CFD code [33]. This finite-volume structured-grid code is able to solve the Reynolds-averaged Navier-Stokes equations coupled with species continuity equations and finite-rate chemical reactions. Thermodynamic properties are computed using curve fits for thermally perfect gases [34]. For these calculations, the Reynolds stresses were modeled using the $k-\omega$ model of Wilcox [35] while gradient diffusion models with turbulent Prandtl and Schmidt numbers of 0.89 and 0.5 were used for the Reynolds heat and mass fluxes. Wall matching functions were used to reduce the near-wall grid resolutions requirements.

Property	Metric	English
Total Temperature	1,568.7 K	2,823.7 R
Total Pressure	427,473 Pa	62 psi

Table 5. Gas Properties

Species	Equil. Mass Fraction	CFD Mass Fraction
N_2	0.638610	0.638630
O_2	0.231439	0.231439
H_2O	0.118707	0.118707
Ar	0.011224	0.011224
NO	0.000018	-
NO_2	0.000002	-

Table 6. Gas Composition

3.3.1 Non-Reacting Internal Flow Calculations

To investigate the effects of upstream geometry on nozzle exit flow and the subsequent external flowfield, three sets of calculations were made using the coarse, medium and fine grids. The first set included the full geometry, the second included the full geometry less the burner can, and the third set included only the nozzle. These three geometries are referred to as the long-combustor, short-combustor and nozzle and are shown in Figure 18. In each case the entire left-most boundary was set to a uniform, post-combustion, subsonic, inflow boundary condition. This boundary condition held the composition and total conditions constant and allowed the inflow velocity to float. Solid walls were modeled as no-slip, isothermal surfaces with a temperature of 330 K. Convergence on each of the grids and for each geometry is given in Table 7.

The solutions for the long-combustor geometry proved to be unsteady for the medium and fine grids. The source of the unsteadiness is flow structures being shed from the rearward facing step of the burner can. These can be clearly seen in Figure 19 which shows contours of the ratio of turbulent viscosity to laminar viscosity. Although the unsteady flow from the combustor would certainly introduce some unsteadiness into the external flow, solving the internal and external flows together introduces a level of complexity beyond the scope desired for this report. Thus, for these two cases, the solution method was switched to an unsteady solution algorithm and the unsteady flow was allowed to establish over several flow-through times. The solution was then allowed to progress further in time (many more flow throughs) and the solution averaged in time. The mass flow error was monitored for the 9 cases and was less than 0.005 percent for the steady flow cases and less than 0.02 percent for the time-averaged unsteady cases.

Geometry	Coarse Grid	Medium Grid	Fine Grid
Nozzle	13.888	13.754	4.068
Short Combustor	6.079	13.339	5.107
Long Combustor	5.538	(unsteady)	(unsteady)

Table 7. Residual Drop in Orders of Magnitude - Internal Geometry, Non-Reacting Cases

Figure 20 shows the nozzle exit profiles of the Mach number, axial velocity, static temperature and the ratio of the turbulent viscosity to the laminar viscosity. In general, the

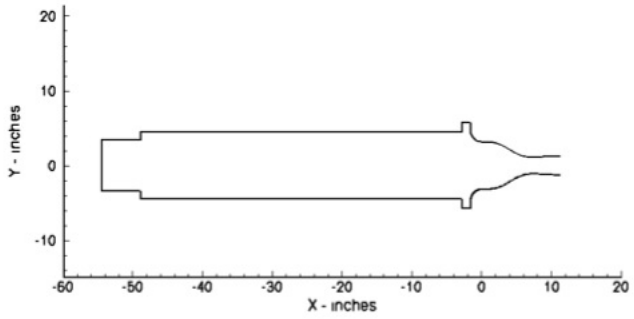

(a) Long Combustor

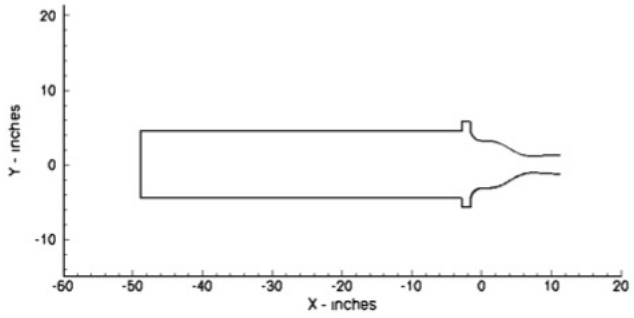

(b) Short Combustor

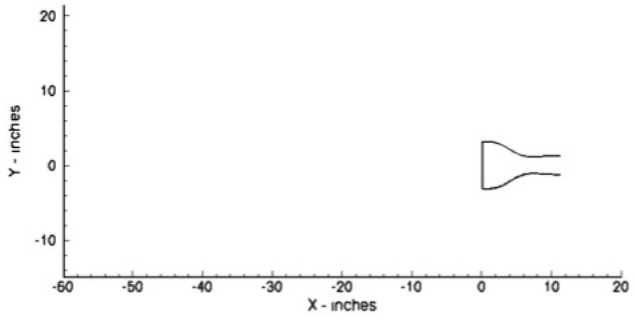

(c) Nozzle

Figure 18. Solution Domains of the Three Internal Geometries

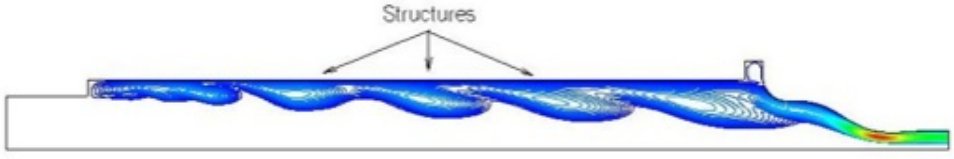

Figure 19. Snapshot of the Unsteady Flow in the Long-Combustor on the Fine Grid

Geometry	Coarse Grid	Medium Grid	Fine Grid
Top Hat	5.344	3.568	6.880
Nozzle	5.821	6.221	5.714
Short Combustor	5.869	6.234	2.761
Long Combustor	5.826	6.016	7.155

Table 8. Residual Drop in Orders of Magnitude - External Geometry, Non-Reacting Cases

difference between the coarse, medium and fine grids is smaller than the difference between the geometries. The velocity and temperature profiles show significant differences in the boundary layer thicknesses between geometries. The Mach number profile has the smallest difference between the geometries due to its functional relationship with velocity and temperature. There is also a significant difference in the levels of turbulent-to-laminar viscosity ratio at the nozzle exit. The nozzle-only geometry peaks at a ratio of about 90, the short-combustor geometry peaks at about 200, and the long-combustor geometry peaks at about 1130.

Figure 21 shows contours of turbulent-to-laminar viscosity ratio for all three geometries. In the nozzle case, the boundary layer begins to grow at the nozzle inflow and achieves a maximum level of viscosity ratio at the nozzle exit. For the short and long combustor geometries, the boundary layer also begins to grow at the inflow boundary but encounters downstream geometrical features (rearward facing step and condensation trap) which increase the turbulence levels. For both of these cases the viscosity ratio reaches its maximum value just upstream of the nozzle throat. The maximum levels are 324.4 and 2366.7 for the short and long combustors respectively. While the condensation trap increases the maximum viscosity ratio by a factor of about 3.6, it is the rearward facing step which has the greatest impact, increasing the viscosity ratio by a factor of 26.5 over the nozzle-only value.

3.3.2 Non-Reacting External Flow Calculations

The next step was to determine the effects of the nozzle exit profiles on the external flowfield solutions. The exit profiles from the internal flow calculations were used as a fixed inflow boundary condition for the nozzle portion of the external flow calculation. In addition to the exit properties computed from the three internal flow calculations, a top-hat (uniform) profile was added to the run matrix. The uniform properties were derived by isentropically expanding the total conditions of Table 5 to a Mach number of 1.5855, setting the turbulence intensity to 0.01 and the turbulent-to-laminar viscosity ratio to 0.01. The Mach number was selected to lie within the small range of centerline exit Mach numbers of the three internal flow calculations.

To improve the numerical convergence by convecting vorticies in the ambient air out of the solution domain, a small pressure gradient was applied across the domain by setting the ambient air inflow total pressure to 101,325 Pa and the outflow static pressure to 101,000 Pa. This resulted in a static pressure difference of 66 Pa (0.01 psi) across the domain and an ambient air flow of about 22 m/sec. Convergence on each of the grids (coarse, medium and fine) for each nozzle-exit flow profile is given in Table 8.

Figure 22 shows the flow structure of the non-reacting flow field. At these operating conditions, the nozzle is slightly underexpanded. This creates a series of expansion and compression waves which bounce back and forth between the centerline and the shear layer. These waves turn the flow alternately towards and away from the centerline as seen in the radial velocity contours in the lower half of the figure. There is an annular shear layer created between the jet and the surrounding ambient air which spreads and eventually merges at the

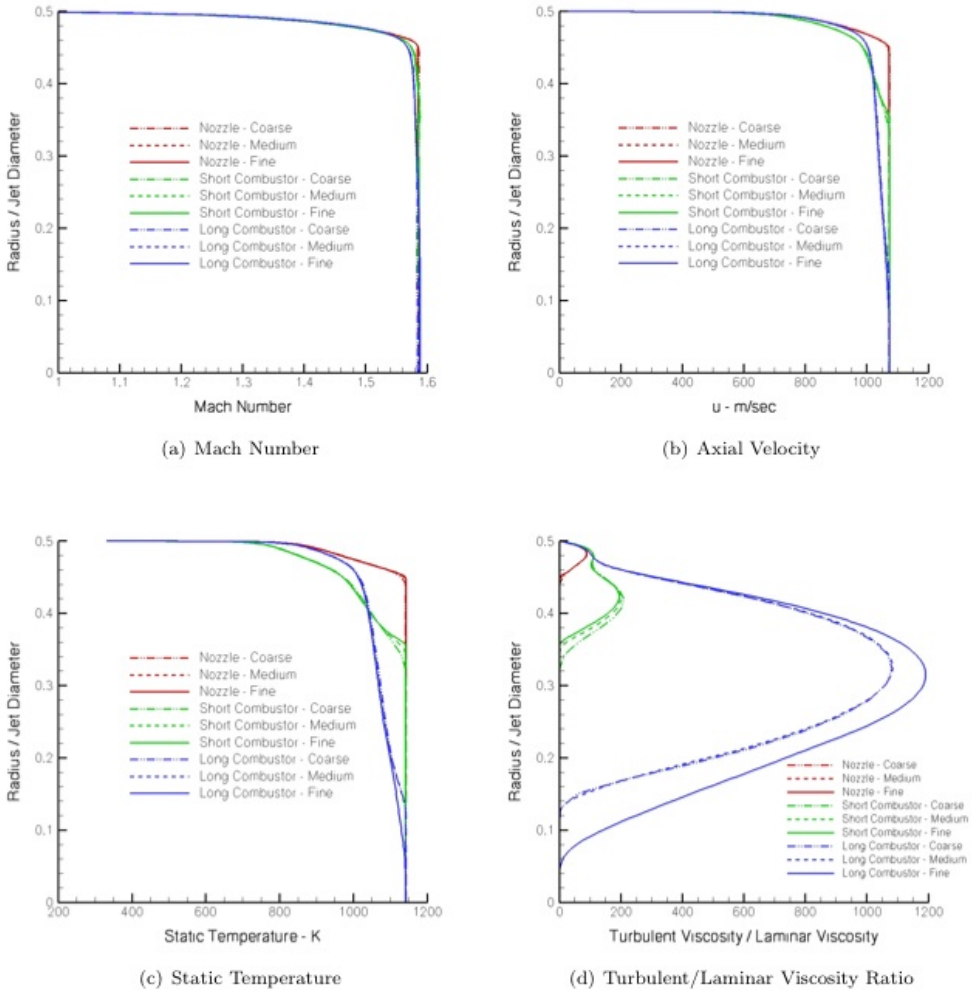

(a) Mach Number

(b) Axial Velocity

(c) Static Temperature

(d) Turbulent/Laminar Viscosity Ratio

Figure 20. Profiles at the Nozzle Exit

centerline. The jet entrains the surrounding ambient flow which separates from the surface of the shroud, creating a recirculating region on the face of the shroud. For this case there was no coflow and the air in the coflow-plenum and coflow-nozzle remained stagnant.

Figure 23 shows flow properties along the centerline. The variation of the properties in the near field are the result of the alternating expansion and compression waves previously described. In the near field, the various solutions are very similar, differing only a little in shape and amplitude. Larger differences begin to appear at axial locations greater than about 4 jet diameters. The top-hat profile shows the greatest difference from the other solutions in both wave amplitude and phase. The rapid decrease in properties between 6.7 and 11.4 jet diameters corresponds to the shear layer spreading and merging at the centerline. The axial location of the drop-off is about the same for the nozzle and short combustor geometries, is a little sooner for the long combustor and is quite a bit longer for the top-hat profile.

Figures 24-26 show radial profiles of axial velocity, static temperature and H_2O mass fraction at axial locations 1, 2, 5 and 10 jet diameters downstream of the nozzle exit. As

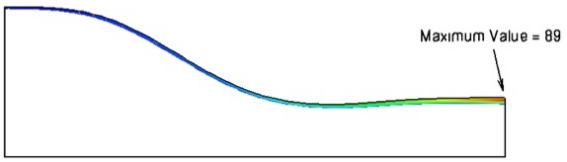

(a) Nozzle-only

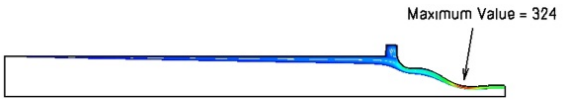

(b) Short Combustor

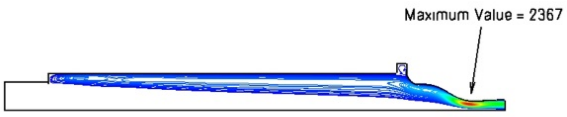

(c) Long Combustor (Time Averaged)

Figure 21. Fine Grid Contours of Turbulent/Laminar Viscosity Ratio

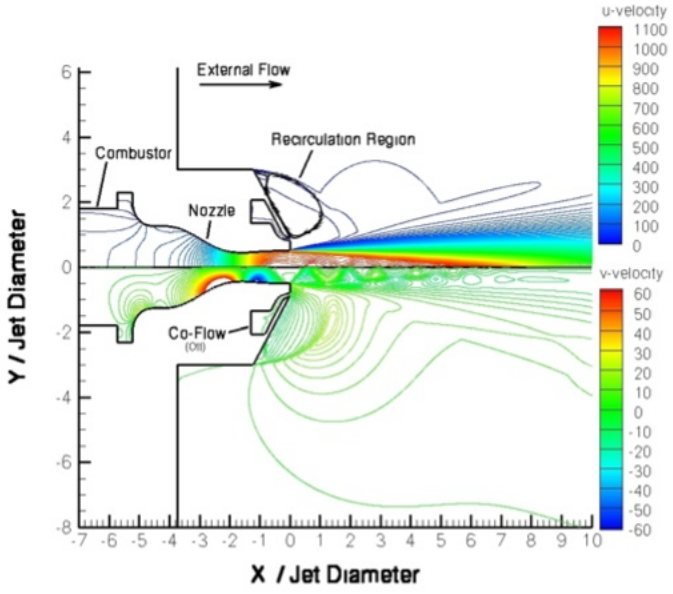

Figure 22. Non-Reacting Velocity Flow Field: Axial (u) and Radial (v) in meters/second

with the centerline properties, the top-hat profile results in the least diffusive external flow while the long-combustor produces the greatest.

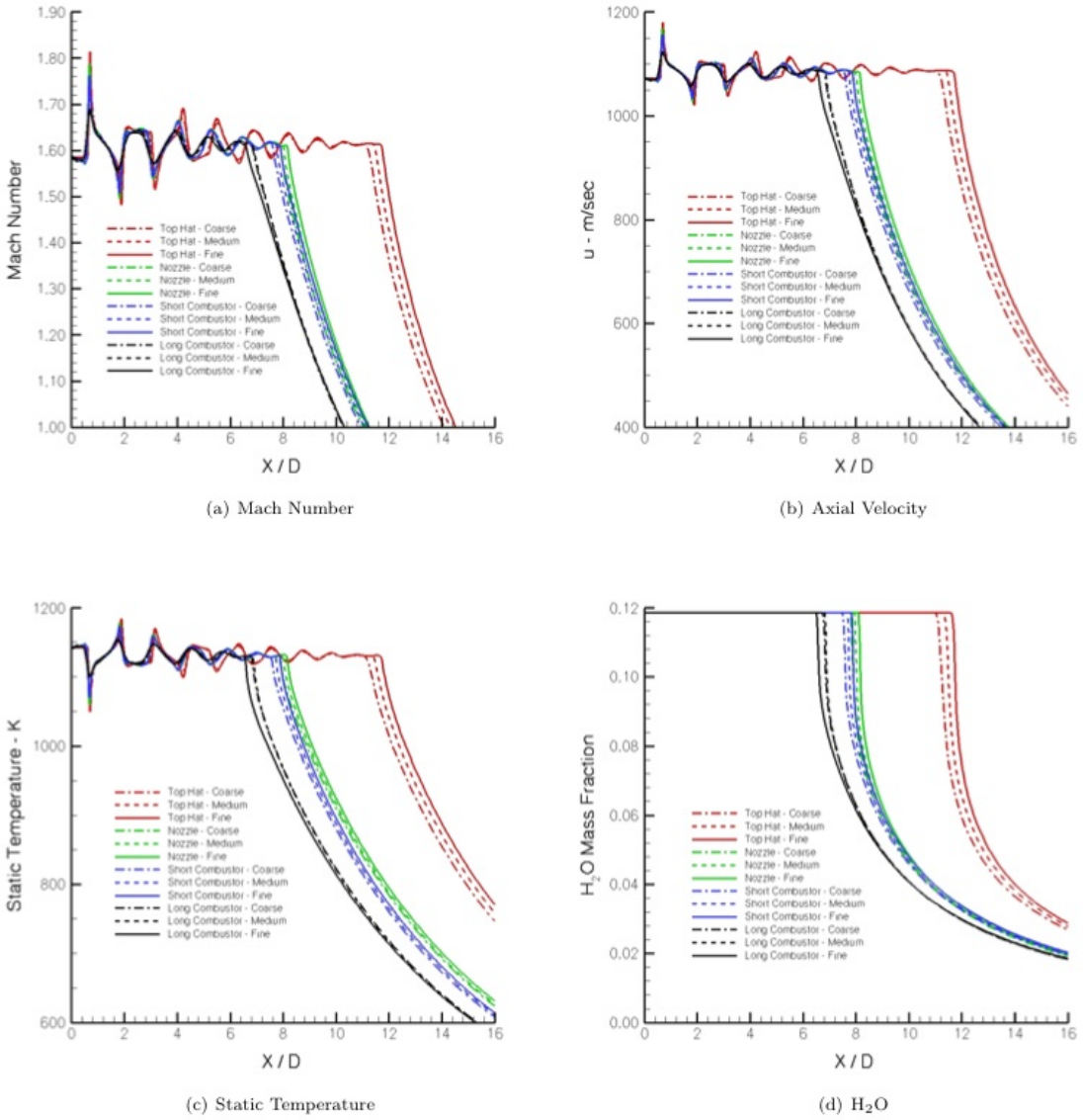

(a) Mach Number

(b) Axial Velocity

(c) Static Temperature

(d) H_2O

Figure 23. Non-Reacting, External-Flow Centerline Distributions

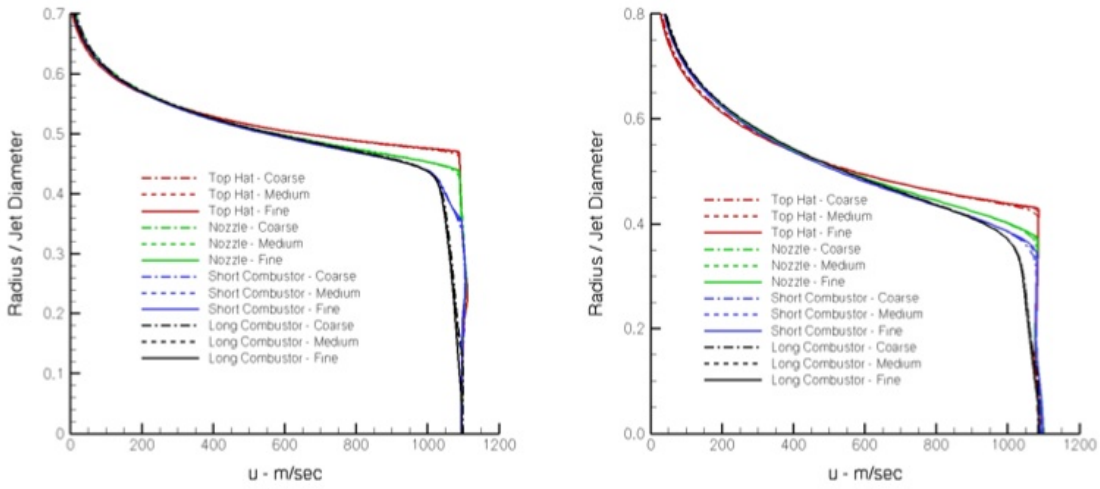

(a) X/D = 1

(b) X/D = 2

(c) X/D = 5

(d) X/D = 10

Figure 24. Non-Reacting, External-Flow Axial Velocity Profiles at Several Axial Locations

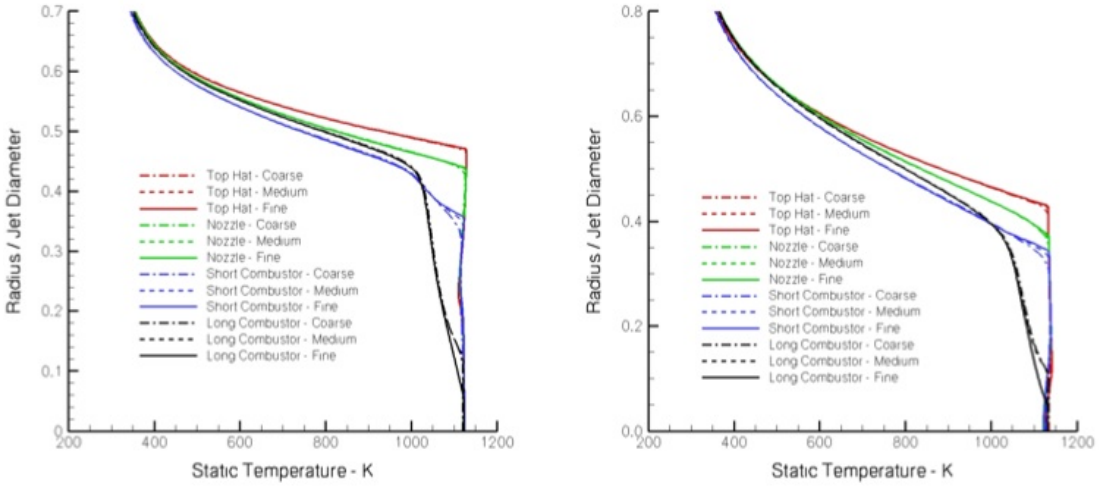

(a) X/D = 1

(b) X/D = 2

(c) X/D = 5

(d) X/D = 10

Figure 25. Non-Reacting, External-Flow Static Temperature Profiles at Several Axial Locations

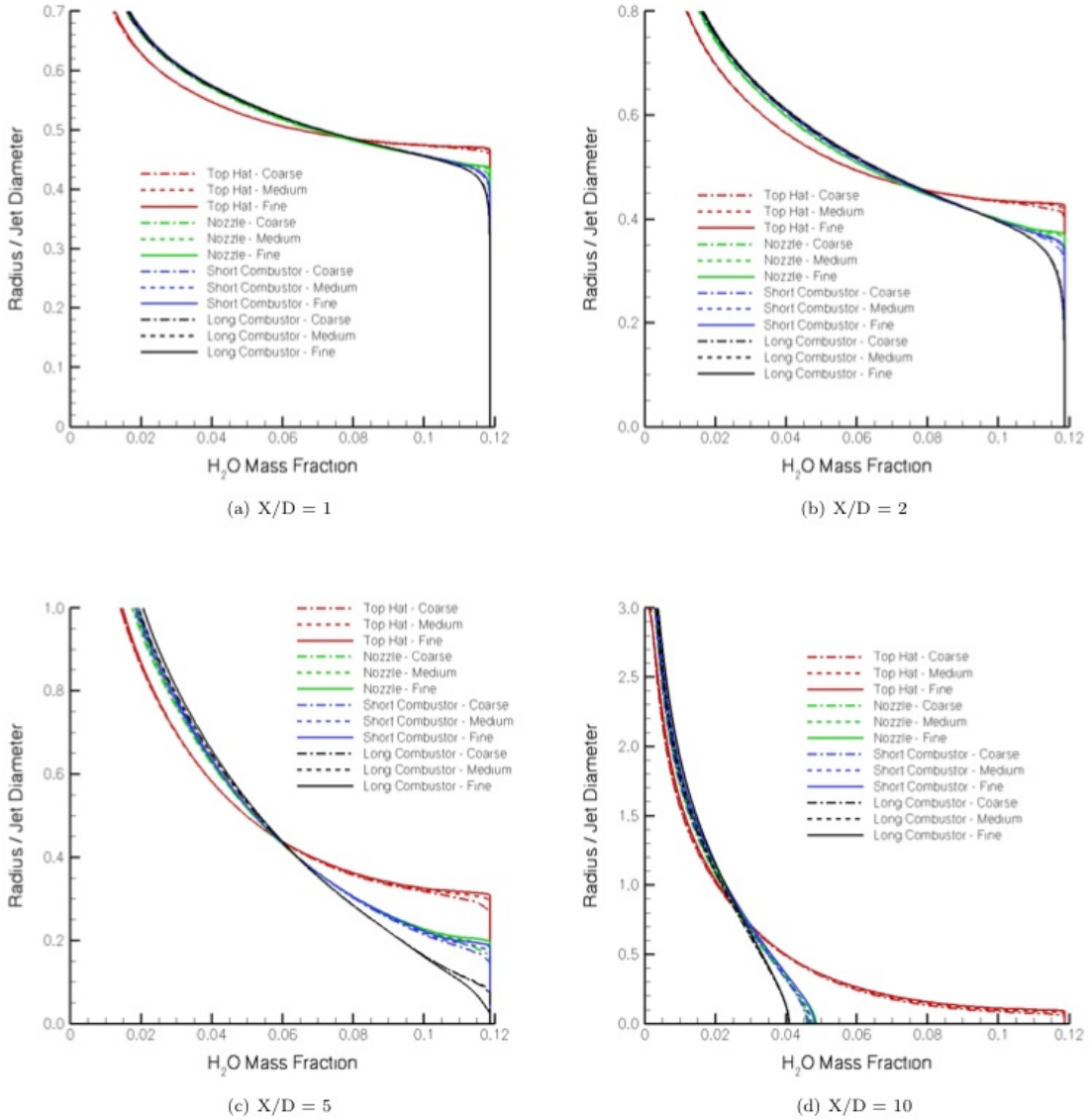

(a) X/D = 1

(b) X/D = 2

(c) X/D = 5

(d) X/D = 10

Figure 26. Non-Reacting, External-Flow H_2O Mass Fraction Profiles at Several Axial Locations

3.4 Reacting Case

The second case to be investigated is similar to the previous but with gaseous hydrogen flowing through the coflow nozzle at a rate of 0.0693 pounds/second. The facility combustor was operated at the same conditions used for the non-reacting, mixing-only case. These conditions give an equivalence ratio (based on the main jet and coflow) of approximately 1. For this calculation, the inflow to the coflow plenum was set to a subsonic, constant mass flow boundary condition. This boundary condition holds the composition, total temperature and mass flow constant and lets the velocity float. The total temperature of the hydrogen was set to 300 K based on the assumption that its temperature did not change from its ambient temperature storage tank. To reduce computational expenses, only the coarse grids were used for this case.

3.4.1 Reacting Internal Flow Calculations

As previously mentioned, the facility combustor operating conditions were the same as those for the non-reacting case (Table 5); however, since the external calculation would contain additional species (OH, H, O), the internal flow calculations were re-computed with the additional species included. In order to avoid any inconsistency between the chemical equilibrium of the input species composition and VULCAN's hydrogen chemistry model (the 7 species / 7 reaction model), the calculations were run with finite-rate chemical reactions. This resulted in nearly constant profiles with values that differed from those of Table 6 in the 6th or 7th decimal place. The exit profiles of flow properties are identical to those of the non-reacting case (Figure 20). The convergence for the reacting, internal flow calculations are given in Table 9.

Geometry	Coarse Grid
Nozzle	13.705
Short Combustor	7.832
Long Combustor	13.591

Table 9. Residual Drop in Orders of Magnitude - Internal Geometry, Reacting Cases

3.4.2 Reacting External Flow Calculations

As with the non-reacting case, a top-hat (uniform flow) nozzle-exit boundary condition was added to the external flow run matrix. All four of these cases proved to be unsteady. The source of the unsteadiness can be seen in the upper half of Figure 27 which shows a snapshot of the unsteady density contours in the near field. As with the non-reacting case, the jet entrains the ambient air flow and separates from the shroud at the corner point, creating a recirculating region on the face of the shroud. However, in this case, the flow sheds structures from the separation point. For all four of these cases, the solutions were initially run with a steady state algorithm and then switched to a time accurate algorithm. After allowing the unsteady flow field to establish, the solution was advanced further in time and the flow properties time averaged. The lower half of Figure 27 shows time averaged density contours.

The overall flow structure of the reacting case is similar to the non-reacting case, but the heat release from the chemical reactions introduces new features. Figure 28 shows time-averaged OH mass fractions and static temperature contours in the near field of the nozzle exit. The previously mentioned recirculation region pulls some of the hydrogen coflow towards the face of the shroud, creating a flame anchored to the face of the shroud near the

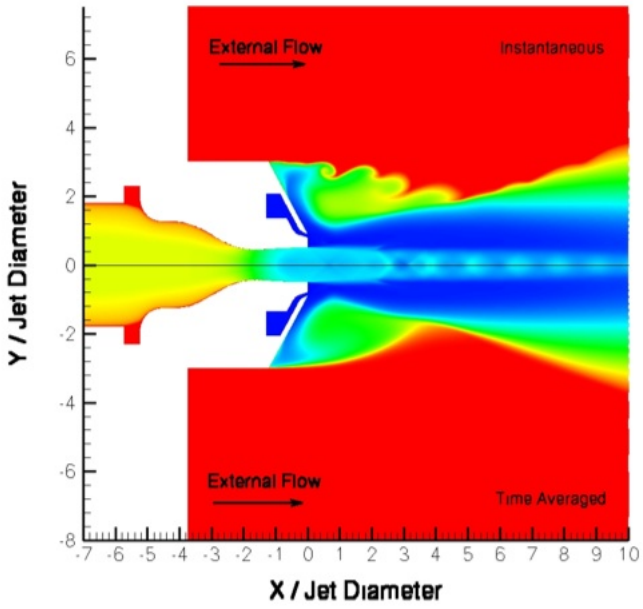

Figure 27. Instantaneous and Time Averaged Density Contours of the Nozzle-Exit Near-Field Flow, Reacting Flow Case

exit of the coflow. This flame extends downstream between the coflow and the ambient air. There is a second, detached flame between the coflow and the hot vitiated air jet. These two flames merge downstream of their initial reaction points. There is also a second small recirculation region adjacent to the rearward facing surface between the main jet and coflow.

The coflow injection and subsequent combustion affects the compression and expansion wave structure within the main jet. This can be seen in the centerline properties of Figure 29. The four nozzle-exit profiles produce very-near field (first 2 jet diameters) distributions that are similar. However, downstream of this, they show significant difference in both the amplitude and frequency of the waves. As with the non-reacting case, the long-combustor shear layer diffuses to the centerline first, the top-hat last and the nozzle-only and short combustor in between the other two. A comparison of the axial location where the shear layer diffuses to the centerline between the reacting and non-reacting cases shows that the reacting-case jet extends downstream much farther than the non-reacting-case jet. For the reacting case, the shear layer/centerline merge location is between 14.3 and 18.9 jet diameters downstream of the nozzle exit, while it is only 6.7 to 11.4 jet diameters for the non-reacting case.

Radial distributions of axial velocity, static temperature and H_2O mass fraction are shown at several axial locations in Figures 30-32. As with the non-reacting case, the solution using the long-combustor profile has the most diffusive behavior.

3.5 Summary and Conclusions

CFD calculations were made for a non-reacting and a reacting co-axial jet validation experiment to determine the sensitivity of the solutions to the profile in the exit plane of the vitiated-air nozzle. Four nozzle-exit profiles were used: a top-hat (uniform) profile, one

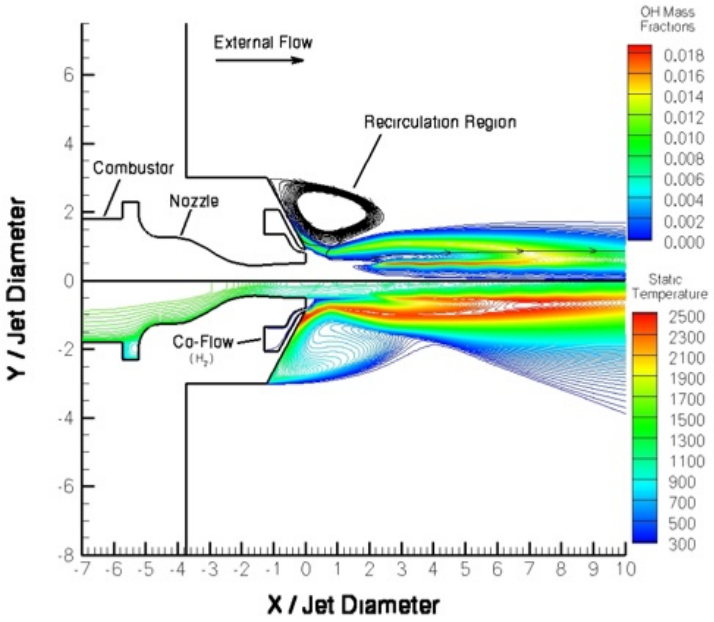

Figure 28. Reacting Flow Overview - Static Temperature in Kelvin

computed from the nozzle geometry, one computed from the nozzle geometry and part of the upstream facility combustor, and one computed from the nozzle and the complete facility combustor. In the non-reacting case, the solutions in the near field (within the first 4 jet diameters of the nozzle exit) were similar, with the top-hat profile showing the most difference. The location where the shear layer diffused to the centerline varied significantly between the cases, varying between 6.7 and 11.4 jet diameters downstream of the nozzle exit. In the reacting case, the solutions in the very-near field (within 2 jet diameters) were similar but then varied downstream. The different profiles affected the frequency and amplitude of the compression/expansion waves inside the slightly underexpanded main jet, producing different centerline distributions. As with the non-reacting case, the location where the shear layer diffused to the centerline varied significantly between the different profile solutions, varying between 14.3 and 18.9 jet diameters downstream of the nozzle exit. These results show that the nozzle exit profile affects the downstream solution and must be taken into account when using this experiment to validate a CFD code. Although one of the nozzle exit profiles included the calculation of the facility combustor, and hence is presumably the most accurate, the calculation used a uniform, post-combustion inflow and neglected any structures or additional flow field changes due to fuel injection and combustion. A comparison with experimental data, or a more involved CFD calculation, is needed to determine if this also needs to be included in a validation calculation.

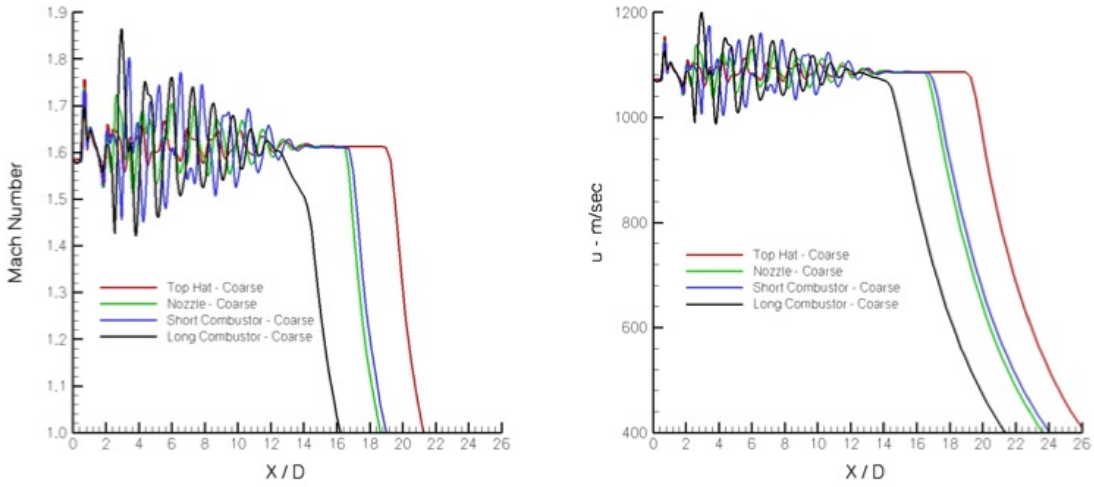

(a) Mach Number

(b) Axial Velocity

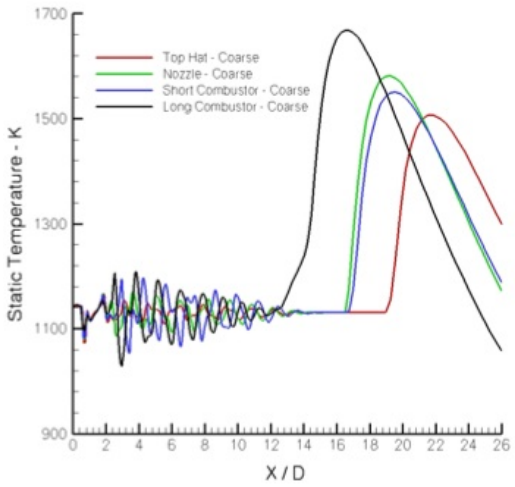

(c) Static Temperature

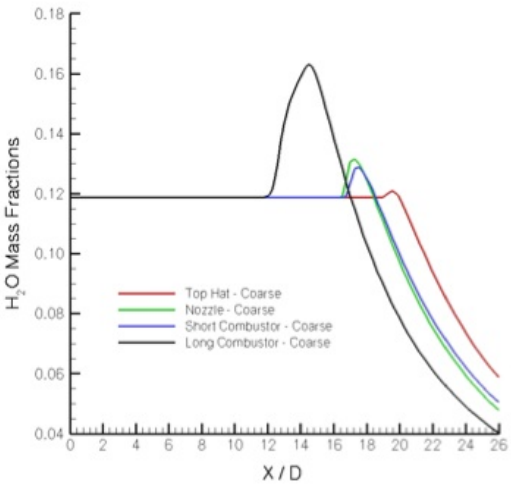

(d) H_2O

Figure 29. Reacting, External-Flow Centerline Distributions

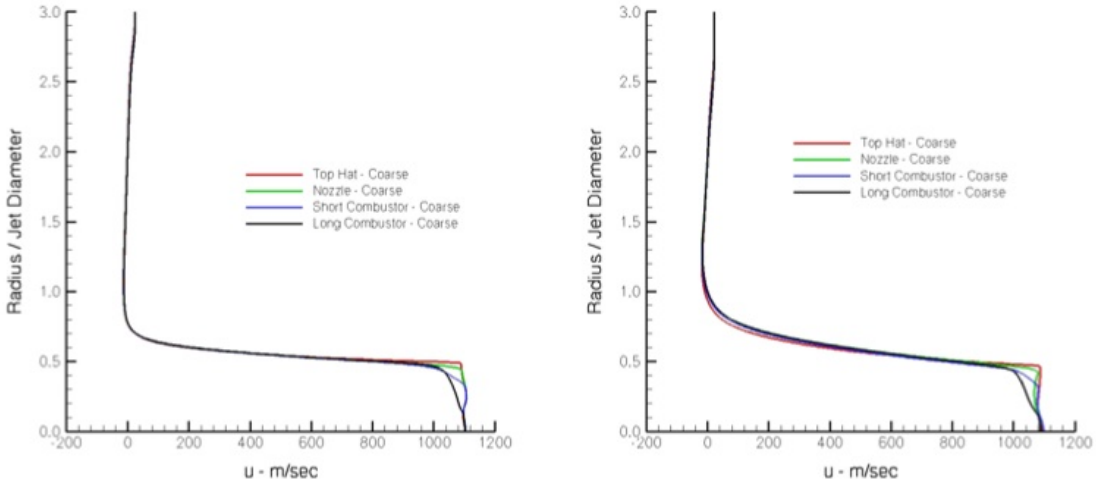

(a) X/D = 1

(b) X/D = 2

(c) X/D = 5

(d) X/D = 10

Figure 30. Reacting, External-Flow Axial Velocity Profiles at Several Axial Locations

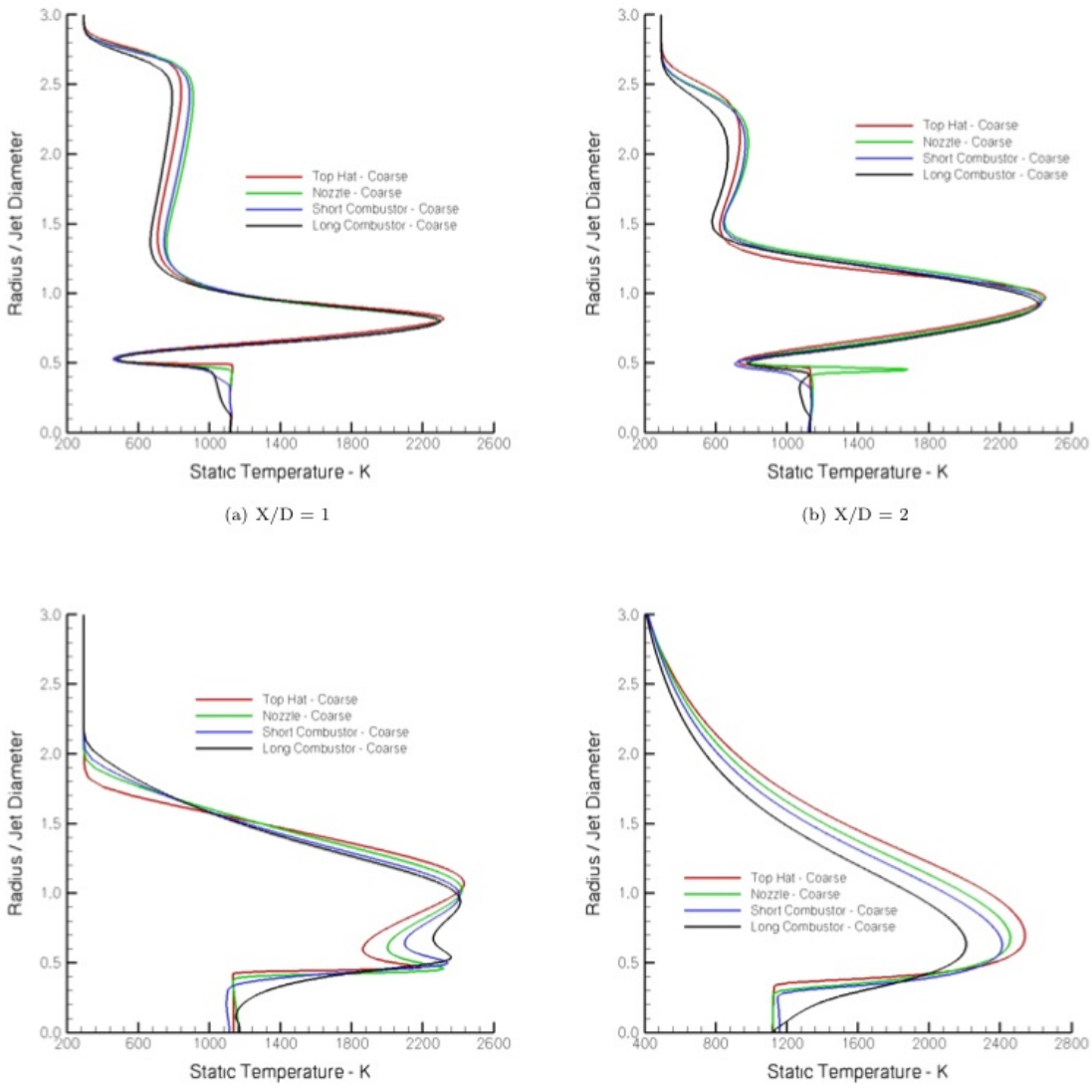

(a) X/D = 1

(b) X/D = 2

(c) X/D = 5

(d) X/D = 10

Figure 31. Reacting, External-Flow Mach Number Profiles at Several Axial Locations

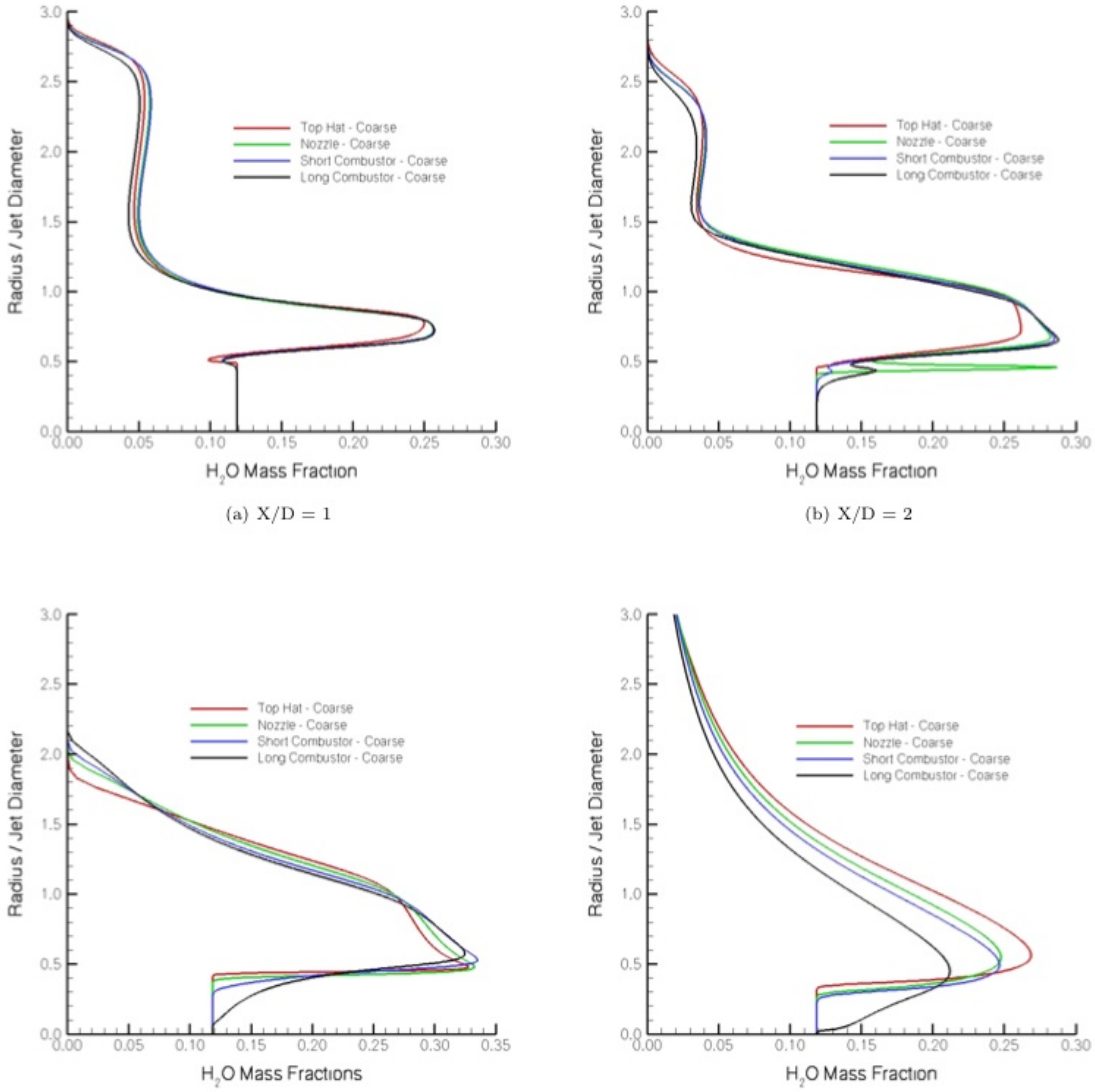

(a) X/D = 1

(b) X/D = 2

(c) X/D = 5

(d) X/D = 10

Figure 32. Reacting, External-Flow Mach Number Profiles at Several Axial Locations

4 CARS Temperature Measurements in the Supersonic Combusting Jet Experiments

Measurements were made in a combustion-heated supersonic axi-symmetric free jet from a nozzle with a diameter of 6.35 cm using dual-pump coherent anti-Stokes Raman spectroscopy (CARS) [36]. The resulting mean and standard deviation temperature maps are presented. The temperature results show that the gas temperature on the centerline remains constant for approximately 5 nozzle diameters. As the heated gas mixes with the ambient air further downstream the mean temperature decreases. The standard deviation map shows evidence of the increase of turbulence in the shear layer as the jet proceeds downstream and mixes with the ambient air. The challenges of collecting data in a harsh environment are discussed along with influences to the data. The yield of the data collected is presented and possible improvements to the yield of the data are discussed.

4.1 Introduction

Coherent Anti-Stokes Raman Spectroscopy (CARS) has previously been applied as a non-intrusive diagnostic tool in studies of supersonic combustion [3, 37–43]. An on-going project at NASA Langley Research Center is using CARS measurements to provide CFD modelers with fundamental data sets of the properties of supersonic combustion flows for the improvement of their flow models. Temperature measurements were made with N_2 CARS in a ducted supersonic combustion flow [3]. The same flow was later probed using dual-pump CARS and provided not only temperature measurements, but also species concentration of N_2, O_2, and H_2 [6, 7]. This flow was found to be difficult to model computationally and thus a new simpler flow was designed, namely a supersonic free jet with a coaxial injection of fuel (H_2). Studies of a small-scaled version of this newly designed flow were performed with Dual-Pump CARS and Interferometric Rayleigh Scattering (IRS) [14, 45]. IRS was used to measure two components of velocity. The current research effort aims to provide CFD modelers with a simplified flow with additional physical parameters measured simultaneously. The larger scale of the current experiment was used to increase the relative size of the flow length scales compared to the CARS and IRS probe volumes. Several methods from the discipline known as design of experiments were used to define the test and defend against experimental measurement systematic errors, to provide meaningful statistics, and to optimize the amount of data taken to the precision desired. The CARS instrument was characterized so that an assessment of the accuracy of the measurements could be made. As part of the experiment, two flow conditions were studied: combusting flow and mixing flow (no fuel). This section of the report describes only the mixing flow results, represented by mean maps of the measured quantities with CARS. The IRS results are presented in a section 5 of this report [46]. Because of the harsh environment of the test facility, the CARS instrument did not always yield reliable data. In this section the data yield are presented and the effects causing this lowered yield are discussed.

A secondary objective of the work described in this section is to discuss the challenges of applying the Dual-Pump CARS instrument to the larger-scale supersonic free jet to give insight on how these challenges were addressed or suggest how they could be addressed in the future. CARS is a laser-based measurement technique that obtains the Raman spectrum of the species present at the crossing of the focal points of three laser beams. The spectra contain temperature and species concentration information. Dual-Pump CARS allows species with Raman shifts in two spectral regions to be overlapped and so increases the number of species measured at once. In this study CARS is applied to a supersonic flow that differs from flows used by previous experimenters [3, 37–39]. The flow in this study is a free jet, where flows in previous experiments were ducted. This large-scale free

jet flow offers challenges because of the effect on the laser beams traveling long distances through variations in the index of refraction caused by the turbulent flow which has large temperature gradients. This effect on the lasers is referred to as beam steering and can change the laser beam direction and focus which can lower the data yield and increase the standard deviation of the temperature measurements. Another effect that can change the direction and focus of the lasers is the vibration caused by the uncontained supersonic flow on structures and mirrors within the test section. A large temperature variation within the flow created the challenge of having a large dynamic range for the detection of the CARS signal. Other challenges of this study included: the size of the study's measurement space (a 70 cm axial distance), ambient temperature changes within the test cell, and restricted access to the laser beam relay system during the experiment. The challenge of ambient temperature changes within the test cell was addressed by situating the lasers in a more stable environment outside the test cell. But this removal required a long path length for the lasers presenting additional challenges of maintaining alignment of the laser beams as the beam focus was translated in the flow, and power losses on the multiple mirrors required to reach the test cell.

4.2 Test Hardware and Facility

The experiments were performed in the Direct Connect Supersonic Combustion Test Facility at NASA Langley Research Center. This facility delivers vitiated air, the hot gas products of H_2, air and O_2 combustion in which O_2 has been added to have the same fraction (by mass) as in air. Vitiated air with an enthalpy equivalent to flight at Mach 5.5 was accelerated in a nozzle and discharged into the test cell at atmospheric pressure. The nozzle, described in section 2 and Ref. [21], created an axi-symmetric free-jet flow at Mach 1.6. A drawing of the nozzle is shown on the left of Fig. 33. The heated gas is delivered through the center nozzle with an exit diameter of 6.35 cm, while a concentric cone formed a coflow nozzle that was not used in this experiment reported herein. An infrared image of the heated gas being delivered from the nozzle can be seen on the right side of Fig. 33. Vertical lines in the infrared image are artifacts caused by reflections from the structure holding the optics for the CARS-IRS instrument. The flow rates of gases to the facility heater for the mixing flow condition were: 0.92±0.012 kg/s of air, 0.155±.005 kg/s of O_2, and 0.0147±.0004 kg/s of H_2.

4.3 Test Procedure

To fully characterize the flow field of the axi-symmetric jet, the measurement locations were chosen using design of experiment methods. The locations are shown in Fig. 34, where (0,0) is defined as the geometrical center of the exit of the nozzle and the axial distance increases in the direction of the flow. Because the flow was assumed to be axi-symmetric, most of the locations were chosen in half of a cross section of the flow. Locations outside this half cross section (triangles in Fig. 34) were chosen to check the symmetry of the jet and to assess the alignment of the CARS instrument with respect to the flow. More locations were placed in regions of flow believed to have high gradients in the values being measured, such as the shear layers. Because of a physical limitation of the beam relay system, the data set was split in two separate regions. These two regions are defined as the upstream region and downstream region are indicated in Fig. 34 by circles and squares, respectively. These two regions overlap at an axial distance of 40 cm. The locations within a given region were visited in a random order so that trends from environmental or instrumental sources would not affect the data set.

The number of samples taken per location was determined by the number required to achieve a pre-determined statistical uncertainty. Every sample for every location could not

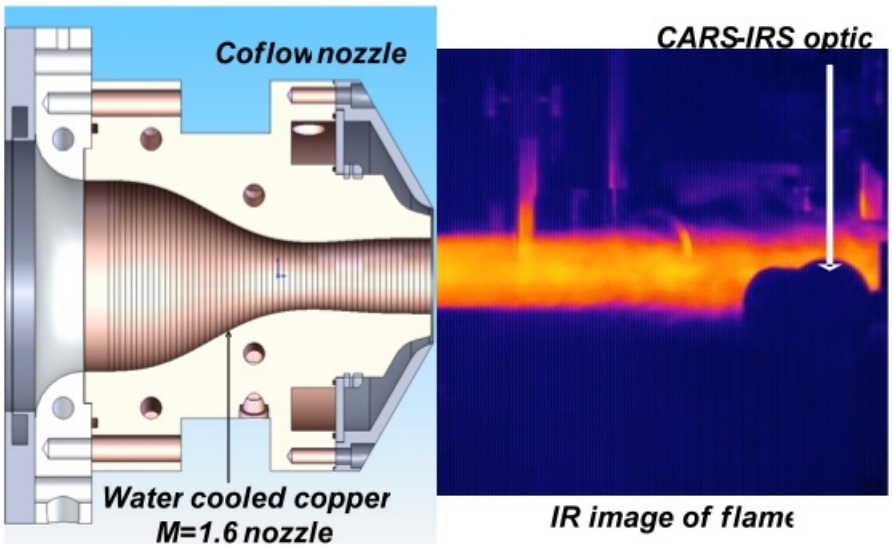

Figure 33. Test apparatus and flow field. Rendering of a section through the model (left hand side) and infrared image of an axi-symmetric free jet for the mixing case (right hand side). Part of the CARS apparatus is shown in the image.

be taken on the same run. Each run lasted 50 s, limited by the memory of the CARS CCD camera. The 20 Hz repetition rate of the laser allowed for data collection every 50 ms. Thus, 1000 samples were taken during each run, allowing 4 measurement locations to be visited each run, each having > 200 samples per location. These repeated samples at the same location allowed computation of various statistical means, variances, and covariances. Most measurement locations were visited during more than one run to defend against run-to-run trends from environmental or instrumental sources.

4.4 CARS Instrumentation

The Dual-Pump CARS instrument included a mobile cart [47] and was located in a room underneath the test cell to protect the lasers from the large temperature changes and vibrations within the test cell. The cart contained the three lasers required for CARS and IRS. An Nd:YAG laser emitted approximately 1 Joule of energy with a 10 ns pulse duration at a rate of 20 Hz and at a wavelength of 532 nm. A fraction of the energy from this laser, 250 mJ, pumped a broadband dye laser centered at 604 nm. This red laser had a FWHM of 12 nm and emits 20 mJ of energy. Then, 180 mJ of the energy from the Nd:YAG pumped the narrowband dye laser operating at 552.75 nm. This yellow laser had a FWHM of 0.3 cm^{-1} and provided an output of 20 mJ/pulse. Finally, 100 mJ of the Nd:YAG energy was used as the green beam for CARS and the remaining green energy was used in a pulse stretcher for IRS. More detail of the cart and the Rayleigh instrument can be found in Refs. [15], [13], and [48]. These three lasers were sent to the test cell though a hole in the test cell floor. In the test cell the lasers were relayed by a series of mostly 3 inch diameter mirrors mounted on a motor-driven beam relay system to the measurement point. This system allowed movement of the CARS measurement location in two dimensions, axially and radially, with respect to the flow. For the final two reflections of the beam relay system, 1 inch diameter mirrors were used for each laser separately. In the final reflection the two mirrors directing

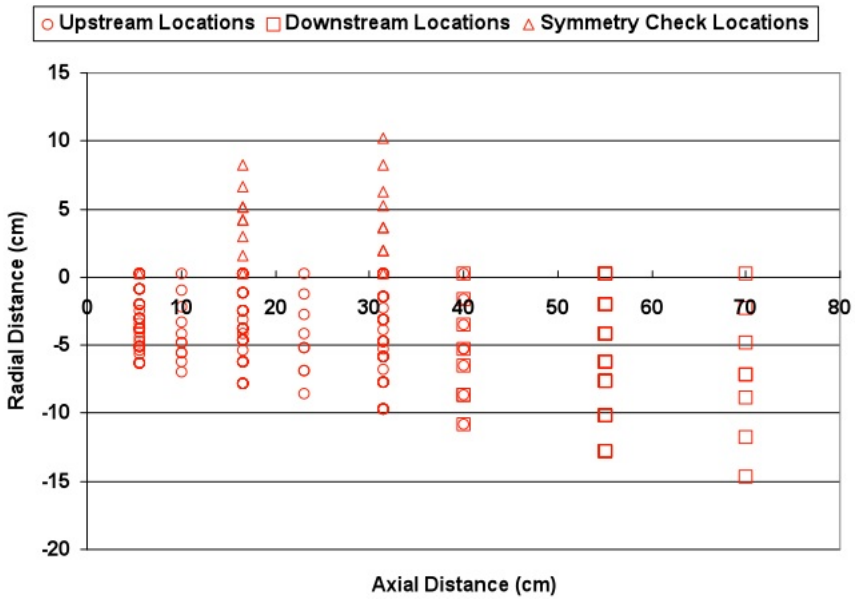

Figure 34. Test matrix used for experiments. Circles indicate the upstream region locations. The symmetry-check locations are indicated by triangles. The downstream region is indicated by squares. The different measurement locations were visited in random order.

the red and yellow laser beams were mounted on remotely controlled motorized mounts. These motorized mounts allowed small realignments of the laser beams without entering the test cell which was not accessible during testing. The laser beams, organized in a folded BOXCARS [50] phase matching geometry, were focused and crossed at their foci with a 40 cm lens, forming the CARS measurement volume. The measurement volume was measured with a knife edge and found to have the approximate dimensions of 90 micron diameter by 1.5 mm long. The energies of the lasers when they reach the measurement volume were approximately 15 mJ in red, 10 mJ in yellow, and 50 mJ in green. Energy was lost in the many mirror bounces and other optics as they were passed through the beam relay system from their sources on the cart. The CARS signal created at the measurement volume was collected on the other side of the flow. The signal was then passed through a beam relay system and focused at the exit of a one meter spectrometer with a 2400 line/mm grating. The slit of the spectrometer was open about 3.4 mm wide so that the resolution of the spectrum was limited by the size of the focus and not by the aperture of the slit. The slit was opened in this manner to prevent the signal from missing the slit and not entering the spectrometer because of beams steering effects described below. The spectra were taken by a CCD camera with 1340 pixels horizontally and 100 pixels vertically. The vertical direction of the CCD was summed, by groups of 33 pixels, into 3 rows (referred to as bins).

Data taken in the mixing flow of the supersonic jet suffered from motion of the focused signal from shot to shot with respect to the entrance slit of the spectrometer. In Fig. 35 the red dashed lines, labeled as flow data, show several spectra obtained during a single run in the mixing flow. These flow data are compared in Fig. 35 with spectra taken while there was no mixing flow, shown as blue dotted lines and labeled as “no flow data”. The flow data have much greater movement on the CCD camera than the no flow data. There are multiple possible sources of this movement. First, the flow could have caused the structure holding the mirrors and the mirrors themselves to vibrate and change in shape and location.

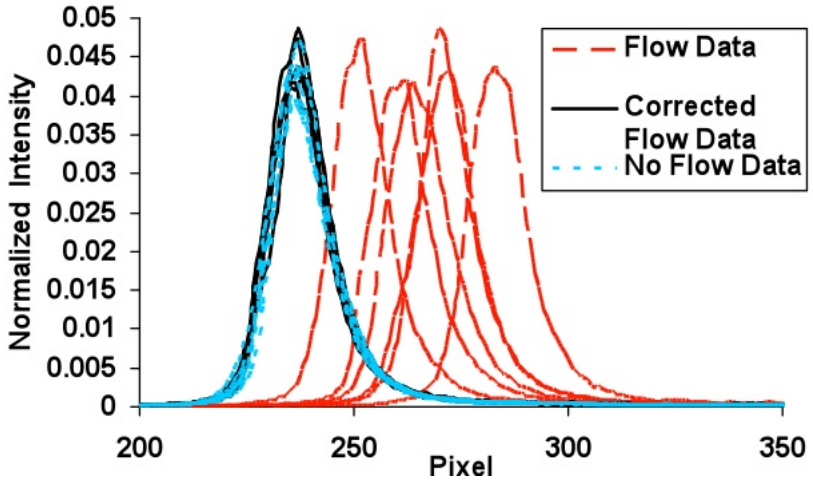

Figure 35. N_2 peaks from CARS spectra. N_2 peaks of CARS spectrum, red dashed lines, taken in supersonic jet at the mixing condition compared with N_2 peaks taken as reference data with no flow, dotted blue line, and N_2 peaks taken in the jet corrected during data analysis.

This change of the mirrors and structure is evidenced by the CARS signal moving from its location on the CCD array under no flow conditions to another location while flowing and remaining in this offset position after the flow stopped. Second, a contributing factor to the movement of the signal could have been the temporal and spatial variation of density in the hot, turbulent jet. Since different densities of gas have different indices of refraction, and since a gradient in index of refraction changes the angle of propagation of light, a gradient of density of the gas can change the direction of the beams.

The motion of the CARS signal was reduced by the addition of two 1 meter focal length relay lenses in the path of the CARS signal but still some motion of the signal remained. The vertical motion of the signal created the potential for loss of signal on the CCD array. In defense against this vertical motion the signal was placed into the center of the 3 vertical bins. This allowed motion of the signal both up and down into the other bins without loss of signal. As previously mentioned, after some runs the signal location permanently changed. In this event, the motorized mirror in front of the spectrometer was adjusted to direct the CARS signal back to the center bin. Originally, it was intended to increase the dynamic range of the instrument by dividing the signal over two or more bins. The third bin would be used for background subtraction. However, movement of the signal vertically with respect to the CCD during the runs prevented the use of this approach. Instead, a neutral density filter on a remote switch was added into the signal path to vary the dynamic range of the system. The filter was used in low temperature regions of the flow to prevent saturation of the CCD camera. The filter was removed in hotter parts of the flow to improve the signal-to-noise ratio. More details about the structure holding the mirrors (beam relay system) and the instrumental setup up can be found in Ref [15].

4.5 CARS Data Analysis

The CARS data collected in this experiment were analyzed using both in-house written software and a modified version of the widely used Sandia CARSFT code [51]. Before the spectra were compared to theory in CARSFT, they were processed using in-house codes.

The first step was to subtract background light from the spectrum. The background light was either collected in one of the 3 CCD bins where no CARS signal was present or in a spectrum obtained with the red laser beam blocked, preventing the creation of the CARS signal. Next, the spectra were corrected (approximately) for the motion of the focused signal at the entrance to the spectrometer. This correction was made by shifting each spectrum, in wavelength, to match spectra taken while the jet was not operating (no flow data). Using the N_2 spectral peak, the spectra were matched at the location in wavelength where 20% of the spectras maximum intensity occurred. This location in the spectrum was used because it changes the least in intensity as temperature changes. The results of this shift are shown by black solid lines in Fig. 35. Next, the shape of the broadband dye laser spectrum was removed from the spectra by dividing by a "non-resonant" reference spectrum. Non-resonant reference spectra were obtained by performing CARS in an argon gas cell (which has no resonances in this spectral range) each day of testing prior to the start of testing and again upon the completion of testing. Finally, the square root of the spectral intensities was taken to convert from intensity to susceptibility (for comparison with CARSFT theoretical spectra).

The processed CARS spectra were analyzed using a version of the Sandia code CARSFT that was modified by Lucht et al [4] for the use of Dual-Pump CARS and which was further modified by OByrne et al [37]. This code computes theoretical spectra convolved with an instrument function, which is a double Gaussian function optimized to produce a best fit of room temperature theoretical spectra to experiment. The instrument function accounts for the spectral line broadening from several sources, including the finite width of the focus of the CARS signal at the entrance to the spectrometer and the finite resolution of the CCD detector. CARSFT subsequently compares these theoretical spectra to the experimental spectra, iterating on temperature and composition (N_2 and O_2 mole fraction) to minimize an objective function, χ^2. χ^2 is a goodness-of-fit parameter calculated using the formula $\sum_k \frac{(theory(k)-data(k))^2}{data(k)}$, where k is the pixel number, or wavelength of the spectrum. The theoretical values in this formula have been normalized by setting their maximum value to one. An arbitrary scaling factor is applied to the data for best fit to the theory. Values of χ^2 less than one generally produce reasonable fits to the data, judged by eye. Fits to data with χ^2 greater than one have large discrepancies by visual inspection.

To provide CFD modelers with the uncertainty in the CARS measurements, the CARS instrument was characterized in a well understood flat flame burner called a Hencken Burner. This type of burner has also been used by Hancock et al [52] and others for characterization of CARS systems: data are compared to adiabatic equilibrium calculations of the flame products. The fuel-to-air ratio was varied to obtain a range of temperature and species concentrations. These measurements were made with the CARS system in place in the test cell but the data were not fully analyzed until some time after all the experiments had been completed. The accuracy of the results can be seen in Fig. 36 showing the calculated values of temperature and species concentration compared with means of 1000 CARS measurements.

The largest percentage difference of the measured CARS temperature from the calculated temperature is 7.4% and the average percentage difference is 3.2%. The largest percentage difference of the O_2 concentration is 31% and N_2 is 7.2% percent. The errors in the CARS measurements can be attributed to several possible sources: uncertainty in the flow rates of the gases, spectral overlap of the N_2 and O_2 spectra, and polarization of the lasers. After the flat flame burner data and mixing flow data were collected, evidence was discovered that the lasers were not all linearly polarized in the same direction, as intended. First the broadband dye laser was observed to be slightly elliptically polarized, when analyzed with a linear polarizer. The CARS signal also showed evidence of elliptical polarization and the orientation of its maximum component of polarization, when measured at the spectrometer, was approximately 45 degrees from the expected direction. For dual-pump CARS a change

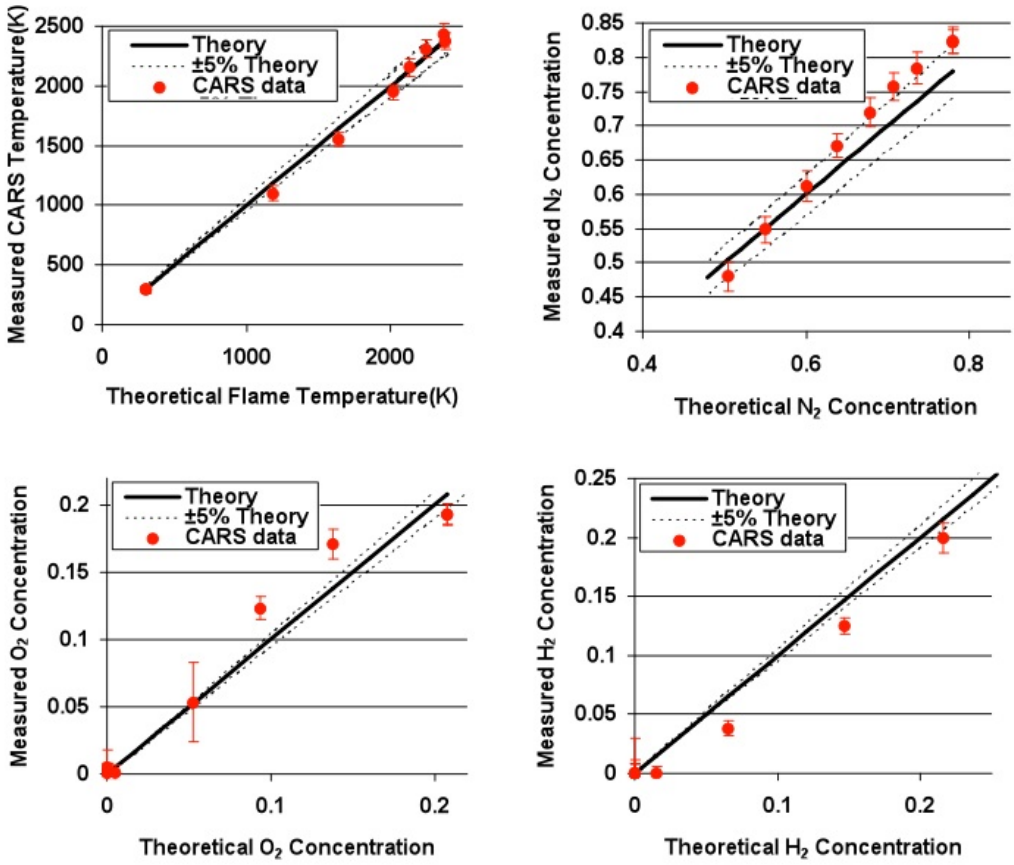

Figure 36. Calculated values versus CARS, measurements taken in flat flame burner with hydrogen fuel. Red dot indicate mean CARS measurements and the error bars indicated the standard deviation. The solid lines show the calculated trends and the dashed lines show 5% different from the calculated values in the flame burner.

in polarization of the input beams affects the relative intensity of the spectra for different species, as discussed in Ref. [5]. Thus, these elliptical polarizations could cause incorrect measurement of the species concentrations. One standard deviation of the 1000 individual measurements is used as a measure of precision and is shown in the plots in Fig. 36 as error bars. The single-shot precision of temperature averaged over all measured temperatures is 71 K, similar to the value obtained by OByrne et al. [37] In the temperature range (300 to 1000 K) for the mixing flow study described below the precision is between 25 K and 65 K respectively - similar to Ref. [54].

4.6 Results and Discussion

The results of the mixing flow experiment will be presented in this section and will focus on the temperature measurements. Since the errors in the composition measurements were on the same order as the variations in N_2 and O_2 composition in the flowfield, the composition data are not reported. Figure 37 shows the mean of temperature in the form of a contour plot. This plot was generated using the grid of the measured mean values at the locations show in Fig. 34. The temperature is 1010±49 K at the first measurement location

downstream of the nozzle exit (5.5 cm) and 0.25 cm from geometric center. The highest temperature gas is indicated by red in the figure. This high temperature starts with the same width as the diameter of the jet (6.35 cm) and slowly narrows downstream as the heated gas mixes with the ambient air. The mixing layer, in the 500 K to 700 K range indicated by green, grows as it moves downstream. The blue color indicates the ambient air temperature of 300 K and shows the boundary of the jet flow. According to the measurements made in the flat flame burner at 1100 K, the mean temperature measured with CARS may be lower than the actual temperature by 100 K. This indicates that the mean temperatures measured near 1000 K may be lower than the actual temperature as much as 100 K. Ambient room temperature, 300 K, has a higher accuracy. The other temperatures in-between probably have higher accuracy as room temperature is approached.

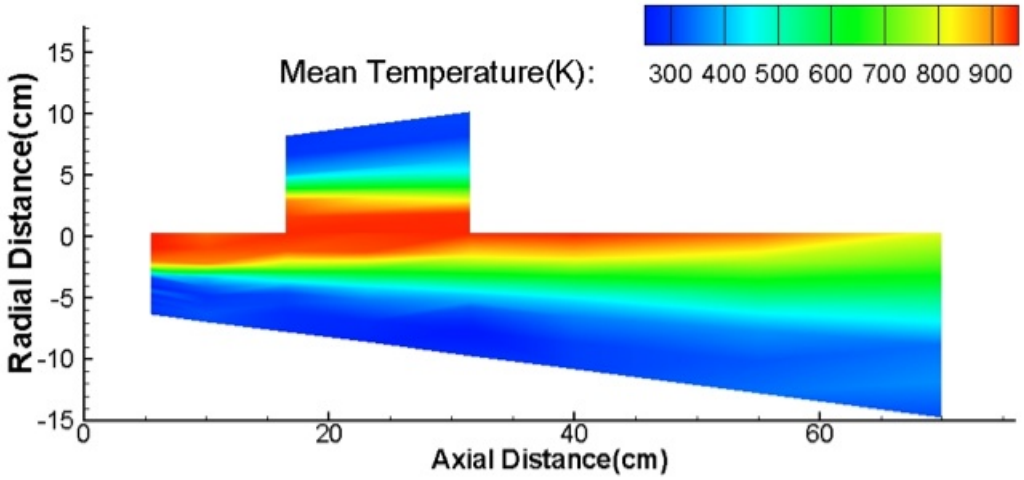

Figure 37. Contour map of mean CARS temperature data taken in an axi-symmetric free jet. Radial Distance versus Axial Distance is plotted in centimeters with respect to (0,0) which is the location of the center of the nozzle exit.

Figure 38 shows a contour plot of the standard deviation of the temperature, in Kelvin. The standard deviation in the plot has been corrected for the CARS instrument single-shot precision. This correction was calculated by taking the difference of the squares of the measured standard deviations and the single-shot precision and then taking the square root of this value. The single-shot precision was measured for temperatures in the flat flame burner, which was assumed to be steady in all flow variables. The single-shot precisions for temperatures not measured in the flat flame burner were found by using a linear interpolation between measured temperatures. In Fig 38, the highest standard deviations of temperature, of about 110 K, are seen in the mixing layer regions. This mixing layer region is shown in the temperature map in Fig. 37 as a transition from 950 K to 650 K. The mixing layer increases in width as it progresses downstream. In the core of the heated flow and in the ambient air, the standard deviation decreases to a range of 50 K to 70 K indicating steadier flow conditions.

The standard deviation map in Fig 38 shows the combined effect of the unsteadiness of the flow and random errors in the instrument above levels experienced in the quiescent Hencken burner. One such error is related to shot-to-shot changes in the width of the CARS spectra caused by changes in the focusing of the CARS signal at the entrance to the spectrometer. Variation in the focus of the CARS spectrum on the CCD changes the width of the instrument function of the detection system. If a constant instrument function width

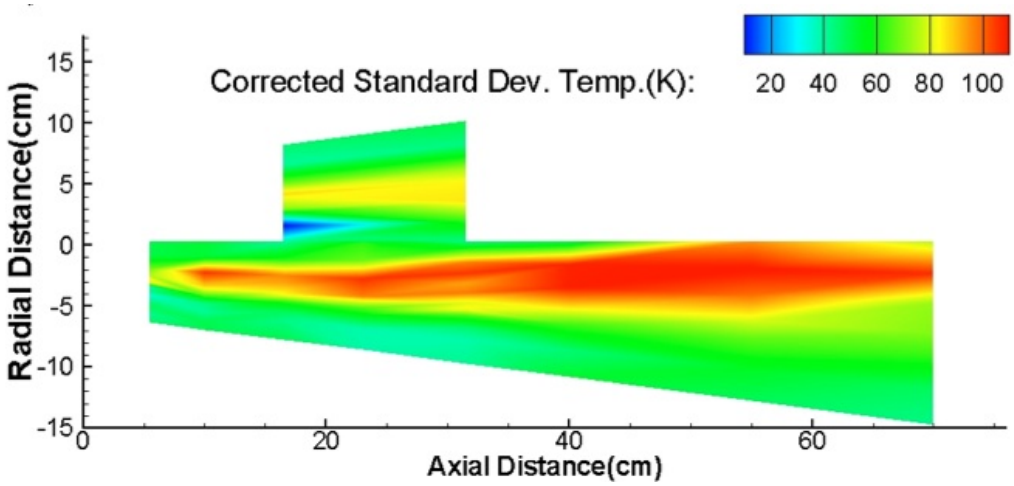

Figure 38. Contour map of CARS temperature corrected standard deviation data taken in an axi-symmetric free jet. The standard deviation has been corrected by the CARS instrument precision.

is used in the analysis this variation in focus leads to erroneous changes in temperature. For the range of temperatures measured in this experiment, 300 K-1000 K, the temperatures obtained using CARSFT are mainly determined by the width of the CARS spectra. Fitted temperatures above 1000 K are sensitive to a combination of the widths of the spectra and the ratio of the intensity of the second vibrational peak to the first vibrational peak. Figure 39 demonstrates shot-to-shot changes in the observed width of the CARS spectra, which lead to erroneous variations in temperature. The spectra in the figure shown with solid lines were taken during operation of the supersonic jet in immediate succession, 50 ms apart. These spectra were obtained while the jet flow was operating, but with the CARS measurement volume located well outside the jet flow, in the ambient air. The spectra in Fig. 39 vary significantly in width. This width variance is best seen at the half maximum indicated by the arrows in the figure. The variation of the width causes spectra to fit to temperatures both above and below the expected ambient, as indicated in the figure caption. For comparison, a reference CARS spectrum taken with the jet flow off in ambient air is shown in the figure as a dashed black line.

The change in width seen in Fig. 39, while temperature stays relatively constant (room temperature), is caused by a variation in the focus of the CARS signal at the entrance to the spectrometer. This change of focus could be caused by the movement of the location of the beams crossing. If the location of beams crossing changes, then the distance from where the CARS signal is created to the collimation lens changes. This change in distance to the collimation lens would lead to a change of the focus at the entrance of the spectrometer. Another possible source of change in focus of the CARS signal is the density change in the turbulent gases in the jet as the CARS signal passes through. A density change could change the index of refraction and act like a lens. A lens-like affect could change the collimation of either the input CARS beams or the signal beam, changing the focus at the entrance of the spectrometer.

The effect of a change in the width of the instrument function on the fitted temperature depends on the temperature at which the spectrum was measured. Figure 40 shows the effect of fitting theoretical spectra at various temperatures to theoretical spectra computed assuming a 25% larger instrument function width. The plot shows that, as the temperature

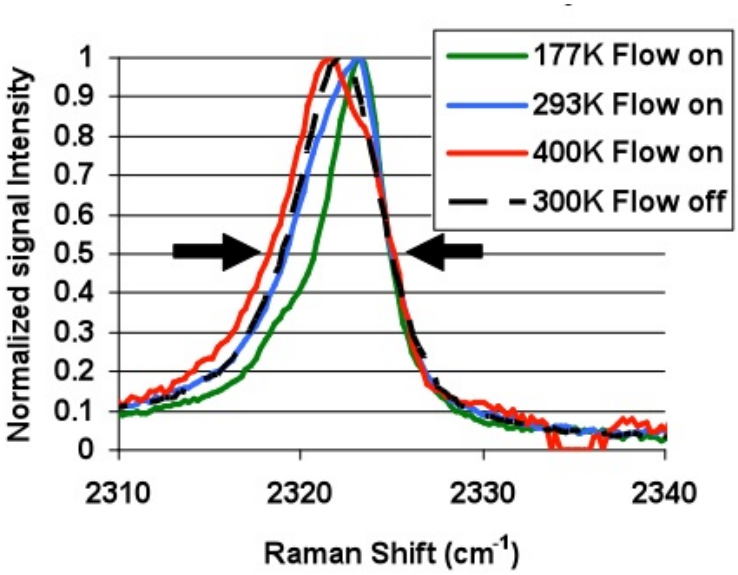

Figure 39. N_2 peak of CARS spectra comparing FWHM in ambient air (300 K) with flow on and off. Normalized signal intensity plotted against frequency (units are wavenumbers) of N_2 peaks of CARS signals. Green showing a narrowed 300 K spectrum fitted to 177K. Red showing a widen 300 K spectrum fitted to 400 K. Compared to blue and black fitted to the near room temperature with flow on and of respectively.

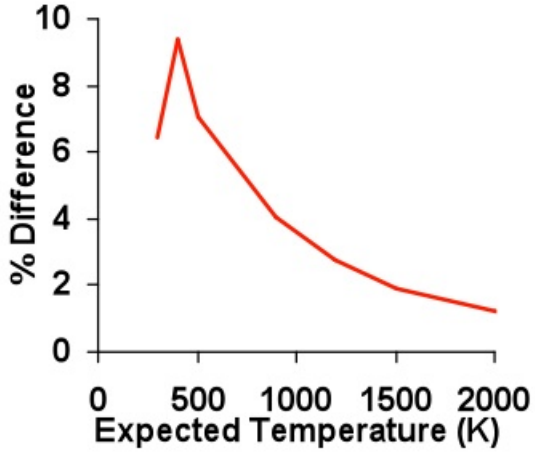

Figure 40. The effect of fitted a CARS spectra with a 25% larger instrument function width. Percentage difference of the original temperature of the spectrum to the fitting temperature versus the expected temperature. The percentage difference decreases with higher temperatures.

increases, the percentage difference between the fitted temperature and the known temperature decreases. The trend of increasing accuracy at higher temperature is mostly due to the

increase in population of the second spectral peak of N_2. A bias in the mean temperature to a higher temperature would have occurred if the signal was focused as tightly as possible at the entrance to the spectrometer, since any change in focus during the tests would have increased the instrument function width. In ambient air, with the jet flow off, the CARS signal was slightly defocused allowing both focus and defocus of the signal to occur. Thus, the mean values of the temperatures in ambient air did not show any bias. Unfortunately the change in width of the instrument function is not consistent or predictable on a shot-by-shot basis, because it is caused by random fluctuations in the flow. Therefore standard deviations in the supersonic jet flow presented in Fig. 38 may be overestimated, especially in colder regions of the flow, because, although they are corrected for instrument precision, this correction does not include the effects of change in signal focus at the spectrometer entrance.

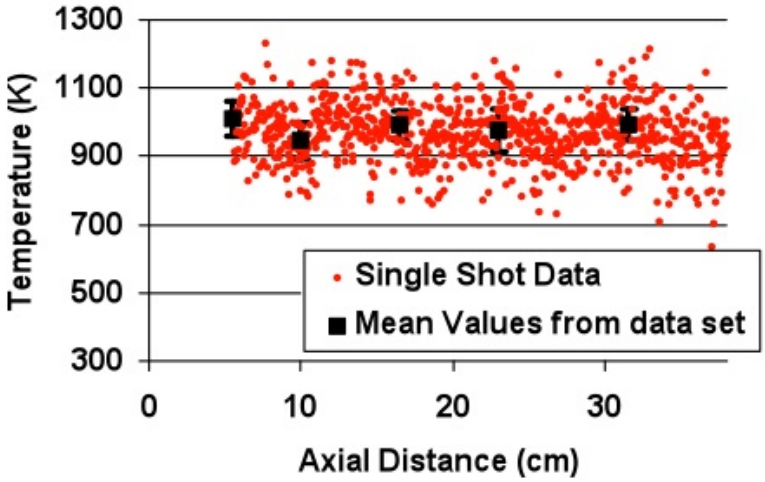

Figure 41. CARS temperature along axis of jet. Single shot temperatures, shown in red, from an axial scan is compared with mean temperatures, shown with black squares, error bars indicating corrected standard deviation of the means.

Another view of the CARS temperature data is offered in Fig. 41, in which single shot data (data from individual laser pulses) are shown in red. These data points were all taken as a scan during one run. This scan was collected along the axis of the jet for half of the measurement space (the upstream region). The data from the scan are compared with mean values of data acquired with the test matrix, shown as black squares. The error bars in the figure represent the corrected standard deviation for the mean values. The mean values follow the trends of the single-shot spectra shown, for example at the axial distance of 10 cm where both the mean and the single shot data show a dip in the measured temperature. This dip in temperature may indicate a shock wave or expansion affecting the temperature at this location.

As mentioned in the test procedure section, the data were taken in two regions due to constraints of the beam-relay system. In the one month break between the upstream (including the symmetry check locations) and downstream data set regions minor modifications were made to the facility. These changes raised the measured stagnation pressure in the combustion chamber by nearly 7%, even though the same flow rates were used as before. This change in pressure was accompanied by an increase in temperature measured by CARS: this change can be seen in Fig. 42. The figure compares the mean values of temperature at an axial distance of 40 cm where the upstream region overlaps the downstream

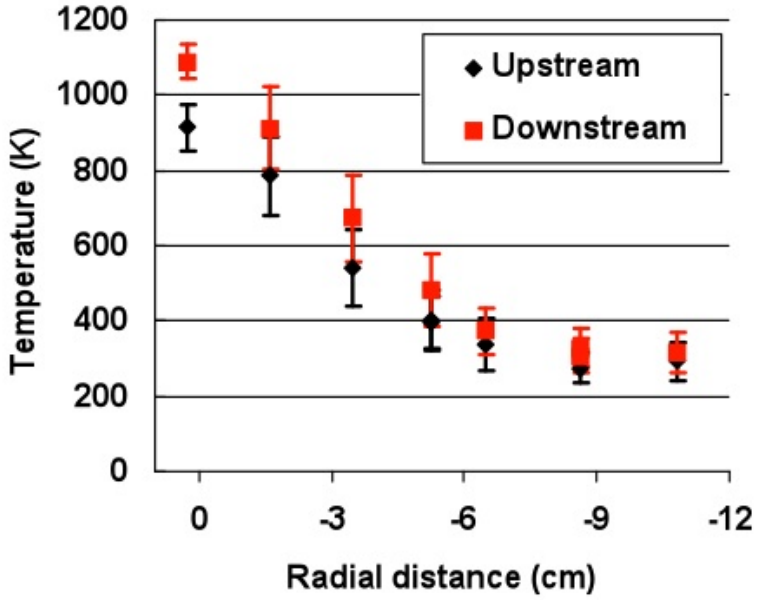

Figure 42. Temperatures taken at the overlap (40 cm) of the upstream and downstream measurement region. Temperature versus radial distance is plotted. Black diamonds in the plot indicating the measurements taken with the upstream locations and red squares indicating the measurements taken with the downstream locations. Error bars indicate corrected standard deviations.

region. The standard deviation at each measurement location is shown by the error bars in the graph. The statistical uncertainties in the means (not shown) are about an order of magnitude smaller than the error bars because these are averages of hundreds of individual measurements. The temperature increase from the downstream region, shown as red squares, compared to the upstream region, shown as black diamonds, is much larger than the statistical uncertainties in the means. This indicates that the change made to the facility changed the properties of the jet flow. Because of this difference in the flow conditions, the two regions should be considered by computational fluid dynamists to be two separate data sets. Note this difference is also present in the plots in Figs. 37 and 38, but the data sets have been averaged together at the 40 cm axial distance.

Table 10 shows the percentage of the data that could not be analyzed because of several factors. These factors are listed in the columns of Table 10 and are detailed below: camera saturation, low signal intensity (below 100 counts), laser-induced breakdown of the gases in the measurement volume, or other factors that resulted in poor fitting to theory. Each factor contributing to data removal is separated into percentages removed for the upstream region, downstream region, and entire data set.

The CCD array of the camera has a saturation threshold. CARS spectra for which a range of pixels exceed that limit are considered saturated. Saturated spectra cannot be fit with the analysis code because a critical part of the spectrum has an unknown intensity. Therefore these data were removed from the data set. The fraction of saturated spectra was the same for upstream and downstream data sets.

Breakdown of the gas sometimes occurs at the location of the beams crossing. At their crossing, the lasers are focused on top of one another and their combined energies can exceed the threshold of the energy at which the gases or dust particles will dissociate. This

	Saturated	Breakdown	Signal < 100 counts	χ^2 >1 (Poor fit)	Yield
Upstream	7.3%	0.3%	3.3%	29.1%	60.0%
Downstream	6.9%	0.2%	9.1%	44.6%	39.3%
All Data	**7.2%**	**0.2%**	**4.9%**	**33.3%**	**54.4%**

Table 10. Percentages removed from data set and total yields. The percentages of data removed for the upstream region, downstream and total data set because of saturation, breakdown, low signal counts, and $\chi^2 > 1$ (poor fit). The last column shows the yields for the data set.

dissociation causes a spark or breakdown. The spark of light is combined with the CARS signal on the CCD array. This effect only contributes to a very small amount of data loss and was the same for upstream and downstream data regions.

Spectra with peak intensities below 100 counts were removed from the data set prior to fitting. The signal-to-noise ratio of these spectra was so low that when the square root of the signal was taken for fitting with CARSFT, it was indistinguishable from the noise. Signal counts below 100 were more frequent in the downstream region indicating an overall lower CARS signal intensity. During the days that the downstream region data was collected, the CARS signal intensity with the flow off was at the same intensity level as the upstream data set. Therefore, the reduction in CARS signal intensity in the downstream region is attributed to effects that occur in response to the flow. Effects that could decrease the CARS signal intensity because of the flow include higher temperatures and increase in turbulence, longer path through turbulence, or more movement of the mirrors. All of these effects would cause more movement of the beams and decrease or eliminate the size of the beams overlap region. There are two possible reasons that the CARS signal intensity decreased beyond an axial distance of 40 cm. Increased beam steering could have been caused by the natural trends of increased turbulence and larger jet diameter further downstream. Alternately, the instrument or facility could have changed between the measurements. To distinguish between these two possibilities a comparison of the yield at the overlap of the measurement region at an axial distance of 40 cm was made. The yield for the upstream region is 21% higher than for the downstream region, even though the measurement location was identical. Along with the change made to the flow facility that increased the temperature in the interim between the measurements of the two regions, a change was also made to the CARS instrumental setup up. This change was the increase of the path length to the measurement volume. This was done by the addition of two mirrors in the path of delivery of the lasers to the measurement volume. These additions could have decreased the stability of the structure and increased the movement of the beams, decreasing the signal level during operation.

Most of the data removed from the data set were from a criterion set on the χ^2 value. Removing data that fitted with $\chi^2 > 1$ effectively removed all spectra with peak signal intensities below 1500 counts indicating that the signal-to-noise ratio is too low for these spectra. The requirement of having $\chi^2 < 1$ removed more data from the downstream region than the upstream region. This indicates a higher frequency of signal lower that 1500 counts in the downstream region. The decrease in the CARS signal intensity for the downstream data region follows the trend from the signal below 100 counts criterion.

The decrease in yield at 40 cm, where the upstream and downstream regions overlap can also be seen in Fig. 43. Figure 43 shows the percentage yield at each measurement location in the form of a contour map. Not only can a sharp drop in the yield be seen between the upstream and downstream data region but also (by comparison with Fig. 37 and 38) the effect of temperature on the signal intensity can be seen. The yield decreases at locations in the flow where the temperature is higher. The dependence of the yield on

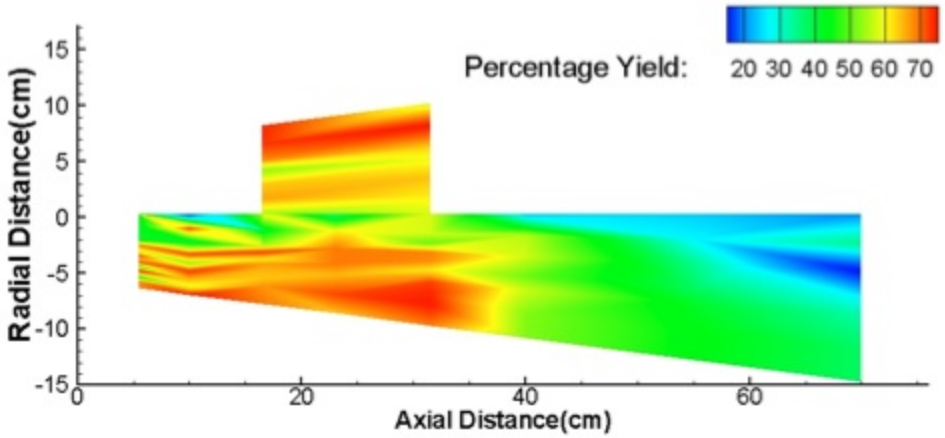

Figure 43. Contour map of percentage yield per measurement location. Yield is dependent on temperature. The upstream region shows more yield than the downstream region.

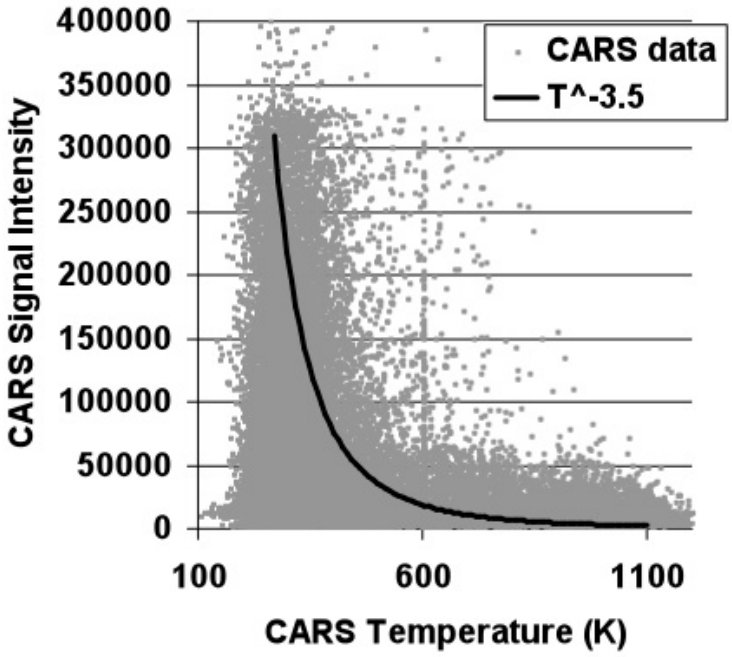

Figure 44. Dependence of CARS signal intensity on temperature. CARS data points shown in gray and the theoretical dependence of intensity on temperature, arbitrarily scaled.

temperature can be attributed to the dependence of the signal intensity (counts) on the temperature as shown in Fig. 44. All the data points used in the results are shown as gray data points in the figure. The data are compared to a theoretical trend of signal intensity versus temperature, as used in Ref. [55], $T^{3.5}$, arbitrarily scaled, is shown as a line in black. The data points generally follow the trend but even at ambient room temperature the signal intensity range is very broad, showing the effect of the beam misalignment to be greater

than the temperature effect in most instances. This temperature effect on signal intensity was shown to not create a large bias in the means of temperature in a previous report on this data set by Danehy et al. [20]

4.7 Conclusions

In conclusion, measurements made with dual-pump CARS in a supersonic symmetric free jet mapped the mean and standard deviation of the temperature field. The data were collected with a yield of 54%. About 7% of the data were lost because of signal saturation. The majority of the data loss was due to low signal intensity, 38%. This percentage is the addition of the percentage of spectra removed because of signal below 100 counts and the goodness-of-fit criteria of χ^2 >1. Most of the low-signal data were lost because of CARSFTs inability to distinguish the signal from the noise. Movement of the beams contributed to a change in focus of the CARS signal at the entrance of the spectrometer. This change in focus did not affect the mean values of the temperatures since the CARS signal began slightly defocused so the change in focus was equally likely to increase or decrease the temperature. The change in focus did, however, increase the standard deviations and could not be decoupled from the standard deviation of temperature in the flow. Changes were made to the facility between the measurements of two regions of the flow defined as upstream and downstream. These changes to the facility changed the flow properties of the jet. Because flow conditions for the upstream region and downstream region are different, the regions should be considered separate data sets.

It is recommended to make the following changes to increase the quality of future data sets. To decrease the loss of data from saturation of the CCD, the dynamic range of the CARS instrument needs to be increased. To decrease loss of signal due to beam movement by structural vibration, the beam relay structure needs to be more rigid. To address the loss of signal intensity caused by beam steering by refractive index gradients, the phase matching could be changed to planar BOXCARS, ensuring that at least two beams remain overlapped at the focus. If the spectra were better resolved, then the variation in focus of the CARS signal at the entrance of the spectrometer would affect the temperature less. To improve the accuracy of the CARS concentration measurements, polarizers should be implemented in each input beam, directly before the CARS focusing lens to eliminate any possible elliptical polarization. A polarizer should also be placed in the signal beam before the spectrometer. Also in the experiment, a test case having a larger difference of species (eg. O_2) from ambient air would provide better distinction between facility air and ambient air. In the future, this data set will be combined with the Rayleigh data set so that the relation of temperature and velocity can be quantified for the benefit of CFD modelers.

5 Spatially and Temporally Resolved Measurements of Velocity Using IRS in the Supersonic Combusting Jet Experiments

This section presents simultaneous measurements at multiple points of two orthogonal components of flow velocity using a single-shot interferometric Rayleigh scattering (IRS) technique [46]. The measurements are performed on a large-scale Mach 1.6 (Mach 5.5 enthalpy) H_2-air combustion jet during the 2007 test campaign in the Direct Connect Supersonic Combustion Test facility at NASA Langley Research Center. The measurements are performed simultaneously with CARS (Coherent Anti-stokes Raman Spectroscopy) using a combined CARS-IRS instrument with a common path 9-nanosecond pulsed, injection-seeded, 532-nm Nd:YAG laser probe pulse. The section summarizes the measurements of velocities along

the core of the vitiated air flow as well as two radial profiles. The average velocity measurement near the centerline at the closest point from the nozzle exit compares favorably with the CFD calculations using the VULCAN code. Further downstream, the measured axial velocity shows overall higher values than predicted with a trend of convergence at further distances. Larger discrepancies are shown in the radial profiles.

5.1 Introduction

Both experimental and computational fluid dynamics methods are widely used in the design and analysis of hypersonic air-breathing engine flow paths. Most CFD methods employ models that are based on statistical properties of flow turbulence. The actual statistical properties can be known only when multiple flow properties are measured simultaneously, and when the spatial scales (hundreds of microns or less) and temporal scales (hundreds of nanoseconds or less) of the turbulent fluctuations are resolved. Correlations between those properties lead to a more detailed understanding of complex flow behavior and aid in the development of multi-parameter turbulence models for computational fluid dynamics codes [2, 12].

This section of the report presents simultaneous measurements at multiple points of two orthogonal components of flow velocity using an interferometric Rayleigh scattering (IRS) technique [16]. The measurements are performed simultaneously with a combined CARS-IRS (Coherent Anti-stokes Raman Spectroscopy — Interferometric Rayleigh Scattering) instrument that uses the same 9-nanosecond pulsed, injection seeded, Nd:YAG laser beam (at 532 nm) for both techniques [13]. The experiments were conducted at NASA Langley Research Centers Direct Connect Supersonic Combustor Test Facility (DCSCTF) on an axisymmetric Mach 1.6 H_2-air combustion-heated jet flow at enthalpy levels of a Mach 5.5 hypersonic flight [20–22]. Section 4 describes in detail the measurements of flow temperature obtained simultaneously with velocities using the CARS system [36].

5.2 Description of the Instrument

Figure 45 shows a schematic of the experimental setup for IRS. The IRS instrument measures by directing and focusing polarized light from a green beam laser (wave vector k_0) using a first lens (L_1) to a measurement volume within the gas medium, providing laser illumination from one direction as shown in the figure. Laser light, elastically scattered in the measurement volume by the gas molecules, is collected from two opposite directions using a lens (L_3) for one direction and a mirror (M_r) for the other. Both collected signal beams (k_{s1} and k_{s2}), directly collected by the lens L_3 and collected and retroreflected toward the lens by the mirror M_r, are combined in a single signal beam. This collected scattered light (the signal) is then collimated by lenses L_4 and L_5, combined with a fraction of the main laser light (reference beam) using a beam combiner/mixer, and passed through a solid etalon for spectral analysis (black box). The interference fringe pattern generated at the output of the etalon (by the lens L_6) is recorded by a CCD camera at 20 Hz, the laser pulse and the measurement repetition rate. The resulting recorded image, as shown in Fig. 46, contains the scattered light spectral information in two horizontal patterns, and the laser frequency (concentric ring pattern) used as a reference frequency. The horizontal patterns are the images of the laser beams (viewed from two directions) filtered out spectrally by the etalon.

Each horizontal pattern determines an independent velocity component. In-house developed image processing software extracts spatial and spectral information for both velocity components from each interferogram image. These data are fit with theoretical Rayleigh scattering models (Gaussian functions) to determine the Doppler shift frequency of the

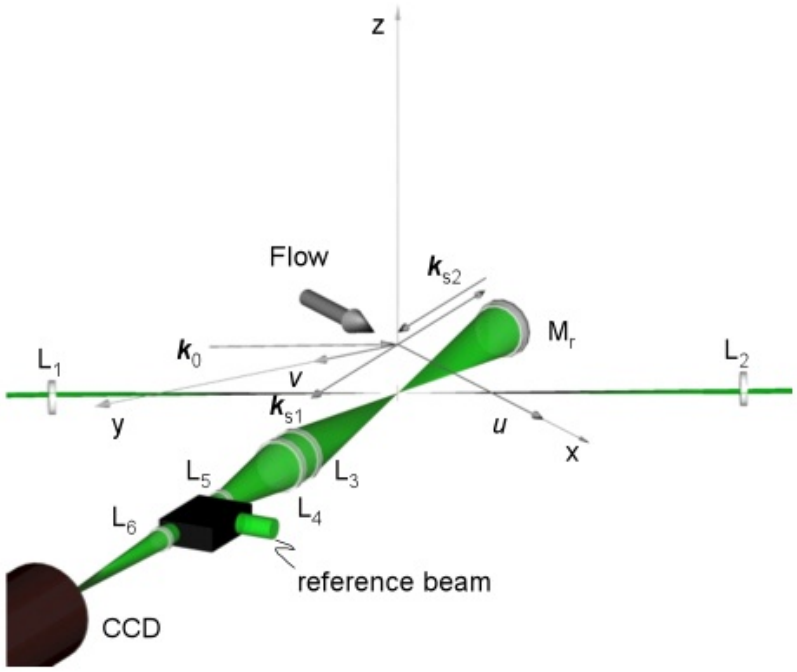

Figure 45. Measurement configuration (all vectors are in the horizontal plane).

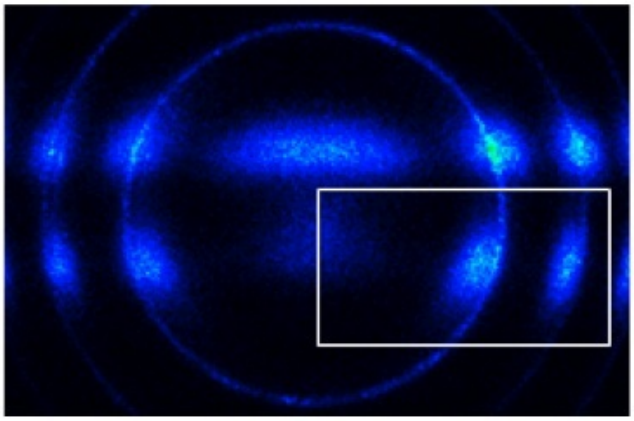

Figure 46. Single-shot interferogram containing reference laser frequency (concentric ring pattern) and Rayleigh scattered light spectral information (horizontal patterns). The interferogram is obtained in the axi-symmetric supersonic jet, with the top horizontal pattern for the radial component, and the bottom horizontal pattern for the axial component of velocity.

spectra with respect to the reference laser frequency. The magnitude of each flow velocity component is then calculated from the Doppler shift.

An example of spatially and temporally resolved IRS spectra from two closely separated measurement locations is shown in Fig. 47. The temporal resolution is about 40 ns [16], and

the spatial distance between spectra is about 0.4 mm. Figure 47(a) and Fig. 47(b), show the experimental data (black symbols), the theoretical best fit (black line), and the residual between them (blue). The fit functions are Gaussian functions (red lines) with the narrow peak (the reference frequency) being at the laser frequency. Figure 47(b) shows spectra with the reference peaks at the noise level that are predominant in the measurements presented here.

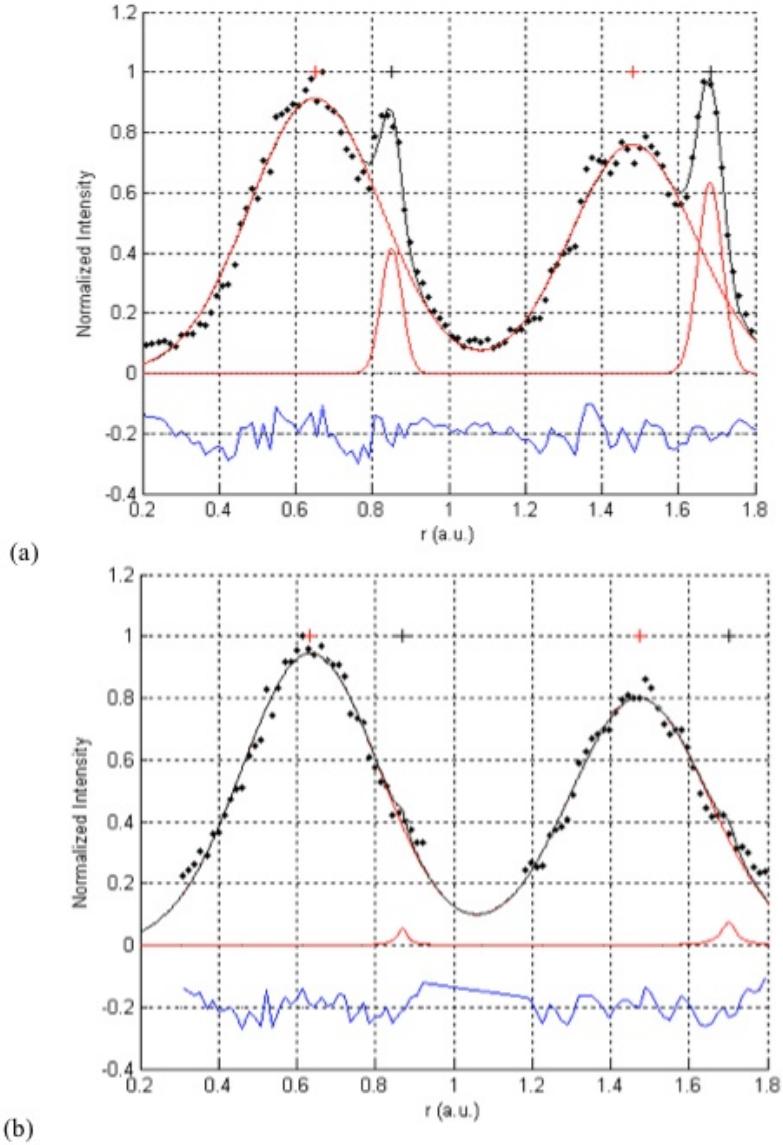

Figure 47. Single-shot IRS spectra from two spatial locations as shown in the inset of Fig. 46. (a), mixed spectra of signal and reference laser of equal amplitude, and (b), combined spectra with the reference intensity at the noise level. The plot shows the experimental data (black symbols), the theoretical best fit (black line), and the residual between them (blue). The fit functions of the signal and the reference are marked in red: the narrower peaks are at the laser reference frequency. The spatial width between spectra is about 0.4 mm.

The bisector of the angle formed by the incident laser beam and the viewing direction gives the direction of the velocity component being measured. Since the collection directions of the scattered light are anti-parallel, the two components of velocity being measured are orthogonal. An angle of 60±1 degrees (forward scattering) was used to measure the streamwise component of velocity, u, and an angle of 120±1 degrees (backward scattering) to measure the component of velocity in a perpendicular direction, ν.

The volume imaged by the IRS system contains four non-evenly spaced measurement points of about 0.2 mm^3 each in the images of the laser beams (Fig. 46). These points are distributed along about 1.6 mm of the laser beam at its focus. The inner points of this pattern are situated about 0.8 mm apart, with at the next points being about 0.4 mm further apart on each side. More detailed information about the IRS system and data analysis can be found in references 56 and 57.

5.3 Facility Description

The nozzle assembly installed in the DCSCTF consists of a water-cooled nickel flange, a water-cooled copper nozzle block, and a stainless steel cone [21]. The convergent-divergent nozzle is formed within the copper block, and its contour was designed by the method of characteristics to provide a uniform Mach 1.6 flow at the exit. A coflow nozzle is formed by the space between the copper block and the steel cone. The coflow nozzle is connected to the fuel supply (H_2) but it is not used during the experiment reported herein. The nozzle is instrumented with thermocouples and pressure taps.

In the facility, the nozzle assembly is fixed horizontally, so the laser beam delivery system and the IRS optics translate horizontally in two dimensions to probe multiple spatial locations in a horizontal plane. Two linear translation stages were used as means of translating the system up to 0.6 m in the cross flow directions, and 1 m in the streamwise direction (∼9 to 16 nozzle diameters). The translation stages have a position accuracy of 200 μm and repeatability of ±12 μm. Due to physical and equipment constraints (including constraints imposed by the CARS system) two arrangements were used to probe the flow. The upstream setup permitted measurements from 0.87 to 7 nozzle diameters downstream of the nozzle exit plane, while the downstream setup allowed measurements between 6 and 13 nozzle diameters. Overlapping test points were set at the intersection of these two regions to check reproducibility of the measurements. All measurement points were performed in a horizontal semi-plane passing through the centerline of the jet (and containing the laser beams). The jet was captured by an exhaust pipe (to minimize the fire hazard during experiments) placed axially in front of the jet for both the upstream and the downstream tests at about 24 nozzle diameters downstream of the nozzle exit. The pipe, with an inside diameter of 24.8 cm, is connected to a vacuum sphere (22 meters in diameter) and is the lowest cross-sectional area in the exhaust system. The pressure in the sphere was reduced to a few torr (mm Hg) before runs, and the typical increase in pressure during a 50 sec run was of the order of 140 torr. Other details of the experimental setup in the facility, including the jet nozzle and combustor design, can be found in references 13 and 20. Figure 48 shows an infrared image (in the range of 3 μm to 5 μm) of the jet flow during the facility run at Mach 5.5 enthalpy. The image shows the shock-free jet flow with some larger turbulent flow structures towards the downstream end of the field of view (flow from left to right). The curved objects in the field of view are the nozzle assembly on the left and silhouettes of the opto-mechanical components of the measurement system.

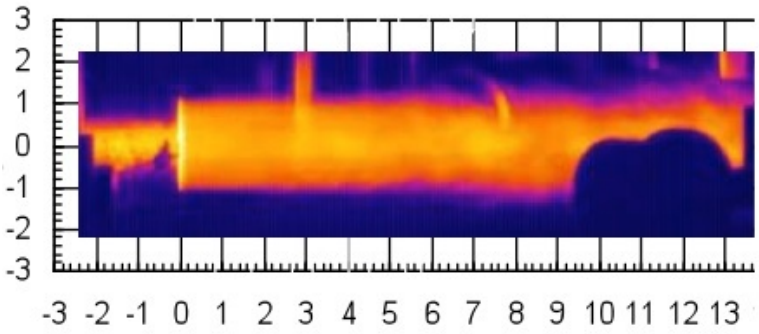

Figure 48. Infrared image of the jet during the facility run at Mach 5.5. The flow is from left to right. The curved objects in the field of view are optical components.

5.4 Velocity Distribution in the Flow Field

5.4.1 CFD simulations using the VULCAN code

As a part of this work, the jet into ambient air was simulated numerically using the VULCAN CFD code. This code solves the Navier-Stokes equations using a finite volume discretization. The inviscid fluxes were computed using the low dissipation flux split scheme of Edwards in conjunction with a 3^{rd} order MUSCL stencil and a limiter by Van Leer. Thermodynamic properties for the thermally perfect gases were computed using the curve fits of McBride et. al. The turbulence was modeled using the k-omega model of Wilcox. The computational domain extended 60 jet diameters downstream of the nozzle exit and 40 jet diameters radially from the centerline to the outer boundary. It also included the facility combustor downstream of the fuel injectors and the Mach 1.6 nozzle. Calculations were made with both coarse (124,556 points) and fine grids (494,332 points) to ensure that the solutions were grid resolved. The combustor conditions[1] were at a total pressure of 419 kPa and a total temperature of 1397 K. In the surrounding ambient air the total pressure was 1 atmosphere with a 20 m/sec velocity imposed to mimic the airflow in the test cell and to aid numerical convergence. Figure 49 shows Mach contours in the flow near the jet exit. A shear layer develops between the high velocity jet flow and the very low velocity ambient airflow. At these conditions the pressure in the jet exit is slightly higher than the ambient pressure resulting in weak waves reflecting back and forth between the shear layer and the centerline.

The flow through the exhaust pipe into the vacuum sphere generated choked flow at the entrance or somewhere in the pipe. This close proximity of the exhaust pipe to the nozzle exit affected the downstream free jet properties slightly. Two CFD calculations were performed to investigate this effect, one without the pipe and a second with the pipe. In the simulation neglecting the exhaust pipe, the jet centerline became subsonic about 11 jet diameters from the nozzle exit and continued to decelerate further downstream. With the pipe, the flow downstream of the sonic point (at about Mach 0.8) re-accelerates to a supersonic Mach number. The exhaust pipe influences the downstream subsonic flow and slightly affects the upstream core flow (about 0.5% of the main stream velocity).

[1]Initial calculations used conditions published by Cutler [21] (P_0 = 419 kPa and T_0 = 1327 K) however, these did not match the CARS temperature data [36]. A second set of calculations was then made at P_0 = 419 kPa and a total temperature of 1397 K.

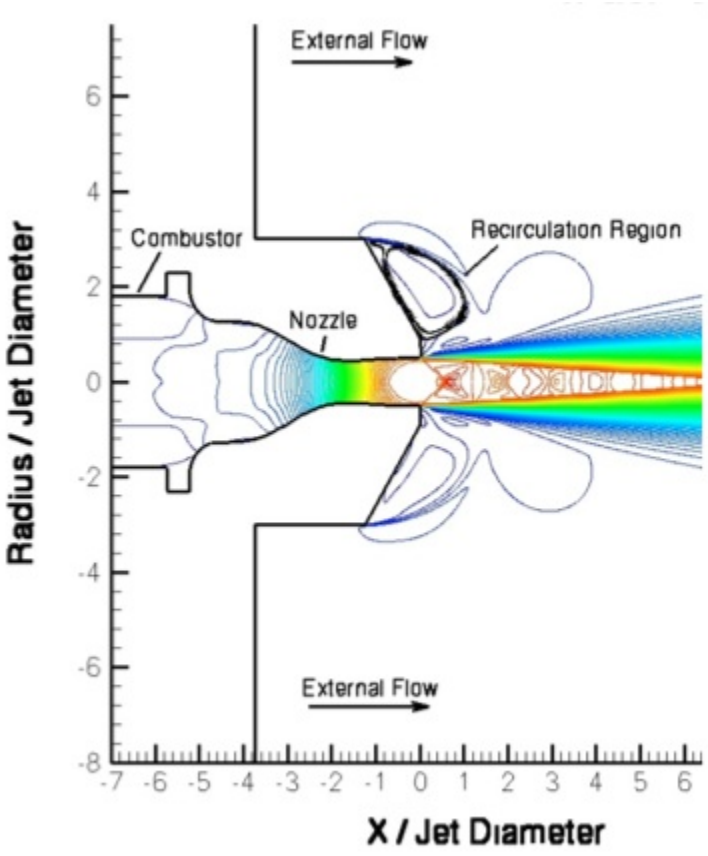

Figure 49. Mach number contours lines in the combustor, nozzle and the upstream flow. The colors in the order, red, yellow, green, and blue, show contour lines of decreasing Mach number.

5.4.2 Streamwise Velocity Profiles near the Centerline of the Jet

Figure 50 shows the average axial velocity u_{ave} ($\overline{u}$) as function of the normalized distance from the nozzle exit plane, x/d (where the nozzle exit plane is at x/d = 0 ± 0.02, and d = 6.35 cm), at y/d = 0.04 ± 0.06 near the centerline. The centerline distribution of the average radial velocity v_{ave} ($\overline{v}$) is plotted similarly in the same figure using open symbols. The data plot is divided into two parts: upstream (black symbols) and downstream (red symbols), corresponding to the two distinctive sets of measurements that were performed. Error bars of one standard deviation about the mean velocity are shown in the figure. Due to the experiment modifications from the upstream to downstream measurements (it is possible that the measurement locations are not overlapped) there is a jump in the average velocity of about 50 m/sec (one standard deviation at that location) at the intersection of these two datasets. Slightly different flow conditions in the combustor might also have a contribution to this jump [36]. A plot of the standard deviation of the measured velocity versus the normalized distance from the nozzle plane is also shown in the lower part of the figure.

The systematic errors of the instrument cannot be fully quantified (at this time) for the entire range of the instrument. The measurements in stagnant air show that the error of measuring zero velocity in the axial direction has a systematic error of about 20 m/sec. The uncertainty in the scattering angle of ±1 degree, relative to the velocity vector being

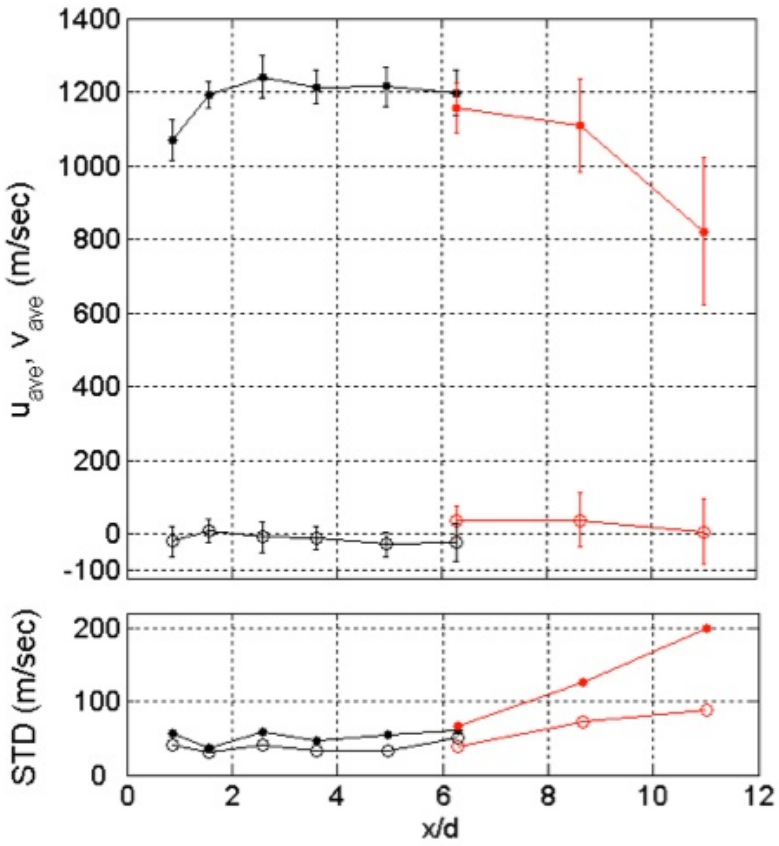

Figure 50. Near centerline average velocity u and v (top), and the standard deviation of the measured velocity (bottom) as function of the normalized distance x/d from the nozzle exit plane.

measured, contributes to a systematic error in calculating the velocity of about ±1.5% or about ±15 m/sec. Therefore, the total systematic error in the velocity measurements quantifiable at this time becomes about 25 m/sec. The instruments random error in the facility, based on the ability to determine the free spectral range of the interferogram [56,57] is found to be about 30 m/sec for the axial component and about 4.5 m/sec for the radial component of velocity. The errors associated with the change in the bias velocity as a function of velocity and gas temperature are unknown, although in Reference [14], it was determined for a similar setup that the velocity bias was no more than 30 m/sec over the range of temperatures used in this experiment. The instrument systematic error of measuring zero velocity (20 m/s) was subtracted from the dataset measured values to correct this known error.

As expected, the flow turbulence, as measured by the standard deviation in the velocity measurements, significantly increases with the distance from the nozzle exit. Increases are as much as about 7 times and 3 times the near-field velocity fluctuations of u and v, respectively.

The centerline measurement results are summarized in Table 11 as a function of the normalized distance x/d along with the average of the measured velocity, $\overline{u}$ and $\overline{v}$, the standard deviation of the measurement, σ_u and σ_v, and the number of measurements,

x/d	$\bar{u}$ (m/sec)	σ_u (m/sec)	$\bar{v}$ (m/sec)	σ_v (m/sec)	N_u	N_v
0.87	1069	57	-21	40	141	29
1.58	1192	36	8	30	82	80
2.6	1241	59	-9	40	94	95
3.6	1213	46	-11	32	81	82
4.9	1214	54	-28	33	93	89
6.3	1197	61	-23	50	77	71
6.3	1156	66	38	39	102	107
8.9	1110	125	38	73	93	92
11.0	821	200	6	89	58	64

Table 11. The axial velocity data near the centerline of the jet (at y/d = 0.04 ± 0.006 where d = 6.35 cm). Red indicates downstream data.

N_u and N_v, used to compute the velocity average from about 200 measurements per set point. The reported velocity measurements are the average from two spatially separated measurement locations about 0.4 mm apart. The effective measurement volume is thus about 0.2 × 0.2 × 0.6 mm. Each mean velocity data point presented here is obtained from one run performed at that location. On average, about 5 times more data is available at one location. All this data will be processed and reported in the near future.

The first data point in Fig. 50, the closest to the nozzle exit, compares favorably with CFD calculations [16, 22]. Further downstream the measured velocity shows overall higher values than the free jet CFD simulation, but both fall, as one would expect, in the downstream region of the jet. This is shown again in Fig. 51 for single-shot measurements. The data is obtained simultaneously from two spatial points at the specified x/d locations (red and black symbols) and from a rapid scan along the jet performed continuously between 0.87 and 4.9 nozzle diameters downstream (red and black circle symbols). For comparison, the CFD is computed on the centerline (light blue) and off axis at y/d = 0.1 (dark blue). The comparison of the measurements with the CFD data at y/d = 0.1 suggests a possible off axis measurement (in the expansion flow regions), although this cannot explain the ∼200 m/s discrepancy.

Figure 50 shows a sudden change in v between the upstream and downstream regions. An explanation is that the bisector of the angle formed by the direction of the laser beam and the receiving optics which define the direction of the measurement does not perfectly overlap the direction of the velocity vector intended to be measured, i.e., the resultant wave vector is not parallel with the velocity vector. The contribution of the v velocity component to the measured velocity u is negligibly small, but the contribution of the u component (at about 1100 m/sec) to the measured v component (less than 100 m/sec) can be significant. The induced measurement error in the v-component can be as much as 20 m/sec per degree of offset angle. This error is unavoidable when the measurement of this angle cannot be obtained with accuracy better than ±1 degree, though it can be minimized by a calibration of the instrument. For the presented data set, such laborious calibration was not possible before every run in the test facility due to a multitude of factors including the setup configuration and the time constraint. For the upstream measurements the offset

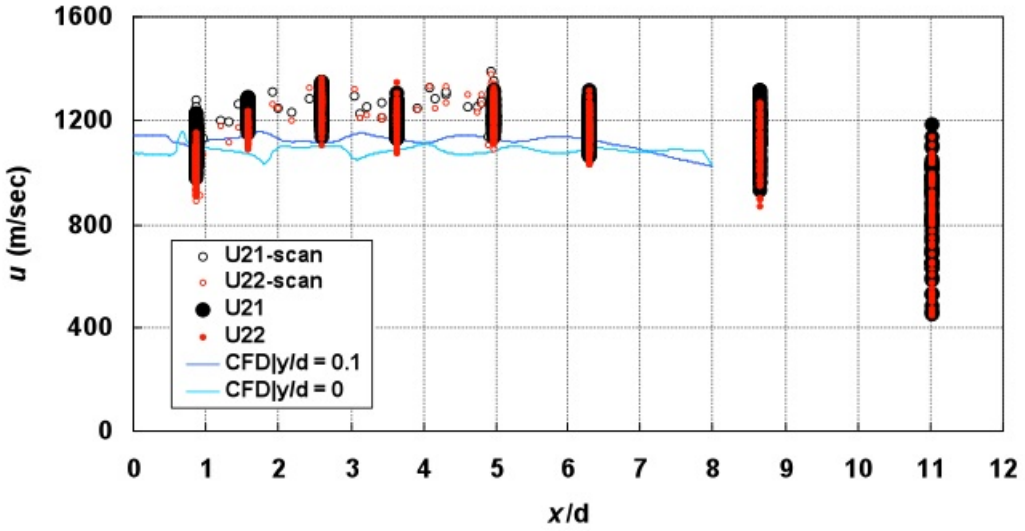

Figure 51. Single-shot measurements and CFD calculations of the axial velocity as function of the normalized distance x/d from the nozzle exit plane. CFD data computed on the centerline (turquoise) and off axis at y/d = 0.1 (blue).

angle is about +3 degrees, and is unknown for the downstream measurements.

Measurements performed at four points simultaneously are shown in Fig. 52 for the axial velocity component as a function of time. The measurements are obtained near the jet centerline at x/d = 0.87, the closest location to the nozzle exit plane (first point in Fig. 50, Fig. 51, and in Table 11). Again, for the current configuration, the four non-evenly spaced points are distributed symmetric along about 1.6 mm of the laser beam at its focus (as shown in the horizontal pattern of Fig. 46). The furthest two inner points around the center of pattern are situated about 0.8 mm apart (between u_1 and u_3), with the closest (the sides of the pattern) at about 0.4 mm apart (between u_1 and u_2 or u_3 and u_4). The red trace shows clearly a difference in the velocity measured between points at this location visible also at locations up to 2.6 nozzle diameters downstream as shown in Fig. 51.

5.4.3 Radial Profiles

Figure 53 shows two measured radial profiles and the CFD calculations of the axial (u) and radial (v) velocity at two axial locations: 2.6 and 11 nozzle diameters downstream. The red and black symbols represent single shot data from rapid scans of the flow in the radial direction. These data are obtained simultaneously from measurements at two spatially separated measurement locations about 0.4 mm apart. The data marked in dark blue with error bars were obtained from averaging multiple single-shot measurements. Similarly, the data without error bars are obtained by averaging the measurements from two spatial locations. It is clear that for the profile at x/d = 2.6 (Fig. 53(a)) the axial velocity does not reach zero at or around one nozzle diameter outside jet, as predicted in the CFD solution (light blue line). (Note in Figure 49 that the CFD solution has a recirculation region attached to the outer shroud that slows the flow at this location.) In the downstream portion of the jet, a velocity profile [58] approximating a Gaussian distribution, should be reached as shown by the CFD calculation, but an approximate top hat profile is shown by the instantaneous measured data instead (Fig. 53(b)). This may indicate that the jet in the CFD solution is

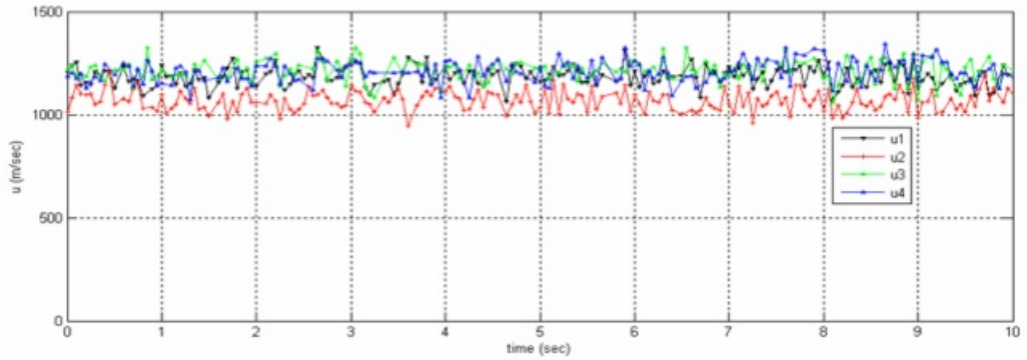

Figure 52. Simultaneous measurement of the axial velocity at four spatial locations near the jet centerline of a Mach 1.6/Mach 5.5 enthalpy jet: The measurements are obtained near the jet exit at x/d = 0.87.

diffusing faster than what is seen in the data. Outside the shear layer at x/d = 2.6, the radial velocity component (v) is three times higher than the predicted one. However, the 20 m/s downstream velocity was assumed as a boundary condition in the CFD calculation and is not a true prediction of downstream properties. Also at these axial locations a difference between calculated and experimental maximum velocity u of about 200 m/sec exists in the jet.

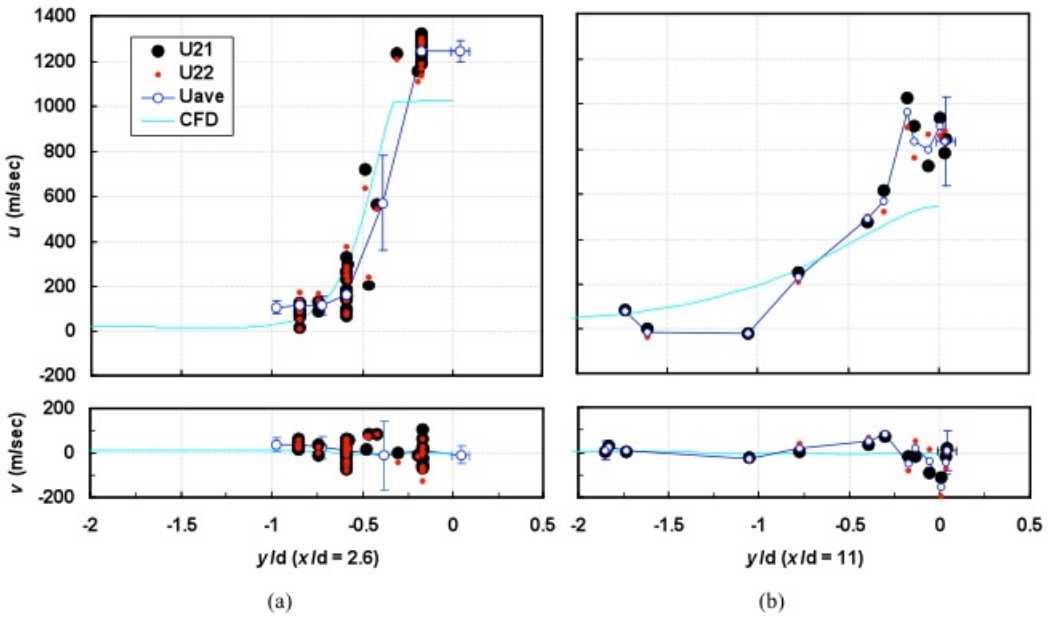

Figure 53. Radial profiles of velocity at two axial locations in the flow. (a), velocity profiles obtained at x/d = 2.6 in the upstream, and (b), at x/d = 11 in the downstream. The blue curves indicate the CFD solutions of an ideal free jet at Mach 1.6 (Mach 5.5 enthalpy).

These discrepancies cannot be explained entirely at this time and no conclusions should

be drawn, though careful analysis was performed on both the Rayleigh spectra processing and the CFD modeling. A variety of factors can lead to such discrepancies: First, not every property was measured so some assumptions were made in setting CFD boundary conditions. For example, the current CFD solutions were made with an assumed inflow turbulence level. Previous work has shown [22] that the diffusion rate of the jet is sensitive to turbulence levels at the nozzle exit. Lower turbulence levels lead to a longer core flow while higher turbulence levels lead to more rapid diffusion and Gaussian-like profiles. Further processing of the data may reveal lower actual turbulence levels than what was assumed for the CFD calculations. Similarly, the nozzle exit and the local near-field of the jet (expected to be slightly lower than atmospheric) pressures were not measured so that the exact jet pressure ratio was not known. This pressure ratio affects the expansion/compression wave structure in the jet. It is also possible that the low pressure at the suction pipe entrance has the effect of accelerating the jet significantly near the exhaust pipe. Therefore the velocity u must be higher and in regions of subsonic flow the acceleration will reduce the jet diameter (by conservation of mass) as shown by the measurements including at the edge of the boundary; A simple back of the envelope calculation employing Eulers equation suggests that this increase is very small (∼5 m/sec) and can not explain the large discrepancy in the core (∼200 m/sec) versus the small discrepancy at the edge (∼100 m/sec). Second, unknown measurement errors while moving the probe volume, such as a variable reference intensity that could offset velocity with a variable quantity (unlikely); and Third, the most of concern, the unknown influence of Hydrogen combustion products and the Raman vibrational excitation of species (from CARS) on the Rayleigh spectra and its distribution of velocities.

5.4.4 Two-Point, and Axial-Radial Velocity Correlations

Figure 54 demonstrates spatial correlations of velocities measured simultaneously at two closely separated spatial points. The distance between points used to measure u_1 and u_2 (or v_1 and v_2) is 0.4 mm. The markers in red indicate upstream data at x/d = 0.87, and the markers in black, the downstream data at x/d = 11.02. Both measurements of u and v show correlation, i.e., the data are scattered along a line with the slope of approximately 45 degrees. This indicates that a large fraction of the turbulence scale is resolved at least down to about 0.4 mm or about 6/1000 of a nozzle diameter for this type of flow.

The correlations between u'= u - $\overline{u}$ and v' = v - $\overline{v}$ velocities, where u' and v' are the velocity components measured simultaneously, and $\overline{u}$ and $\overline{v}$ are the corresponding mean velocities, are shown in Fig. 55. The black and red markers in Fig. 55(a) show the scatter in the data near the centerline at x/d = 2.6, and in the downstream at x/d = 11, respectively. In Fig. 55(b), the graph shows the velocity data obtained in the mixing layer at (x, y)/d = (2.6, -0.4). The velocities have a relatively low correlation near the jet axis both in the upstream ($\overline{u'}^2$) = 2214 m^2/sec^2, ($\overline{v'}^2$) = 958 m^2/sec^2, ($\overline{u'v'}$) = -136 m^2/sec^2) and in the downstream flow (($\overline{u'}^2$) = 34335 m^2/sec^2, ($\overline{v'}^2$) = 6108 m^2/sec^2, ($\overline{u'v'}$) = -571 m^2/sec^2), as is expected based on the axisymmetry of the flowfield. In the mixing layer the velocities are correlated (($\overline{u'}^2$) = 43754 m^2/sec^2, ($\overline{v'}^2$) = 12650 m^2/sec^2, ($\overline{u'v'}$) = 10359 m^2/sec^2) as expected in a turbulent shear layer; note that in this data set v is positive radially inward and thus the sign of $\overline{u'v'}^2$ is consistent with expectations for a turbulent shear layer. Furthermore, turbulent energy and other statistical parameters necessary for turbulent model development can be extracted from this dataset. For example, the square root of the turbulent kinetic energy $\sqrt{\frac{1}{2}(\overline{u'}^2 + \overline{v'}^2 + \overline{u'v'})}$, where v' is approximately w' for axisymmetric flow, is measured to be 3.7% in the upstream at x/d = 2.6, about 18.5% in the downstream at x/d =11, and 32% in the mixing layer at (x, y)/d = (2.6, -0.4).

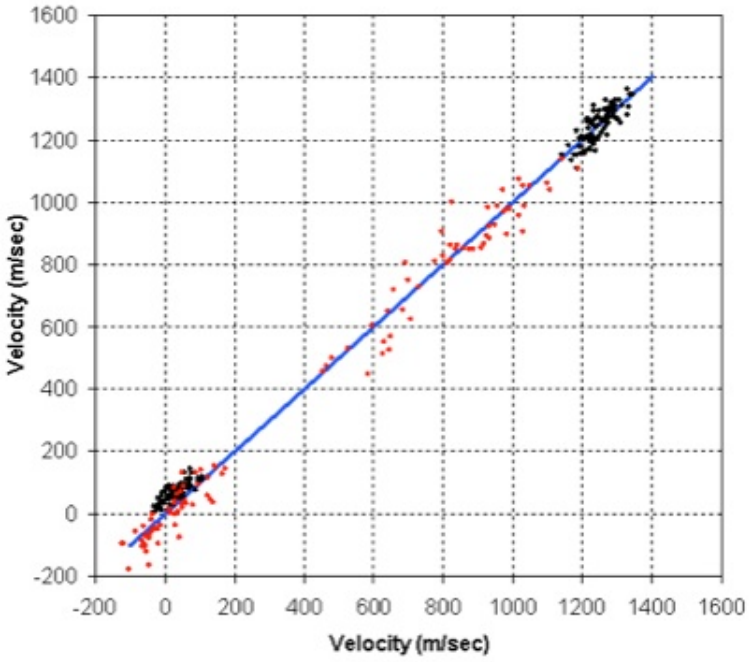

Figure 54. Two-point correlations of velocities. The distance between points is 0.4 mm. Black and Red markers indicate upstream and the downstream data at x/d = 0.87 and x/d = 11, respectively.

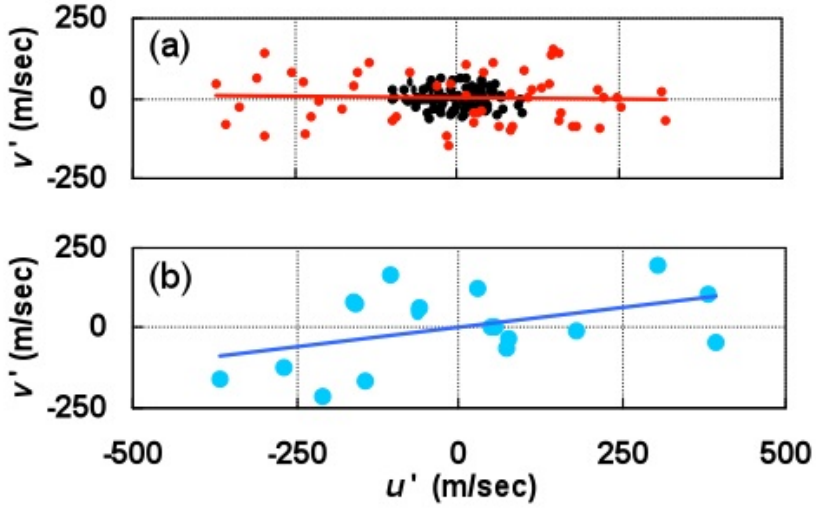

Figure 55. Correlation of velocities in the jet flow. (a), near the centerline at (x, y)/d = (2.6, 0.04) in the upstream (black), and at (x, y)/d = (11, 0.04) in the downstream. (b), velocity correlations in the mixing layer at (x, y)/d = (2.6, -0.4).

5.5 Conclusions

Measurements of two-components of flow velocity have been obtained at multiple points using a single-shot interferometric Rayleigh scattering (IRS) technique for the first time in

a large-scale combustion flow. The measurements are performed on a Mach 1.6, Mach 5.5 sensible enthalpy, H_2-air combustion heated jet at NASA Langley Research Center. The measurements are simultaneous with CARS using a combined CARS-IRS instrument that uses the same 9-nanosecond pulsed, injection seeded, Nd:YAG laser beam (at 532 nm) as the probe laser.

The data presented here summarizes measurements of the radial and streamwise velocity components near the centerline of the jet and at two radial profiles of streamwise velocity for the mixing case. The first data point of the test matrix, the closest to the nozzle exit, compares favorably with the CFD calculations using the VULCAN code. Further downstream the measured velocity shows overall higher values than the CFD values with a trend of convergence further downstream. Radial velocities are small in the mean, relative to the fluctuations, while discrepancies between the mean radial velocity and the CFD values are greater than expected. A variety of factors can cause such discrepancies such as the assumptions made in setting the CFD boundary conditions, unknown measurement errors while moving the probe volume, noisy Rayleigh spectra and the difficulty of fitting such noisy spectra. Of the most concern, is the unknown influence of Hydrogen combustion products and the Raman vibrational excitation of species (from CARS) on the Rayleigh spectra and its distribution of velocities.

The instrument precision and its systematic errors in the facility were estimated for the axial component to be about 30 m/sec, and 25 m/sec, respectively. For the radial component the instrument precision is better than 5 m/sec except that errors in alignment of the measurement coordinate system with the jet coordinate system can lead to larger systematic errors in v. The contribution of the u-component (at about 1100 m/sec) to the measured v-component (typically less than 100 m/sec) for a small angular misalignment can be as much as 20 m/sec per degree. The systematic error in velocity u is negligibly small in such a case.

Finally, the instrument resolved the turbulent time and length scales of the jet flow, as shown in the comparison of turbulent properties and computations, proving it to be a valuable tool in combustion diagnostics and in supporting CFD modeling. Plausible measurements of the turbulent kinetic energy, $\overline{u'v'}$, the main component of the turbulent Reynolds stress, were presented.

6 Development and Implementation of Ethylene-Air Reduced Reaction Models in High-Speed Flows

Development of reduced chemical kinetic models with a lower number of scalar variables can lead to a significant reduction in the computational effort required in simulating high-speed reacting flows. The automated reduction procedure developed here is based on the application of the quasi-steady-state (QSS) approximation for intermediate chemical species and on the elimination of selected fast elementary reactions [59]. The procedure is sufficiently general that any complex starting reaction mechanism (detailed or skeletal) can be reduced with minimal human intervention. A key feature of the reduction procedure is the decoupling of the QSS species appearing in the QSS algebraic relations, enabling the explicit solution of the QSS species concentrations which are needed for the evaluation of the elementary reaction rates. The automated procedure is used to obtain explicit robust reduced reaction models for ethylene-air. The predictions obtained with reduced models are compared with experimental data on ignition delay, flame propagation velocity, and non-premixed flame extinction condition, over a wide range of equivalence ratios, initial temperatures, pressures, and flow strain rates. The reduced reaction models developed are also implemented in simulation of supersonic reacting shear layers for a range of inflow conditions. Detailed analyses show that the models can adequately explain basic combustion characteristics associated

with the location of detached reaction fronts and the corresponding induction lengths or induction times.

6.1 Introduction

Since the 1980's considerable effort has been devoted to developing well-validated computational methods for hypersonic applications, including high-speed reacting flows with finite-rate kinetics [60]. Considering the prohibitive computational effort involved in employing detailed reaction mechanisms with 1000's of elementary reactions, methods of reaction model reduction and their validation/verification are addressed in this work. In particular, systematically reduced reaction models are developed based on characteristic time scales of supersonic reacting flow fields. The reduced reaction model validations are performed based on several canonical reacting flow geometries, eg. zero-dimensional ignition phenomena, laminar flame propagation, extinction of strained non-premixed counterflow flames with strong molecular mixing effects, and supersonic shear flows with detached or lifted reaction layers.

The typical hydrocarbon fuels considered for hypersonic applications, eg. JP-7, JP-8, etc., consist of nearly 300 different hydrocarbon components or species. For modeling purposes in hypersonic applications, the overall reaction process has been represented by cracked fuel mixtures with specified kinetic rates [61, 62]. This effort has received renewed interest with steady improvements in high-performance computational capabilities and also interest in application to gas-turbine engines, pulse detonation engines, etc. [63]. In hypersonic applications, however, the previous work has shown that when the fuel is used to dissipate typical thermal loads, ensuing cracking of the fuel molecules leads to lower order hydrocarbon molecules (fuels consisting of one- to three-carbon atoms — C_1-C_3 fuels, such as CH_4, C_2H_4, C_2H_2, C_3H_8). Therefore, the focus of the work described in this section is on the development and validation of reduced reaction models for such lower-order hydrocarbon fuel mixtures.

The detailed reaction mechanisms for C_1-C_3 cracked fuels still consist of 70-80 species in close to 500 elementary reactions with somewhat well established rate constants [64–70]. In the near term, even these relatively short mechanisms cannot be implemented in multi-dimensional turbulent reacting flow simulations because of the computational effort involved. This is particularly true for flows with large Damköhler numbers. Fortunately, by considering the characteristic flow and chemical time scales in the flow field, these detailed reaction models can be simplified or "reduced" to a manageable level, and this is the main focus of the present investigation. It should be emphasized that the reduction procedure is based on the implementation of quasi steady-state (QSS) approximation and retains all the species and reactions of the starting elementary mechanism (identified here as the skeletal mechanism), but species associated with QSS are solved explicitly via algebraic relationships. Moreover, knowing that the rate constants of detailed reaction models are continuously being updated as new experimental data become available, a comprehensive automatic reduction procedure has been developed and implemented in canonical reacting flows mentioned above.

6.2 Mechanism Reduction Methods

The concept of deriving simplified chemical kinetic models based on the quasi steady-state (QSS) approximation for selected intermediate chemical species dates back to the early 1900's. Some examples are the homogenous reaction models of Bodenstien [71] and the heterogeneous reaction models of Langmuir [72]. While these early investigations were motivated by the lack of chemical kinetic data, the recent efforts on mechanism reduction were driven by the computational difficulty associated with the implementation of rather

large detailed chemical kinetic models, especially in large-scale simulations of unsteady multi-dimensional combustion systems.

An early investigation aimed at reducing the computational effort employed what is known as the rate-controlled partial equilibrium (or rate-controlled constrained equilibrium, RCCE) approach [73]. A major weakness of the RCCE approach lies in the identification of the "kinetic constraints," which is still an active research topic [74]. The systematic application of the QSS approach of Peters [75] eliminated the arbitrariness of imposing "kinetic constraints," and established the field of reduced reaction modeling. As part of this work, an automated reduction approach based QSS approximation was developed and implemented, as discussed below.

6.2.1 Quasi Steady-State and Partial-Equilibrium Approximations

A brief outline of procedure used to develop reduced reaction models is presented here. Consider the conservation equations for species i, written in the form

$$\mathcal{L}[Y_i] = W_i\hat{\omega}_i \equiv W_i(\hat{\omega}_i^+ - \hat{\omega}_i^-), \quad i = 1, .., N, \tag{1}$$

where $\mathcal{L}$ is some operator that describes the transient, convective, and diffusive effects, while the RHS describes the net mass production rate. As indicated in Eq. 1, the net mass production rate can also be written in terms of species creation ($\hat{\omega}_i^+$) and species destruction terms ($\hat{\omega}_i^-$). For fast chemical reactions or large Damköhler numbers (defined as the ratio of characteristic flow time to chemical reaction time), the flame structure can be described by the equilibrium chemistry. In other words, the transport flux terms are much smaller than the species creation ($\hat{\omega}_i^+$) and destruction ($\hat{\omega}_i^-$) fluxes. The resulting balance between the creation and destruction terms eliminates the need to integrate partial differential equations governing species with fast chemistry, with significant simplification of the solution process. This simplification can be translated into a "reduced reaction model," which still retains all the information of fast chemical reactions in the form of algebraic relations, with a reduced set of scalar variables to be integrated.

A majority of early investigations using reduced reaction models based on the QSS approximation were analytical in nature [75, 79–82], hence the computational efficiency was not a primary factor in developing these reduced models. For example, highly-stiff coupled algebraic relations arising from the QSS approximation were solved iteratively, i.e. with "inner" iterations [83], or the coupled QSS algebraic relations were truncated to yield "explicit" expressions for the species in QSS albeit within a narrow range of validity or with diminished accuracy. The need for introducing "inner" iterations or "truncations" clearly increases with the complexity of the detailed reaction model, e.g. when dealing with models describing large hydrocarbon fuel oxidation.

6.2.2 Automatic Reduction Method

The formal computer-based reduction methods, e.g. computational singular perturbation (CSP) method [84], facilitated the development of reduced reaction models from large detailed models, based on the quasi steady-state/partial-equilibrium approximation in homogeneous ignition system. Variants of the CSP approach has been used by others [85, 86] to obtain reduced reaction models either based on ignition or perfectly-stirred reactor simulations. However, these mathematical/computational approaches still require the solution of highly-stiff algebraic relations using computationally expensive "inner" iterations, which the RCCE approach intended to avoid via potential element method.

After careful consideration of the above literature, a new automated mechanism reduction procedure was developed using the MATLAB environment by Zambon and Chelliah [77]. A key distinction of the present approach from previous work is the ability to relax certain

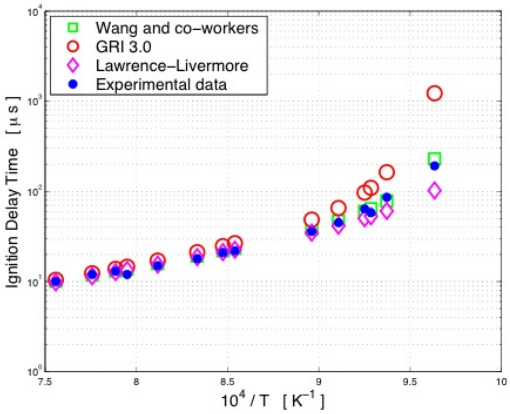

Figure 56. Comparison of ignition delay data for a H_2:O_2:Ar mixture of 2:1:3.76 at p=2.5 atm (Bhaskaran et al. [87]), with detailed kinetic models (Zambon and Chelliah [77].

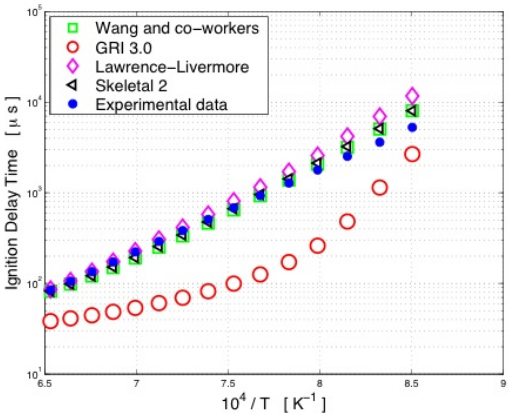

Figure 57. Comparison of ignition delay data for C_2H_4:O_2:Ar mixture of 0.25:0.75:99.0 at p= 12 atm (Baker and Skinner [88]), with detailed kinetic models (Zambon and Chelliah [77]).

QSS relationships to obtain "explicit" expressions for the QSS species, i.e. completely avoid costly "inner" iterations, as discussed above. The level of relaxation can be based on a predetermined tolerance satisfying the QSS approximation. A computational cost analysis was presented in [77] highlighting the differences between the "explicit" reduced reaction model (ERRM) approach and the "inner" (or implicit) iteration approaches. Another important feature of the present ERRM approach is the ability to analyse solutions of the ignition process in a spatially uniform well-stirred reactor as well as solutions of premixed or non-premixed flames with transport effects. It has been shown that the reduced reaction models derived based on ignition solution can be different from those derived using a steady-state flame structure solution, especially when considering the absence of transport effects in the homogeneous ignition problem [77]. In this regard, the present MATLAB-based ERRM approach is more general compared to the CSP approach [84]. Other features include the ability to always obtain a unique reduced reaction model by elimination of the fast reactions in a logical manner and the ability to tailor the output from the MATLAB program to adapt to various computational codes [77].

6.3 Results and Discussion

6.3.1 Detailed Reaction Models

For C_1-C_3 hydrocarbons, several detailed or elementary kinetic models have been reported in the literature, including Wang and co-workers [64], Lawrence Livermore National Laboratory [65], UC San Diego [66], GRI-3.0 [67], and others [68–70]. As part this work, the applicability of these detailed models in predicting 119 sets of ignition delay data sets for H_2, CH_4, C_2H_4 and C_3H_8 were investigated. A sample comparison of two data sets are shown in Figs 56 and 57, for H_2 and C_2H_4. While the detailed models by Wang and co-workers [64] and Lawrence Livermore National Laboratory [65] agree closely with most of the experimental ignition delay data shown, it should be pointed out that these models for C_1-C_3 hydrocarbon fuels are continuously being updated and considerable uncertainties still exist. In this regard, computational mechanism reduction tools developed must be able to quickly adopt any changes introduced to the detailed reaction models.

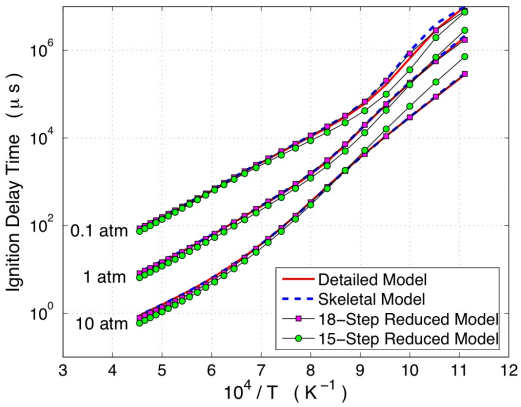

Figure 58. Comparison of ignition delay data for a $C_2H_4/O_2/Ar$ mixture using detailed, skeletal and reduced reaction models (Zambon and Chelliah [77]).

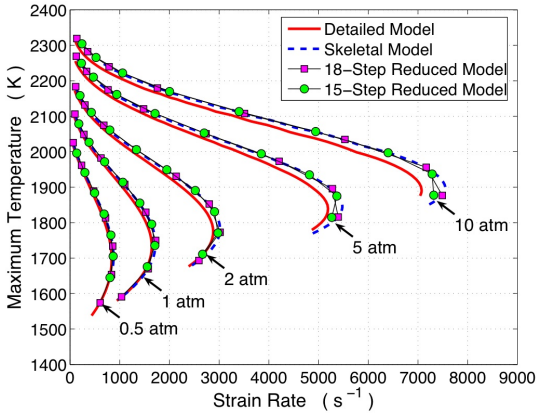

Figure 59. Comparison of extinction prediction of $C_2H_4/O_2/Ar$ mixture using detailed, skeletal and reduced reaction models (Zambon and Chelliah [77].)

6.3.2 Skeletal Reaction Models

The detailed kinetic models described above, consisting of roughly 70 species in 500 reactions for C_2-C_3 hydrocarbons (eg. ethylene, propane), can be further stripped down to **skeletal** reaction models which contain only the essential rate controlling reactions. This reduction involves evaluation of combined effects of (i) the local and global sensitivity of each reaction (both forward and backward), (ii) heat release by each reaction, and (iii) reaction pathway or reaction fluxes. For example, using the detailed model of Wang and co-workers [64], a 31 species in 128 reaction skeletal model was recently developed for ethylene oxidation by Zambon and Chelliah [77]. A comparison of the ignition delay predictions and non-premixed counterflow flame extinction prediction of ethylene/air with this skeletal model and the detailed model are shown in Figs. 58 and 59.

While such "skeletal" models can be implemented in simple multidimensional simulations (eg. two-dimensional shear layers), as mentioned in the introduction, their implementation in multi-dimensional, turbulent, transient reacting flow simulations is not practical. This difficulty can be related to the large number of scalar variables involved and the stiffness associated with the "fast" chemical reactions. The only viable option is to use systematically developed **reduced reaction models**, where fast reversible chemical reactions are set to partial equilibrium or a set of species is identified in QSS based on groups of fast chemical reactions.

6.3.3 Reduced Reaction Models

Starting with the "skeletal" reaction model developed above, two sets of reduced reaction models have been obtained based on (a) ignition delay results (eg. 18-step model ethylene/air) and (b) flame propagation results (eg. 15-step model ethylene/air), and are listed in Table 12. Irrespective of the basis for their reduction, these two reduced reaction models were then used in predictions of ignition delay and flame extinction condition, as shown in Figs. 58 and 59, as well as flame propagation predictions shown in Fig. 60. As seen from Figs. 58 - 60, the 18-step reduced reaction model works well in all three cases, i.e. ignition, propagation, and extinction for a wide range of pressures and equivalence ratios, while the 15-step model shows deviation from the ignition delay results at low temperatures.

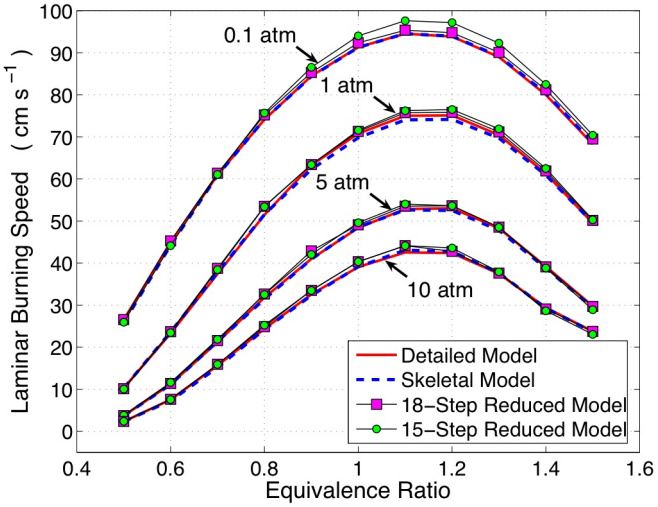

Figure 60. Comparison of flame propagation velocity prediction of C_2H_4/air mixtures using detailed, skeletal and reduced reaction models (Zambon and Chelliah [77].)

6.3.4 Extension to Large Hydrocarbon Fuels

In an early investigation on jet fuel chemistry, the concept of fast thermal decomposition of jet fuels was implemented by Lee et al. [62]. Certainly, the task of developing a decomposition model for jet fuel is rather difficult because jet fuels typically contain over 300 hydrocarbon components. Of these components, roughly 75% by volume are paraffinic components and 25% by volume are aromatic components. In order to distinguish the reaction mechanism for the two groups, by assuming that the paraffinic components can be represented by $C_{13}H_{28}$ and the aromatic compounds by $C_{10}H_8$, Lee et al. [62] have proposed the following global decomposition reaction for the paraffinic component

$$2C_{13}H_{28} \rightarrow 13C_2H_4 + 2H_2, \qquad (I)$$

and the following global oxidation reaction for the aromatic component

$$C_{10}H_8 + 5O_2 \rightarrow 10CO + 4H_2. \qquad (II)$$

In their study [62], the subsequent oxidation of ethylene (C_2H_4), carbon monoxide (CO) and hydrogen (H_2) was modelled by two methods (a) a detailed mechanism involving 51 species in 242 reactions and (b) an *ad hoc* three-step global mechanism. The frequency factors of reaction rates (I) and (II) were adjusted to get agreement with measured ignition delay times reported by Freeman and Lefebvre [89].

On the other hand, recent surrogate fuel development efforts have introduced a much wider range of pure hydrocarbon components to represent chemical as well as physical properties of jet fuels. These mixtures range from simple two-component mixtures (*n*-Decane (70%) and *n*-Propylbenzene (30%)) to complex twelve-component mixtures (*n*-Decane (15%), *n*-Dodecane (20%), *n*-Tetradecane (15%), *n*-Hexadecane (10%), *m*-Xylene (5%), Butylbenzene (5%), Tetramethylbenzene (5%), etc.) [90]. Clearly, considerable ambiguity exists about the ideal surrogate fuel mixture to be used and careful experimental validation is essential for development of reliable kinetic models for jet fuels.

Step Number	Global Reaction	18-Step	15-Step
1	$C_2H_4 + H = CH_3 + CH_2$	√	√
2	$aC_3H_5 + H_2 = C_3H_6 + H$	√	
3	$C_2H_4 + CH_3 = C_3H_6 + H$	√	√
4	$C_2H_3 + H_2 = CH_3 + CH_2$	√	
5	$C_2H_6 = 2\ \ CH_3$	√	√
6	$CH_4 = CH_3 + H$	√	√
7	$C_2H_2 + H_2 = 2\ \ CH_2$	√	√
8	$CH_3 = CH_2 + H$	√	√
9	$CH_2O + H_2 = CH_2 + H_2O$	√	√
10	$CH_2CO = CH_2 + CO$	√	
11	$CO + 2\ H_2 + O = CH_2 + 2\ \ H + O_2$	√	√
12	$CO_2 = CO + O$	√	√
13	$H_2O_2 = 2\ \ OH$	√	√
14	$HO_2 = O_2 + H$	√	√
15	$H_2 = 2\ \ H$	√	√
16	$H_2O + H = O_2 + OH$	√	√
17	$H + OH = H_2 + O$	√	√
18	$O + OH = O_2 + H$	√	√

Table 12. The representation of 18-step and 15-step reduced reaction models developed for ethylene/air using automated reduction approach (Zambon and Chelliah [77]).

Besides the fast-thermal decomposition in combustion environment, the individual hydrocarbon components of jet fuels are likely to undergo endothermic pyrolysis during active cooling of hypersonic vehicles. The outcome of the latter process is known to depend on the pyrolysis temperature and the heat flux [91]. The net result is that finite-rate chemical kinetic models are needed only for the lower-order hydrocarbon fuels, eg. ethylene, acetylene, etc. In order to explore the viability of extending the chemical kinetic models developed for C_1-C_2 species to JP-10 (tricyclodecane, $C_{10}H_{16}$), a global fast-decomposition reaction of the form

$$C_{10}H_{16} \rightarrow aC_2H_4 + bC_2H_2 + cH_2,$$

is assumed here, with the selection of appropriate stoichiometric coefficients a, b, and c. Figure 61 shows the predicted ignition delay time using the ethylene detailed and skeletal models with the above fast JP-10 decomposition reaction. The experimental data of Colket and Spadaccini [92] for JP-10 ignition are shown for comparison. These predictions have clearly indicated that the ignition delay is independent of the rate constants selected for the decomposition reaction, but is a strong function of the stoichiometric reaction coefficients selected. Considering the excellent agreement between skeletal and reduced reaction models for ethylene shown in Fig. 58, a similar level of agreement between JP10 ignition delay data with the proposed reduced reaction models is clearly attainable.

6.3.5 Extension to Multi-Dimensional Simulations

In addition to the development and validation of reduced reaction models based on canonical reacting flow configurations (i.e. ignition, propagation, and extinction), the reduced reaction models have been implemented in simulation of two-dimensional, high-speed, shear flows. The objective here is to verify the applicability of the mechanism reduction methodology developed for high-speed reacting flows, including the generation of analytical Jacobian matrices. In this effort, NASA SPARK code [60] was implemented for two cases, with

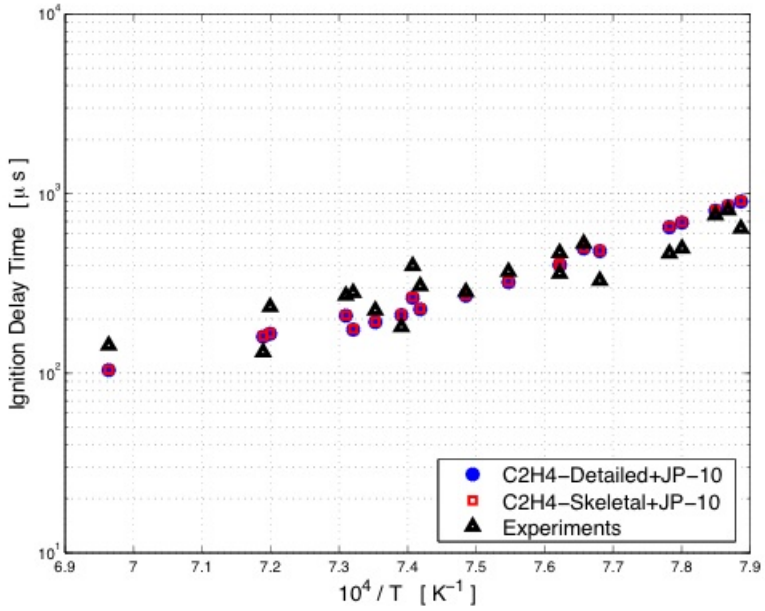

Figure 61. Comparison of ignition delay *vs.* $1/T$, for a JP10/air mixture. Experiments are from Colket and Spadaccini [92] and predictions are assuming fast-thermal decomposition coupled with ethylene detailed and skeletal models (Zambon and Chelliah [77]).

highly refined grid resolution and a small computational domain. In the first case, two supersonic streams of non-premixed hydrogen and air was considered with a finite thickness splitter plate. The grid resolution of the order of 20 μm was used to resolve molecular mixing and finite-rate chemistry of hydrogen-air shear flow. Inflow conditions (Mach number and temperatures) were selected such that the chemical reactions indeed occur in a detached region without flashback or blow-off, as shown in Fig. 62. Since the flow field is dominated by unsteady Kelvin-Helmholtz type instabilities, for the reduced reaction model verification purposes, quantitative comparisons between the detailed model and the reduced reaction model are performed based on averaged results as shown in Fig. 63. The excellent agreement seen in Fig. 63 indicates that even for such low-resident time supersonic reacting flows, well-validated reduced reaction models can capture the mixing and finite-rate chemistry as described by the detailed model.

For the ethylene-air supersonic shear flow case, a slightly simple two-dimensional configuration is considered here, i.e. a smooth hyperbolic-tangent inflow velocity profile is imposed. Unlike the finite-thickness splitter plate case with large scale vortical structures, here the resulting mixing and reaction layer is stable, as shown in Fig. 64, and requires considerably less computational effort. A comparison of the predicted species profiles across a fixed x-plane (at steady state, typically after about 5000 iterations) is shown in Fig. 65, indicating an excellent agreement between the skeletal model and 18-step reduced reaction model for ethylene-air.

6.4 Conclusions

Starting from any detailed or skeletal reaction model, a method of automatic generation of reduced reaction models was developed using the symbolic programming features of MATLAB. While the procedure developed was based on the concept of systematic application of

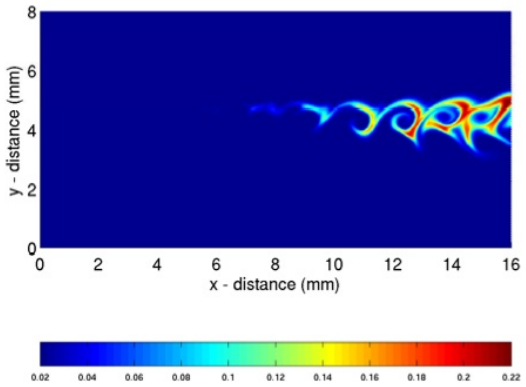

Figure 62. Predicted H_2O contours of hydrogen-air shear layer, with $M_{air} = 1.5$, $M_{H_2} = 1.1$, $T_{air} = 2000$K, $T_{H_2} = 900$, $p = 1$ atm, and $d_{splitter} = 0.5$mm.

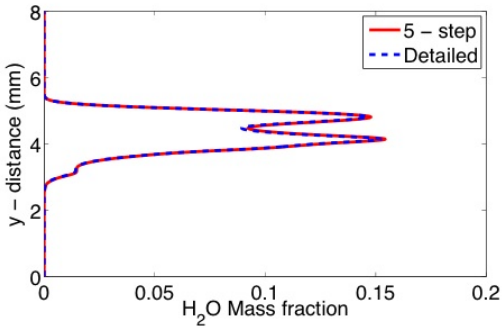

Figure 63. Comparison of ensemble-averaged H_2O profiles across the shear layer ($x = 15$mm), using a detailed and a 5-step reduced model for hydrogen-air.

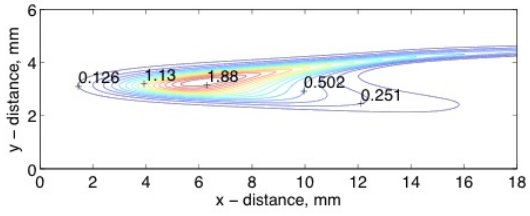

Figure 64. Predicted instantaneous HO_2 contours of ethylene-air shear layer with hyperbolic-tangent inflow profile for velocity, with $M_{air} = 1.8$, $M_{C_2H_4} = 1.4$, $T_{air} = 2200$K, $T_{C_2H_4} = 2000$K, and $p = 1$ atm.

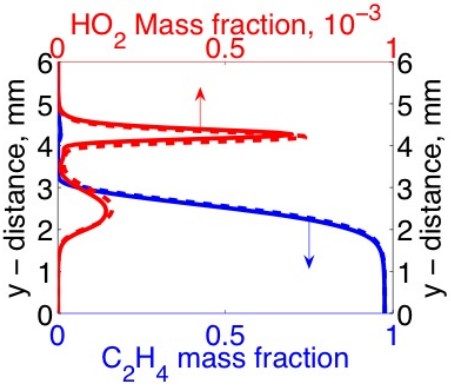

Figure 65. Comparison of instantaneous profiles of ethylene and HO_2 across the shear layer ($x = 15$mm), using the skeletal (dashed) and 18-step reduced model (solid) for ethylene-air.

the quasi steady-state (QSS) approximation, an important feature of the approach developed was the ability to explore different levels of reduction based on a set of user-defined parameters or error tolerances to tailor the reduced reaction model to the specific application of interest. In addition, the reduced reaction models developed can be based on results from a zero-dimensional ignition configuration, as well as flame propagation and extinction configurations where the transport effects can become relevant.

Considering ethylene as the primary C_2 fuel of interest for hypersonic applications, a skeletal reaction mechanism for ethylene consisting of 31 species in 128 reversible elementary reactions was first developed. The automated procedure was then applied to develop several reduced reaction models, eg. a 5-step model for hydrogen-air, a 13-step model for methane-air, and two models for ethylene-air based on ignition data (18-step) and on flame propagation data (15-step). These models were validated based on ignition delay times, flame propagation velocity, and extinction condition data, for a range of temperatures, pressures, and equivalence ratios.

Reduced reaction models developed for hydrogen-air and ethylene-air mixtures were then implemented in simulation of a supersonic reacting shear layer configuration. Because of the simplicity of this two-dimensional configuration, this system has facilitated the verification of reduced reaction models developed in multi-dimensional setting by making extensive comparisons with the detailed/skeletal reaction model solutions. For the hydrogen-air case with a finite-thickness splitter plate, the averaged flow variables obtained with the reduced (5-step model) and detailed models indicate excellent agreement across the shear layer at various downstream locations, as well as the predicted flame stand-off distances. A similar level of agreement was observed between the skeletal model and the 18-step ethylene-air reduced model where the splitter plate at the inflow was replaced with a hyperbolic-tangent inflow profile. The application of reduced reaction models to multi-dimensional, turbulent reacting flows is being pursued with other collaborators.

7 Simulation of the Supersonic Combusting Jet Experiments Involving Hydrogen/Air and Ethylene/Air Reaction

A comprehensive turbulence model that calculates the turbulent Prandtl and Schmidt numbers as part of the solution, accounts for compressibility effects, and addresses turbulence/chemistry interaction is presented [93]. The model predictitons are compared to two experiments, the large scale supersonic combusting jet experiment of section 2 involving mixing, hydrogen combustion, and ethylene combustion, and a three-dimensional ethylene mixing experiment. Fair to good agreement is indicated in the cases where data is available. Chemical mechanisms are found to have an influence on auto-ignition for hydrogen combustion cases, and ignition location and flame size for hydrogen/ethylene combustion cases using reduced mechanisms.

7.1 Introduction

Simulation of turbulent combustion in scramjet engines requires highly sophisticated models in order to address the complex flow physics involved. Typical turbulence models only consider velocity fluctuations, but earlier work [94] has shown that specification of the turbulent Prandtl number, Prt, and turbulent Schmidt number, Sct, have a profound influence on the simulation. In high speed reacting flows, concentrations and temperature fluctuations are as important as velocity fluctuations, and must be included in the model. In order to assess the impact of these fluctuations, equations for the variance of enthalpy and its dissipation

rate, as well as the variance of concentrations and its dissipation rate are required. These equations are derived from the exact compressible Navier-Stokes equations and modeled term by term in the same way the $k-\zeta$ turbulence model was developed [95]. Compressibility is another important aspect of supersonic mixing in that it limits the spreading rate of injected fuel. The model of Ref. [96] is used, which has been previously validated with three sets of supersonic mixing experiments [97–99]. Turbulence/Chemistry interaction is also an important part of supersonic combustion. Traditionally, assumed or evolution Probability Density Functions (PDFs) are used to address this. It was shown in Ref. 100 that calculations using assumed and evolution PDFs produced comparable mean flows, but the assumed PDF was unable to predict higher order correlations, such as those involving chemical source terms, with any accuracy. Also, evolution PDFs require a large amount of storage and computational time, since they require Monte Carlo simulation. Due to these restrictions, the terms involving chemical production rates were modeled as in Ref. 101. The chemical kinetic model also plays an important role in supersonic combustion. Differences among chemical models can affect the ignition location or the temperature at which a simulation will auto-ignite. Four distinct chemical models are considered here, two for vitiated air/hydrogen combustion [102, 103], and two reduced chemical models for vitiated air/ethylene combustion [77, 104]. Predictions of this model, which includes all of the above aspects, are compared with the experiments of the Office of the Secretary of Defenses Test Media Effects Program (OSD-TME) [10]. The purpose of this program is to examine the effects of the differences between ground tests and flight tests of supersonic combustors. In particular, the use of vitiated air in place of regular air, and its effects on flame holding and other aspects related to chemical kinetics [1, 20]. Also, a particular experiment of Lin et al. [105] involving normal injection of ethylene into a cold Mach 2 flow is considered.

7.2 Formulation of the Problem

7.2.1 Governing Equations

The variable Pr_t and Sc_t formulations employed in this work are based on equations for the variance of enthalpy and its dissipation rate and variance of concentrations and its dissipation rate. The variance of enthalpy, h''^2 , and its dissipation rate, ϵ_k , provide an expression for α_t , the turbulent diffusivity in the form

$$\alpha_t = 0.5(C_h k \tau_h + \nu_t/\beta_h) \tag{1}$$

where

$$\tau_h = h''^2/\epsilon_h, \quad \epsilon_h = \alpha\overline{\left(\frac{\partial h''}{\partial x_i}\right)^2} \tag{2}$$

ν_t is the turbulent eddy viscosity,

$$\nu_t = C_\mu k^2/\nu\zeta, \quad C_\mu = 0.09. \tag{3}$$

C_μ is a model constant, α is the laminar diffusivity, and ν is the molecular kinematic viscosity. The parameter β_h is chosen here as 0.5. The turbulent Prandtl number, Pr_t is given by

$$Pr_t = \nu_t/\alpha_t. \tag{4}$$

Similarly, the variance of concentrations, σ_Y ,

$$\sigma_Y = \sum \widetilde{Y_m''^2}, \tag{5}$$

where Y_m'' is the fluctuation of the mass fraction of species m, and its dissipation rate, ϵ_Y ,

$$\epsilon_Y = \sum \overline{D \left(\frac{\partial Y_m''}{\partial x_i} \right)^2} \tag{6}$$

yield the turbulent diffusion coefficient, D_t, as

$$D_t = 0.5(C_Y k \ \tau_Y + \nu_t/\beta_Y) \tag{7}$$

where

$$\tau_Y = \sigma_Y/\epsilon_Y. \tag{8}$$

C_Y and β_Y are model constants, and D is the molecular binary diffusion coefficient. The turbulent Schmidt number, Sc_t, is defined as

$$Sc_t = \nu_t/D_t. \tag{9}$$

Equations 1 and 7 are coded in such a way that, for constant Pr_t and/or Sc_tcalculations, β_h and/or β_Y are chosen to match the desired number(s). Both C_Y and C_h were obtained from Launder [106].

The equation for σ_Y, the variance of concentrations, contains the term

$$\sum \overline{Y_m'' \dot{\omega}_m},$$

where $\dot{\omega}_m$ is the production rate of species m. Similarly, the equation that governs the enthalpy variance contains the term

$$\sum \overline{Y_m'' \dot{\omega}_m},$$

where $\Delta h_{f,m}$ is the heat of formation of species m. Traditionally, the above terms are evaluated by using assumed or evolution PDFs, or ignored completely. Because such terms are important, a modeling approach was implemented in Ref. 101. Thus,

$$2 \sum \overline{Y_m'' \dot{\omega}_m} = C_{Y,8} \sum \sqrt{\widetilde{Y_m''}} \ \overline{\dot{\omega}_m} \tag{10}$$

and

$$\sum \overline{h_m'' \dot{\omega}_m \Delta h_{f,m}} = C_{h,12} \sqrt{\widetilde{h''}} \sum \overline{\dot{\omega}_m \Delta H_{f,m}} \tag{11}$$

where $C_{Y,8}$ and $C_{h,12}$ are model constants, and $\overline{\dot{\omega}_m}$ is the value of $\dot{\omega}_m$ using mean temperature and mass fractions. Because evolution PDF methods are computationally intensive requiring extensive computer time and excessive storage, the above modeling results in a highly efficient algorithm.

The compressibility correction results from the dilatational dissipation term, $\frac{4}{3}\nu\overline{\rho(u_i'', j)^2}$, and a pressure work term, $\overline{u_i''} \frac{\partial P}{\partial x_i}$, that appear in the k equation. The variety of models given in Ref. 107 assume the dilatational dissipation term to be proportional to $M_t \sim k/a^2$, the turbulent Mach number. However, because the speed of sound is finite for gases, the $k - \zeta$ model models the term as [95]

$$\frac{4}{3}\nu\overline{\rho(u_{i,j}'')^2} = C_1 \overline{\rho} k/\tau_\rho, \quad C_1 = 0.6 \tag{12}$$

where

$$\frac{1}{\tau_\rho} = \frac{1}{\overline{\rho}} \left[k \left(\frac{\partial \overline{\rho}}{\partial x_i}^2 \right) \right]^{\frac{1}{2}} \tag{13}$$

As may be seen from Ref. 107, compressibility effects severely restrict the spreading rate of free shear layers at high Mach numbers and thus have a profound influence on mixing and combustion. The pressure work term is modeled as

$$\overline{u_i''} \frac{\partial P}{\partial x_i} = \frac{\nu_i}{C_k \overline{\rho}} \frac{\partial \overline{\rho}}{\partial x_i} \frac{\partial P}{\partial x_i} \tag{14}$$

7.2.2 Numerical Procedure

A modification of REACTMB [108], a code that has been under development at North Carolina State University for the last several years, is employed in this investigation. It is a general purpose parallel Navier-Stokes solver for multi-component multi-phase reactive flows at all speeds. It employs a second order essentially non-oscillatory and/or total variation diminishing (ENO/TVD) upwind method based on the Low Diffusion Flux Splitting Scheme of Edwards [109] to discretize the inviscid fluxes while central differences are employed for the viscous and diffusion terms. Plane relaxation is employed. The code is parallelized using domain decomposition and message passing (MPI) strategies.

7.2.3 Chemical Kinetics Models

Vitiated Air/H_2

Two completely distinct H_2 / Air mechanisms are considered. The first is the seven species / seven reaction model developed by Jachimowski. [102] In this mechanism, the seven species considered are: H_2, O_2, OH, H_2O, H, and O together with the inert species N_2. All reaction rates in this model are functions of temperature. The second is the nine species / nineteen reaction mechanism developed by Connaire [103] et al. This model considers all of the above species as well as HO_2 and H_2O_2. Moreover, the reaction rates are both pressure and temperature dependent. This model was developed for combustion over a temperature range of 298 - 2700 K, a pressure range of 0.01 - 87 atmospheres and equivalence ratios from 0.2 - 6.

Vitiated Air/H_2/C_2H_4

Two sets of reduced kinetic models are employed for C_2H_4/Air combustion. The first is that of Gokulakrishnan et al. [104] In this model, a one-step reaction, $C_2H_4 + O_2$ resulting in C_2H_2O and H_2 is employed. This is followed by a detailed $C_2H_2O/H_2/O_2$ kinetic model that includes 14 species and 44 reactions. The second is that of Zambon and Chelliah [77], which employs the quasi-steady-state (QSS) approximation. The equations that result from QSS are, in general, nonlinear. The distinguishing feature of this approach is that the solution of the resulting algebraic equation is explicit, thus increasing efficiency. The resulting reduced model consists of 18 elementary reactions involving 22 species.

7.3 Results and Discussion

A Schematic of the OSD-TME experiment is shown in Figure 2. The center jet in this axisymmetric device consists of vitiated air at Mach 1.6. The test enthalpies ranged from that of Mach 5 to Mach 7 flight. The fuel is injected at low subsonic speeds through a coflow nozzle angled 30 toward the main jet. The pressure at the nozzle exits is atmospheric and total temperature in the coflow nozzle is near ambient. Experiments were conducted without coflow fuel, as well as with hydrogen alone, ethylene alone, and a hydrogen ethylene

Run Number	Enthalpy	P0 (Pa)	T0 (K)	Phi H2	Phi C2H4
M27-M75	Mach 5.5	402500	1218	-	-
M79-M95	Mach 5.5	429400	1376	-	-
H57	Mach 5.5	414400	1319	1	-
E40a	Mach 6	421300	1523	0.7	-
E40b	Mach 6	421300	1523	0.7	0.53

Table 13. OSD—Test Media Effects Experiment Conditions.

mix. The runs chosen for computations are listed in Table 13. The cases without coflow fuel will be referred to as the mixing cases. The block layout of the grid used for all of the OSD-TME experiments is shown in Figure 66. The measurements in this experiment were taking using a dual pump CARS-IRS system for simultaneous measurements of temperature, species concentrations, and two velocity components [14]. The error associated with these experimental measurements is 50-100 K for the temperatures and 30-100 m/s for the velocities. The computational grid for the OSD-TME cases employs 74 blocks and contains 236,480 cells. The refined grid employs 122 blocks and contains 377,024 cells.

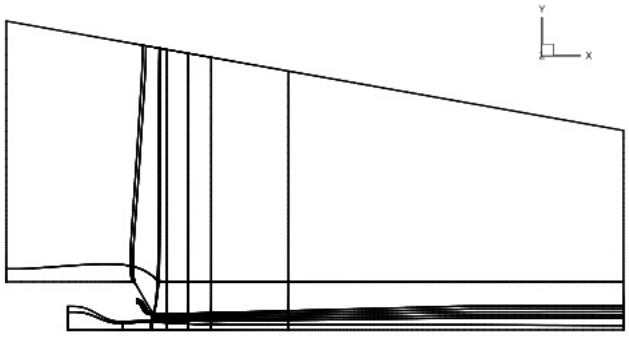

Figure 66. Block Layout for OSD-TME Computations.

A schematic of the ethylene injection experiment is shown in Figure 67. The injector, which is normal to the main flow, is circular and has a diameter of 0.1875 in. The Mach 2 air stream has a stagnation temperature and pressure of 300 K and 241317 Pa respectively. The ethylene injection nozzle has a stagnation temperature of 315 K and a stagnation pressure of 127553 Pa. The main flow boundary layer thickness at the exit of the injector was about 0.24 in. The block layout of this three dimensional case is shown in Figure 68. Ethylene mixture fraction is measured at three streamwise planes using a Raman scattering technique.16 The computational grid for this case employs 248 blocks and contains 3,768,320 cells.

7.3.1 Vitiated Air / Air

There are two sets of data for the mixing cases of the OSD-TME experiments, radial temperature profiles at various streamwise locations, and axial velocity along the centerline of the nozzle. As can be seen in Table 13, the average stagnation temperature for the near field measurements, which were taken in runs M27-M75, is significantly lower than the average for the far field measurements, which were taken in runs M79-M95. The same trend

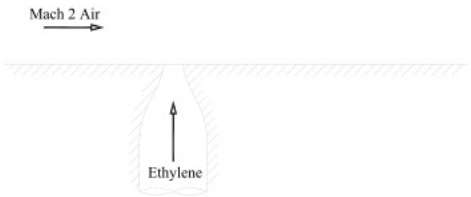

Figure 67. Schematic of Ethylene Injection Case.

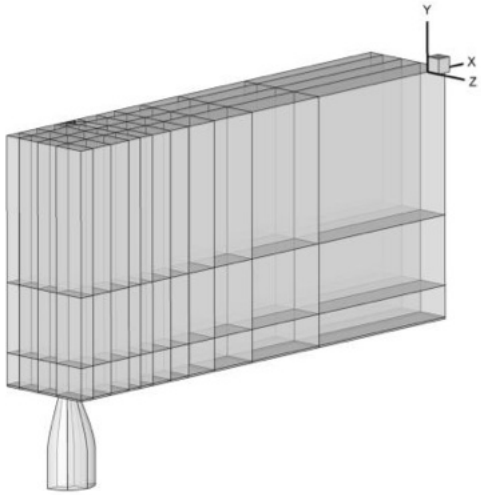

Figure 68. Block Layout for Ethylene Injection Case.

is observed in the stagnation pressure. Simulations were carried out using both of these averages and are presented together with the experimental data.

Figure 69 shows measured and computed temperature profiles for eight different streamwise locations. For the most part, there is good agreement. Note that there is some asymmetry in the experimental data. This is most likely due to a shifted reference point in the measurements, not an asymmetry in the jet itself. The experimental data is presented here unaltered. Also note the appearance of two different experimental profiles at the 40 mm station. This has been attributed to the fact that half of the measurements came from the higher average temperature runs. Figure 70 shows the measured and computed axial velocities along the centerline of the jet. The measured velocities are significantly higher than either of the computed profiles. This cause of this difference is unknown. Given the measured temperatures along the centerline, these velocities correspond to approximately Mach 1.8-1.9 flow. The nozzle is designed for Mach 1.6 operation, which both of the simulations predict. Finally, the computed turbulent Schmidt number contour is shown in Figure 71. Note the variation from the specified floor value of 0.2 to 1.0 across the mixing region of the jet.

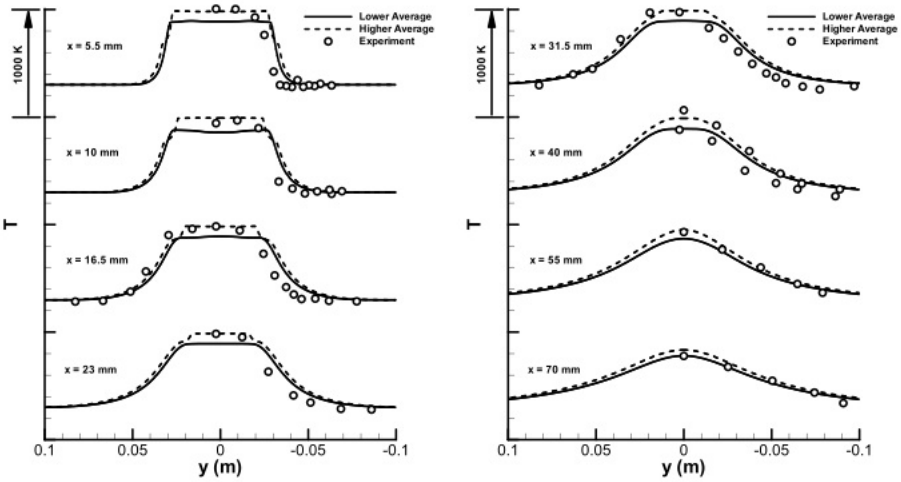

Figure 69. Radial Temperature Profiles for OSD-TME Mixing Runs.

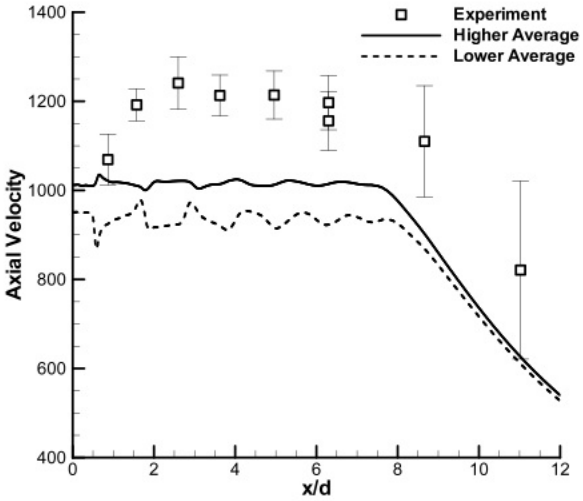

Figure 70. Axial Velocity along Centerline for OSD-TME Mixing Runs.

7.3.2 Vitiated Air / Air / H_2

While there is no experimental data for run H57 of the OSD-TME experiment, an infrared image is included for qualitative comparison. This image can be seen in Figure 72. The hydrogen is injected at atmospheric pressure and temperature with a mass flow rate corresponding to an equivalence ratio of 1.0. The purpose of these computational runs is to compare the two chemical models. Figure 73 shows the computed H_2O mole fractions for each of the chemical models, with Jachimowski on the top half and Connaire on the bottom half. Note that while the solutions are similar, the Connaire model is much less likely to auto-ignite. In this case, it was restarted from an ignited Jachimowski run, at which point it sustained the combustion and produced similar results to those of the Jachimwoski mechanism. Figures 74 and 75 show contours of turbulent Schmidt number and turbulent

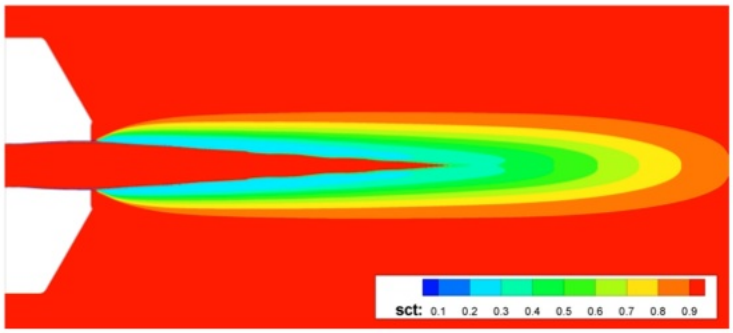

Figure 71. Computed Turbulent Schmidt Number Contours for OSD-TME Mixing Runs.

Prandtl number respectively.

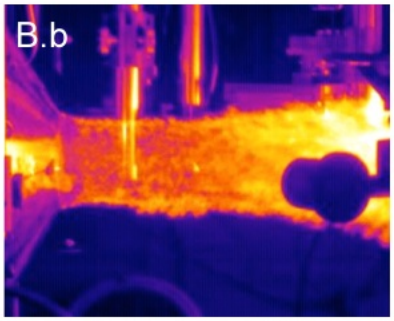

Figure 72. Infrared Image of Run H57.

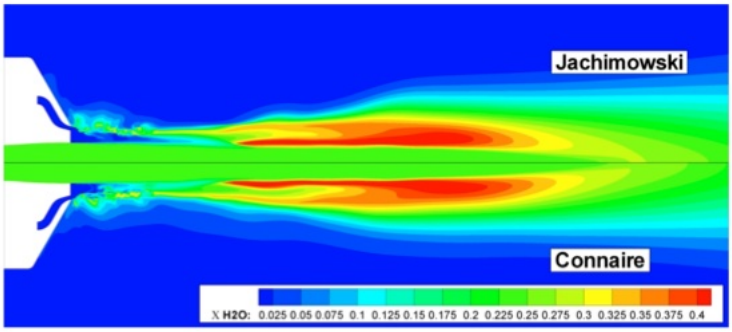

Figure 73. Computed H_2O Mole Fraction Contours for OSD-TME Run H57.

An additional run was performed using the Jachimowski mechanism on a refined grid, which doubled the number of cells in the streamwise direction. The ignition location and the overall solution remained unchanged.

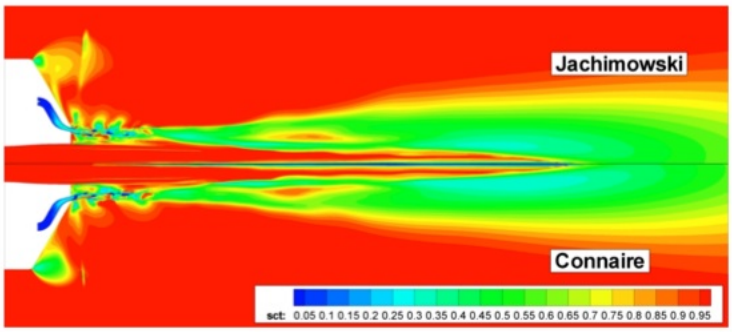

Figure 74. Computed Turbulent Schmidt Number Contours for OSD-TME Run H57.

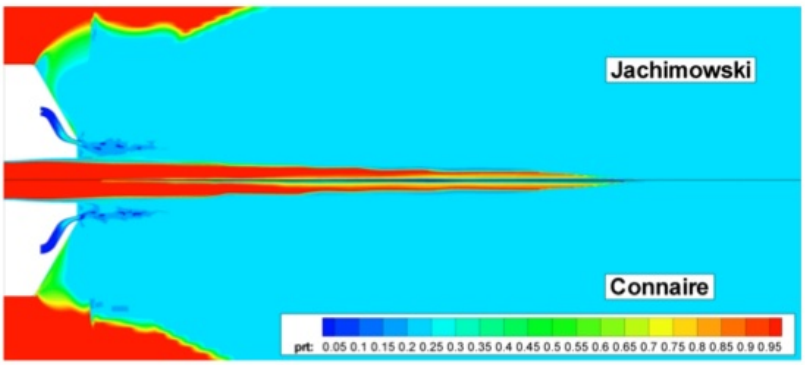

Figure 75. Computed Turbulent Prandtl Number Contours for OSD-TME Run H57.

7.3.3 Vitiated Air / Air / C_2H_4

The first case involving ethylene is the normal injection mixing experiment. Contours of air density on the symmetry plane are shown in Figure 76. This figure is included to show the structure of the flow, and to indicate the locations of the measurement planes. These planes are located at 5, 10, and 25.3 diameters down stream of the jet. Figure 77 shows the contours of ethylene mixture fraction on these three planes, measured quantities on the left and computed quantities on the right. Mixture fraction is defined by the following formula.

$$Z = (sY_f - Y_0 + Y_{0,0})/(sY_{f,0} + Y_{0,0}) \ , \tag{15}$$

where

$$s = (X_0 M_0)/(X_f M_f) \ \ at\ stoichometric. \tag{16}$$

The subscript o denotes oxidizer and f denotes fuel. In this case, these correspond to oxygen and ethylene. $Y_{f,o}$ represents the mass fraction of fuel in the fuel stream and $Y_{o,o}$ represents the mass fraction of oxidizer in the oxidizer stream. There is fair agreement between computation and experiment here. The first station predicts a lower concentration of fuel in the center of the jet, while the third station shows a higher concentration than experiment. The black line on the plots represents the stoichometric line. Finally the computed turbulent Schmidt number contours are shown in Figure 78.

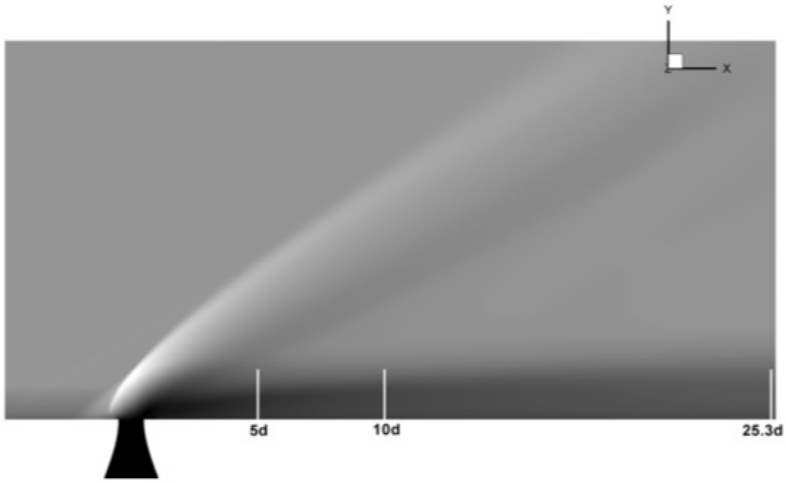

Figure 76. Computed Symmetry Plane Air Density Contours for Ethylene Injection Experiment.

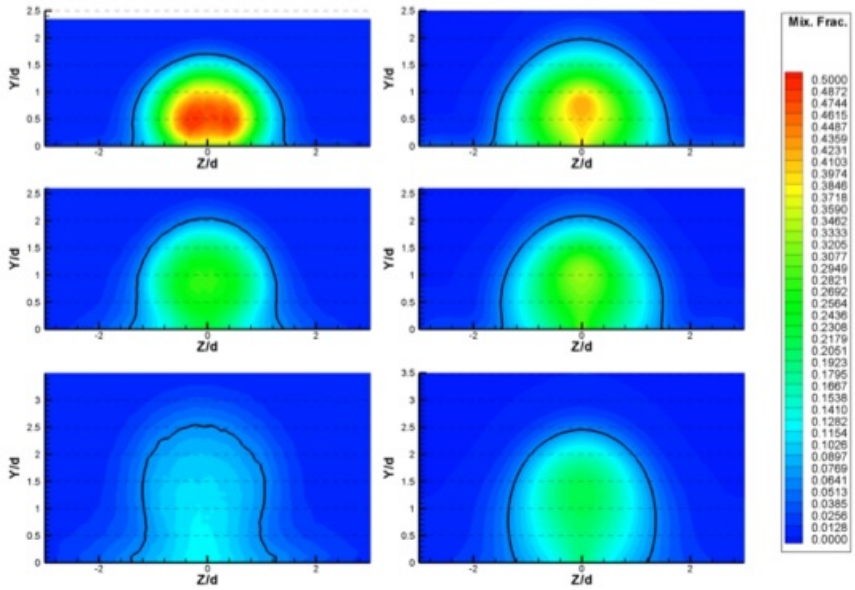

Figure 77. Measured (left) and Computed (right) Mixture Fraction Contours for Ethylene Injection Experiment.

The second case involving ethylene is run E40 of the OSD-TME experiments. This run is split into two phases, E40a and E40b. During the first phase, the coflow contains only hydrogen, with a target equivalence ratio of 0.5. During the second phase, which is initiated after steady combustion is achieved in the first phase, the coflow fuel contains both hydrogen and ethylene each with a target equivalence ratio of 0.5. The actual equivalence ratios for this particular run can be seen in Table 13. The target enthalpy is that of Mach 6 flow. A visible image of each phase is shown in Figure 79. This case was used as a comparison of the

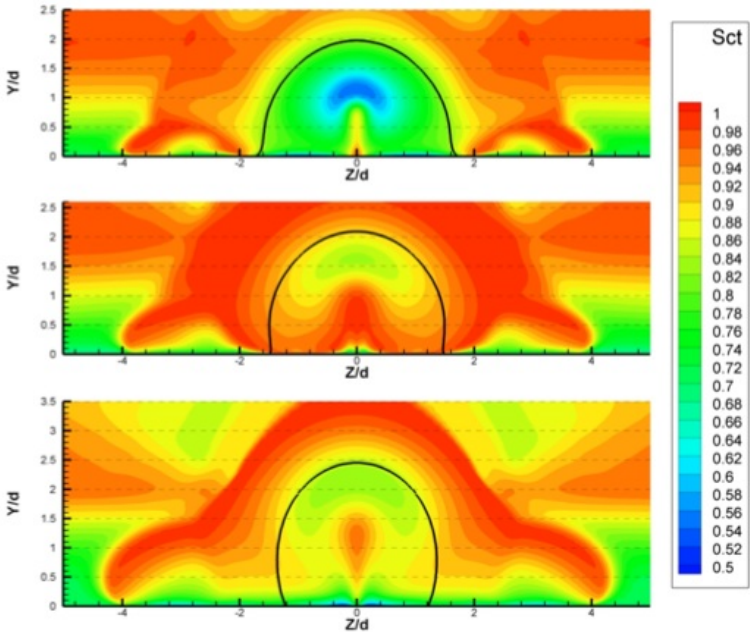

Figure 78. Computed Turbulent Schmidt Number Contours for Ethylene Injection Experiment.

two reduced ethylene mechanism described above, the 15 species model of Gakulakrishnan et al. and the 22 species model of Zambon and Chelliah. Figure 80 shows the H_2O contours for run E40a, where only hydrogen is present in the coflow fuel. The 15 species model is on top and the 22 species model is on the bottom. The 22 species model predicts a much earlier ignition and an overall smaller flame. The same trend is observed for run 40b, which is shown in Figure 81. The structure is essentially the same, but for the 22 species model, the ignition location moves slightly downstream when the ethylene is introduced. Referring back to visible images in Figure 79, this slight movement is to be expected.

7.4 Conclusions

A detailed turbulence model is presented that calculates the turbulent Prandtl and Schmidt numbers as part of the solution and models the turbulence/chemistry interaction. The model is self contained. Thus, all it requires is the specification of initial and boundary conditions.

Two sets of experiments are examined in this study. The first is an axisymmetric annular jet under a variety of conditions: a case with no coflow, a case with hydrogen fuel, and a case with a mixture of hydrogen and ethylene fuel. The second is a three dimensional case where ethylene is allowed to mix with cold air. Fair to good agreement is indicated in all cases, but some cases were only compared qualitatively in the absence of experimental data.

The role of chemical kinetic mechanism was determined to have an impact on auto-ignition for the hydrogen only cases, and a signification impact on ignition location and flame size for hydrogen/ethylene mixtures. It is believed that the current model can serve as a basis for scramjet designs. However, further comparison with detailed experiments is needed to further fine tune it.

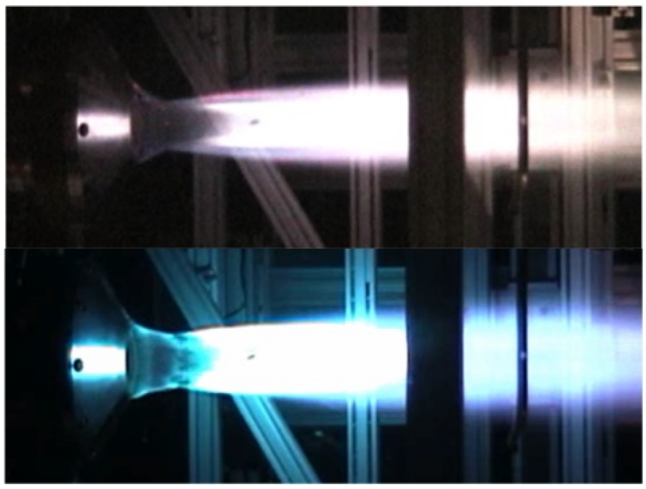

Figure 79. Visible Images of OSD-TME Experiment, Runs E40a (top) and E40b (bottom).

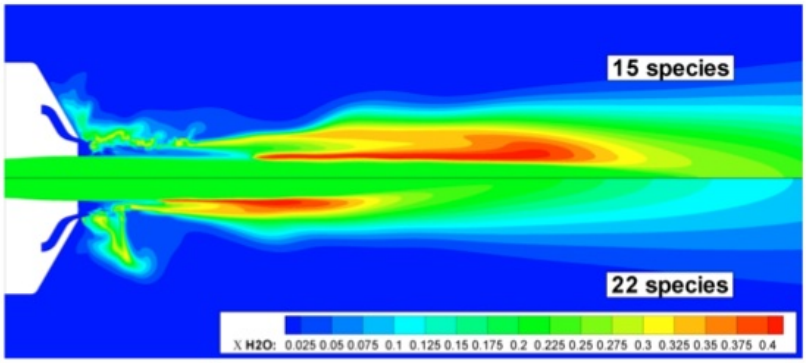

Figure 80. Computed H_2O Mole Fraction Contours for OSD-TME Experiment, Run 40a.

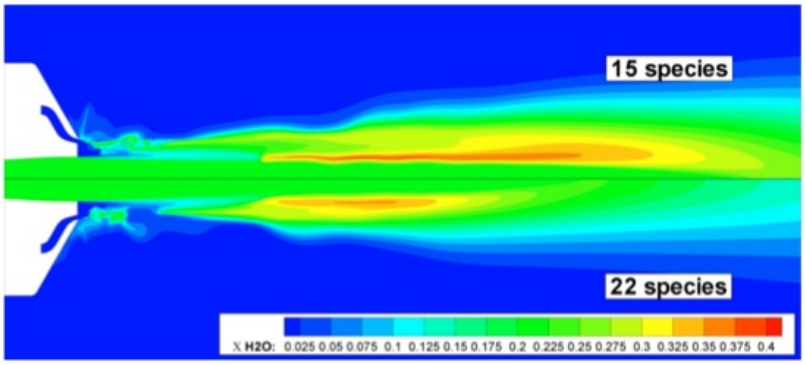

Figure 81. Computed H_2O Mole Fraction Contours for OSD-TME Experiment, Run 40b.

8 Large Eddy Simulation of High Speed Turbulent Mixing and Reaction

The filtered density function (FDF) method is being extended for subgrid scale (SGS) closure as required in large eddy simulation (LES) of high speed turbulent reacting flows [110]. The primary advantage of FDF is that the effects of SGS chemical reactions appear in a closed form. The suitable means of invoking FDF in high speed flows is via consideration of the SGS statistics of the energy, the pressure, the velocity and the scalar fields. This formulation is under way in which modeled stochastic differential equations are being developed to account for the SGS transport of all of these fields. The simplest subset of this model considers the SGS transport of the scalar field. Results are presented for the LES of scalar mixing in a high speed shear flow via this method.

8.1 Introduction

Modeling and simulation of high speed turbulent reacting flows have been the subject of widespread investigations for several decades now. The state of the practice in simulations of such flows typically solves the Reynolds averaged Navier-Stokes (RANS) equations, expanded to include scalars' transport. Closure is usually through two-equation turbulence models in conjunction with Boussinesq and gradient-diffusion assumption. Chemical reaction source terms are usually formulated using the law of mass action, and the effects of turbulence fluctuations on reaction rates are either completely ignored or modeled via eddy break up and/or assumed probability density function (PDF) methods. This first generation model has been incorporated in majority of CFD codes worldwide. This technology, however, is severely limited in many respects and the shortcomings are well documented in literature.

The physics of high speed combustion is rich with many complexities. From the modeling standpoint, some of the primary issues are the development of accurate descriptors for turbulence, chemistry, compressibility, and turbulence-chemistry interactions. The phenomenon of mixing at both micro- and macro-scales and its role and capability (or lack thereof) to provide a suitable environment for combustion and the subsequent effects of combustion on hydrodynamics, are at the heart of physics of high-speed reacting flows. From the computational viewpoint, novel strategies are needed to allow affordable simulation of complex flows with state-of-the art physical models. The power of parallel scientific computing now allows inclusion of more complex physical phenomena which in turn translate into greatly improved predictive capabilities.

It is now widely accepted that the optimum means of capturing the detailed, unsteady physics of turbulent combustion is via large eddy simulation (LES) [111, 112]. The primary issue associated with LES is accurate modeling of the subgrid scale (SGS) quantities. The filtered density function (FDF) methodology [111, 113] has proven particularly effective for this closure. The FDF is the counterpart of the probability density function (PDF) methodology in RANS [113, 114]. The idea of using the PDF method for LES was first suggested by Givi [115]. But it was the formal definition of FDF by Pope [116] which provided the mathematical foundation of LES/FDF. Within the past several years, significant progress has been made in developments and applications of the FDF. In its simplest form, the "assumed" FDF method was suggested by Madnia *et al.* [117, 118], where all of the drawbacks of this simple approach were highlighted. Similar to PDF methods, there are different ways by which transport of the FDF can be considered. These differ in the flow variables which are being considered, and whether the method is applicable to constant density or variable density flows. The marginal scalar FDF (SFDF) was developed by Colucci *et al.* [119]. This work demonstrated, for the first time, that solution of the transported FDF is possible. The

encouraging results obtained in this work motivated further research on this methodology. The scalar filtered mass density function (SFMDF), which is the variable density form of SFDF was developed by Jaberi *et al.* [120,121] and Garrick *et al.* [122]. The marginal velocity FDF (VFDF) was developed by Gicquel *et al.* [123]. The joint velocity-scalar FDF (VSFDF) was developed by Sheikhi *et al.* [124] and the joint velocity-scalar FMDF (VSFMDF) was developed by Sheikhi *et al.* [125] The first LES of a realistic flame (Sandia's piloted diffusion flame D) was conducted via SFMDF [126]. Prediction of the more complex field of a bluff-body (Sandia-Sydney Flame) by SFMDF has also been successful [127]. Following our developments of the FDF, this methodology has experienced widespread usage [128–135]. Examples are contributions in its basic implementation, [136–140] fine-tuning of its subclosures, [141–143] and its validation via laboratory experiments [138, 144–148]. The FDF is finding its way into commercial codes and has been the subject of detailed discussions in several books [113, 149–151]. Givi *et al.* [152] provide a recent review of the state of progress in LES via FDF.

Work is underway to develop the FDF method for LES of high-speed turbulent reacting flows. The ultimate goal is to extend the FDF methodology to account for SGS closure of the entire velocity-scalar field. This is envisioned to be possible via construction of the energy-pressure-velocity-scalar FMDF (EPVS-FMDF). The simplest subset of this general model is the SFMDF in which the effects of hydrodynamics must be modeleld by other (non-FDF) models. The present work considers some of these models and employs them for LES a high speed flow of interest to NASA [153–155].

8.2 Formulation

Large eddy simulation involves the spatial filtering operation:

$$\langle Q(\mathbf{x},t)\rangle_\ell = \int_{-\infty}^{+\infty} Q(\mathbf{x}',t)G(\mathbf{x}',\mathbf{x})d\mathbf{x}', \tag{17}$$

where $G(\mathbf{x}',\mathbf{x})$ denotes a filter function, and $\langle Q(\mathbf{x},t)\rangle_\ell$ is the filtered value of the transport variable $Q(\mathbf{x},t)$ in space ($\mathbf{x}$) and time (t). In variable-density flows it is convenient to use the Favre filtered quantity $\langle Q(\mathbf{x},t)\rangle_L = \langle \rho Q\rangle_\ell / \langle \rho\rangle_\ell$. We consider a filter function that is spatially and temporally invariant and localized, thus: $G(\mathbf{x}',\mathbf{x}) \equiv G(\mathbf{x}'-\mathbf{x})$ with the properties $G(\mathbf{x}) \geq 0$, $\int_{-\infty}^{+\infty} G(\mathbf{x})d\mathbf{x} = 1$. In high speed turbulent reacting flows, the primary transport variables are the density $\rho(\mathbf{x},t)$, the velocity vector $u_i(\mathbf{x},t)$ $(i = 1,2,3)$, the mass fraction, $\phi_\alpha(\mathbf{x},t)$ $(\alpha = 1,\ldots,N_s$ where N_s is the number of chemical species), the pressure $p(\mathbf{x},t)$ and the energy $e(\mathbf{x},t)$. The equations which govern the transport of these variables in space (x_i) $(i = 1,2,3)$ and time (t) are the continuity, momentum, species and energy equations along with an equation of state. The filtered form of these equations are:

$$\frac{\partial \langle \rho \rangle_\ell}{\partial t} + \frac{\partial \langle \rho \rangle_\ell \langle u_j \rangle_L}{\partial x_j} = 0 \tag{18a}$$

$$\frac{\partial \langle \rho \rangle_\ell \langle u_i \rangle_L}{\partial t} + \frac{\partial \langle \rho \rangle_\ell \langle u_j \rangle_L \langle u_i \rangle_L}{\partial x_j} = -\frac{\partial \langle p \rangle_\ell}{\partial x_i} + \frac{\partial \langle \tau_{ij} \rangle_L}{\partial x_j} - \frac{\partial \langle \rho \rangle_\ell \tau_L(u_i, u_j)}{\partial x_j} \tag{18b}$$

$$\frac{\partial(\langle \rho \rangle_\ell \langle \phi_\alpha \rangle_L)}{\partial t} + \frac{\partial(\langle \rho \rangle_\ell \langle u_i \rangle_L \langle \phi_\alpha \rangle_L)}{\partial x_i} = \frac{\partial \langle M_i^\alpha \rangle_L}{\partial x_i} - \frac{\partial \langle \rho \rangle_\ell \tau_L(\phi_\alpha, u_j)}{\partial x_j} + \langle \rho \omega_\alpha \rangle_\ell \tag{18c}$$

$$\begin{aligned} \frac{\partial \langle \rho \rangle_\ell \langle e \rangle_L}{\partial t} + \frac{\partial \langle \rho \rangle_\ell \langle u_j \rangle_L \langle e \rangle_L}{\partial x_j} &= -\frac{\partial \langle q_j \rangle_L}{\partial x_j} - \frac{\partial \langle \rho \rangle_\ell \tau_L(e, u_j)}{\partial x_j} \\ &+ \left\langle \tau_{ij} \frac{\partial u_i}{\partial x_j} \right\rangle_\ell - \left\langle p \frac{\partial u_j}{\partial x_j} \right\rangle_\ell \end{aligned} \tag{18d}$$

Here ω_α denotes the chemical reaction source term, τ_{ij} is the viscous stress tensor, M_i^α is the scalar flux, q_j is the energy flux, and

$$\tau_L(a, b) = \langle ab \rangle_L - \langle a \rangle_L \langle b \rangle_L , \tag{19}$$

denote the second-order SGS correlations. The EPVS-FDF, denoted by P_L, is formally defined as:

$$P_L(\boldsymbol{v}, \boldsymbol{\psi}, \theta, \eta, \mathbf{x}; t) = \int_{-\infty}^{+\infty} \rho(\mathbf{x}', t) \zeta(\mathbf{x}', t) G(\mathbf{x}' - \mathbf{x}) d\mathbf{x}', \tag{20}$$

where

$$\zeta(\mathbf{x}, t) = \prod_{i=1}^{3} \delta(v_i - u_i(\mathbf{x}, t)) \times \prod_{\alpha=1}^{N_s} \delta(\psi_\alpha - \phi_\alpha(\mathbf{x}, t)) \times \delta(\theta - e(\mathbf{x}, t)) \times \delta(\eta - p(\mathbf{x}, t)) . \tag{21}$$

Here δ denotes the Dirac delta function, and $\boldsymbol{v}, \boldsymbol{\psi}, \theta, \eta$ are the velocity vector, the scalar array, the internal energy and the pressure in the sample space. The term ζ is the "fine-grained" density. [156]. With the condition of a positive filter kernel, [157] P_L has all of the properties of a mass density function [158]. For further developments it is useful to define the "conditional filtered value" of the variable $Q(\mathbf{x}, t)$ as

$$\begin{aligned} &\left\langle Q(\mathbf{x}, t) \,\middle|\, \boldsymbol{u}(\mathbf{x}, t) = \boldsymbol{v}, \boldsymbol{\phi}(\mathbf{x}, t) = \boldsymbol{\psi}, e(\mathbf{x}, t) = \theta, p(\mathbf{x}, t) = \eta \right\rangle_\ell \equiv \left\langle Q \,\middle|\, \boldsymbol{v}, \boldsymbol{\psi}, \theta, \eta \right\rangle_\ell = \\ &\frac{\int_{-\infty}^{+\infty} Q(\mathbf{x}', t) \rho(\mathbf{x}', t) \zeta(\mathbf{x}', t) G(\mathbf{x}' - \mathbf{x}) d\mathbf{x}'}{P_L(\boldsymbol{v}, \boldsymbol{\psi}, \theta, \eta, \mathbf{x}; t)}. \end{aligned} \tag{22}$$

Equation (22) implies the following:

(i) for $Q(\mathbf{x}, t) = c$,
$$\left\langle Q(\mathbf{x}, t) \,\middle|\, \boldsymbol{v}, \boldsymbol{\psi}, \theta, \eta \right\rangle_\ell = c, \tag{23a}$$

(ii) for $Q(\mathbf{x}, t) \equiv \hat{Q}(\boldsymbol{u}(\mathbf{x}, t), \boldsymbol{\phi}(\mathbf{x}, t), e(\mathbf{x}, t), p(\mathbf{x}, t))$,
$$\left\langle Q(\mathbf{x}, t) \,\middle|\, \boldsymbol{v}, \boldsymbol{\psi}, \theta, \eta \right\rangle_\ell = \hat{Q}(\boldsymbol{v}, \boldsymbol{\psi}, \theta, \eta). \tag{23b}$$

(iii) Integral properties:
$$\begin{aligned} &\langle \rho(\mathbf{x}, t) \rangle_\ell \langle Q(\mathbf{x}, t) \rangle_L = \langle \rho(\mathbf{x}, t) Q(\mathbf{x}, t) \rangle_\ell = \\ &\int \left\langle Q(\mathbf{x}, t) \,\middle|\, \boldsymbol{v}, \boldsymbol{\psi}, \theta, \eta \right\rangle_\ell P_L(\boldsymbol{v}, \boldsymbol{\psi}, \theta, \eta, \mathbf{x}; t) \, d\boldsymbol{v} \, d\boldsymbol{\psi} \, d\theta \, d\eta. \end{aligned} \tag{23c}$$

From Eqs. (23) it follows that the filtered value of any function of the velocity and/or scalar variables is obtained by its integration over the velocity and scalar sample spaces

$$\langle \rho(\mathbf{x},t)\rangle_\ell \, \langle Q(\mathbf{x},t)\rangle_L = \int \ldots \int_{-\infty}^{+\infty} \hat{Q}(\boldsymbol{v},\boldsymbol{\psi},\theta,\eta) P_L(\boldsymbol{v},\boldsymbol{\psi},\theta,\eta,\mathbf{x};t)\, d\boldsymbol{v}\, d\boldsymbol{\psi}\, d\theta\, d\eta. \tag{24}$$

To develop a modeled transport equation for the EPVS-FDF, we consider the general diffusion process [159] given by the system of stochastic differential equations (SDEs):

$$\begin{aligned}
dX_i^+(t) &= D_i^X(\mathbf{X}^+,\mathbf{U}^+,\boldsymbol{\phi}^+,e^+,p^+;t)dt + B_{ij}^X(\mathbf{X}^+,\mathbf{U}^+,\boldsymbol{\phi}^+,e^+,p^+;t)dW_j^X(t) \\
&+ F_{ij}^{XU}(\mathbf{X}^+,\mathbf{U}^+,\boldsymbol{\phi}^+,e^+,p^+;t)dW_j^U(t) \\
&+ F_{ij}^{X\phi}(\mathbf{X}^+,\mathbf{U}^+,\boldsymbol{\phi}^+,e^+,p^+;t)dW_j^\phi(t), &\text{(25a)}\\
dU_i^+(t) &= D_i^U(\mathbf{X}^+,\mathbf{U}^+,\boldsymbol{\phi}^+,e^+,p^+;t)dt + B_{ij}^U(\mathbf{X}^+,\mathbf{U}^+,\boldsymbol{\phi}^+,e^+,p^+;t)dW_j^U(t) \\
&+ F_{ij}^{UX}(\mathbf{X}^+,\mathbf{U}^+,\boldsymbol{\phi}^+,e^+,p^+;t)dW_j^X(t) \\
&+ F_{ij}^{U\phi}(\mathbf{X}^+,\mathbf{U}^+,\boldsymbol{\phi}^+,e^+,p^+;t)dW_j^\phi(t), &\text{(25b)}\\
d\phi_\alpha^+(t) &= D_\alpha^\phi(\mathbf{X}^+,\mathbf{U}^+,\boldsymbol{\phi}^+,e^+,p^+;t)dt + B_{\alpha j}^\phi(\mathbf{X}^+,\mathbf{U}^+,\boldsymbol{\phi}^+,e^+,p^+;t)dW_j^\phi(t) \\
&+ F_{\alpha j}^{\phi X}(\mathbf{X}^+,\mathbf{U}^+,\boldsymbol{\phi}^+,e^+,p^+;t)dW_j^X(t) \\
&+ F_{\alpha j}^{\phi U}(\mathbf{X}^+,\mathbf{U}^+,\boldsymbol{\phi}^+,e^+,p^+;t)dW_j^U(t), &\text{(25c)}\\
de^+(t) &= D^e(\mathbf{X}^+,\mathbf{U}^+,\boldsymbol{\phi}^+,e^+,p^+;t)dt + B_j^e(\mathbf{X}^+,\mathbf{U}^+,\boldsymbol{\phi}^+,e^+,p^+;t)dW_j^e(t), &\text{(25d)}\\
dp^+(t) &= D^p(\mathbf{X}^+,\mathbf{U}^+,\boldsymbol{\phi}^+,e^+,p^+;t)dt + B_j^p(\mathbf{X}^+,\mathbf{U}^+,\boldsymbol{\phi}^+,e^+,p^+;t)dW_j^p(t), &\text{(25e)}
\end{aligned}$$

where X_i^+, U_i^+, ϕ_α^+, e^+ and p^+ are probabilistic representations of position, velocity vector, species mass fraction, energy and pressure, respectively. The D terms denote drift coefficient, the B terms denote diffusion, the F terms denote diffusion couplings, and the W terms denote the Wiener-Lévy processes [160, 161]. To model these coefficients, following Refs. [119, 123, 124, 162, 163] we are utilizing the simplified Langevin model (SLM) for closure of the velocity field and are considering several mixing models for closure of the scalar field. In order to model the internal energy and the pressure, we are expanding upon the PDF model of Delarue and Pope [164].

While the formulation of the EPVS-FMDF is being completed, we have considered the scalar subset of this model, the SFMDF, for LES of a high speed shear flow. In this case, the hydrodynamics field is approximated via conventional (non-FDF) closures. In doing so, the SGS stress tensor is first decomposed into the deviatoric and the isotropic parts:

$$\tau_L(u_i,u_j) = \tau_L^{(D)}(u_i,u_j) + \tau_L^{(I)}(u_i,u_j),$$

where

$$\tau_L^{(D)}(u_i,u_j) = \tau_L(u_i,u_j) - \frac{1}{3}\tau_L(u_k,u_k)\,\delta_{ij}\,,\ \tau_L^{(I)}(u_i,u_j) = \frac{1}{3}\tau_L(u_k,u_k)\,\delta_{ij}. \tag{26}$$

The deviatoric part is modeled via the Smagorinsky model [165, 166]:

$$\tau_L^{(D)}(u_i,u_j) = -2\,\nu_T\Big(\langle S_{ij}\rangle_L - \frac{1}{3}\langle S_{kk}\rangle_L\,\delta_{ij}\Big), \tag{27}$$

where

$$\langle S_{ij}\rangle_L = \frac{1}{2}\Big(\frac{\partial\langle u_i\rangle_L}{\partial x_j} + \frac{\partial\langle u_j\rangle_L}{\partial x_i}\Big), \tag{28}$$

is the filtered rate of strain and ν_T is the SGS viscosity:

$$\nu_T = C_s\, l^2 \Big(\langle S_{ij}\rangle_L \langle S_{ij}\rangle_L\Big)^{\frac{1}{2}}, \tag{29}$$

where l is the characteristic length of the filter and the parameter C_s is the Smagorinsky constant, which is assigned a value or computed dynamically. For the isotropic part, the Yoshizawa's model [167] is used:

$$\tau_L^{(I)}(u_i, u_j) = \frac{2}{3} C_I \, l^2 \Big(\langle S_{mn} \rangle_L \langle S_{mn} \rangle_L \Big) \delta_{ij} \tag{30}$$

with C_I being a constant. The model of Eidson [168] is used for the SGS scalar fluxes:

$$\tau_L(e, u_i) = -\frac{\nu_T}{Pr_T} \frac{\partial \langle e \rangle_L}{\partial x_i}, \quad \tau_L(\phi_\alpha, u_i) = -\frac{\nu_T}{Sc_T} \frac{\partial \langle \phi_\alpha \rangle_L}{\partial x_i}, \tag{31}$$

where Pr_T and Sc_T are the SGS Prandtl and Schmidt numbers, respectively.

8.3 Results

The SFMDF methodology is used for LES of the flow configuration considered by Cutler *et al.* [169, 170] This configuration is shown in Fig. 82 and consists of a non-reacting coaxial axisymmetric jet with a center jet composition of oxygen and helium (5% and 95% by volume, respectively) and a coflow of air. The diameters of the center jet and the coflow

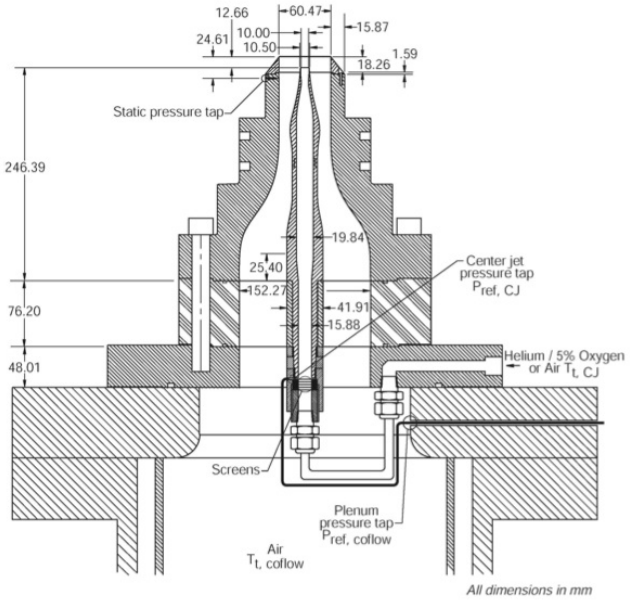

Figure 82. Schematic of the coaxial jet facility [169, 170].

are 10mm and 60mm respectively. Measurements are provided from the nozzle exit to a downstream distance of 261mm. Both streams are discharged to ambient at 1 atmosphere and at Mach 1.8. The velocity of the center jet, however, is more than that of the coflow since the jet is of a lighter gas with a higher speed of sound. The total temperature of both the center jet and the coflow is about 300K. Computations are performed on a domain spanning 121mm $\times$ 50mm $\times$ 50mm diameters in the streamwise (x), cross-stream (y), and spanwise (z) directions, with a Cartesian grid with $158 \times 65 \times 65$ nodes, respectively. The flow field is initialized to the inlet averaged filtered values. At the inflow, the average values from the experiment are specified for all variables, except for the inlet axial velocity, where small perturbations are superimposed on the mean profile at the fundamental jet

Constant	Simulation I	Simulation II	Simulation III
C_s	0.014 (Erlebacher *et al.* [165])	Dynamic Model (Moin *et al.* [173])	Dynamic Model (Moin *et al.* [173])
C_I	0.0066 (Speziale *et al.* [174])	0.0066 (Speziale *et al.* [174])	0.0066 (Speziale *et al.* [174])
Pr_T	0.75 (Eidson [168], Cutler *et al.* [170])	Dynamic Model (Moin *et al.* [173])	Dynamic Model (Moin *et al.* [173])
Sc_T	equal to Pr_T (Cutler *et al.* [169])	equal to Pr_T (Cutler *et al.* [169])	Dynamic Model (Moin *et al.* [173])

Table 14. Model Constants

instability frequency and its first two sub-harmonics [171]. At free streams, zero derivative boundary condition is used [172]. At the outlet, in the case of supersonic outflow, 2^{nd} order extrapolation is used. At subsonic outflow, the total pressure and temperature are specified and the velocities and mass fractions are extrapolated [169]. Three sets of simulations are conducted with different ways by which the model constants are specified. Table 14 provides a listing of all of the constants. These are either kept fixed or computed dynamically. In the latter, the dynamic procedure of Moin *et al.* [173] is used.

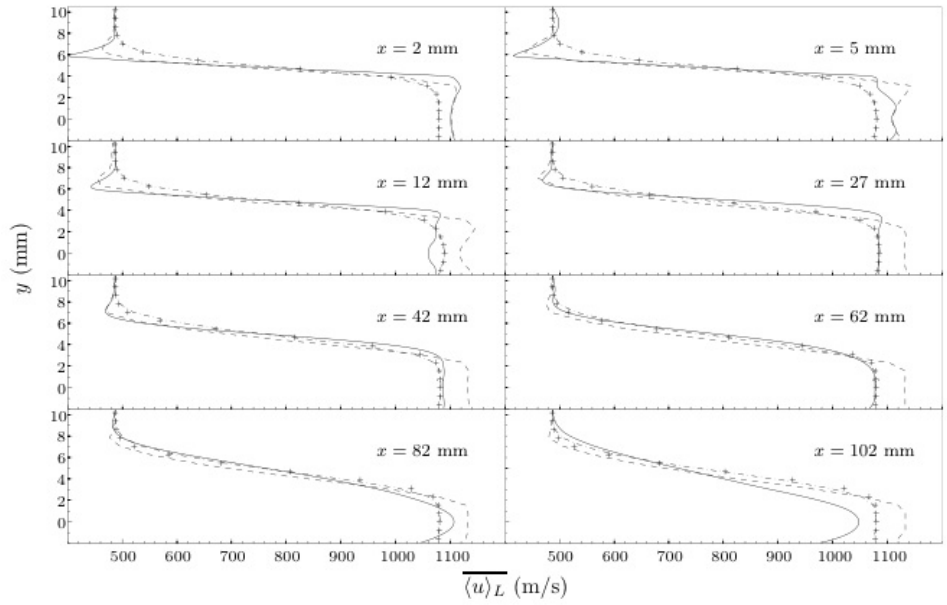

Figure 83. Average filtered velocity profiles. − Experiment, −− Simulation I, −.− Simulation III.

In dynamic simulations, the "test" filter was chosen to be twice the width of the primary filter. For stability of the dynamic simulations, the model constants were forced to be the same as the average value of the constants over the whole domain. Some sample results are presented here.

Figures 83 and 84 show the values of averaged filtered axial velocity, $\overline{\langle u \rangle_L}$, and averaged mass fraction of center jet, $\overline{\langle \phi_{He-O_2} \rangle_L}$. Here, the over-bar denotes the ensemble average

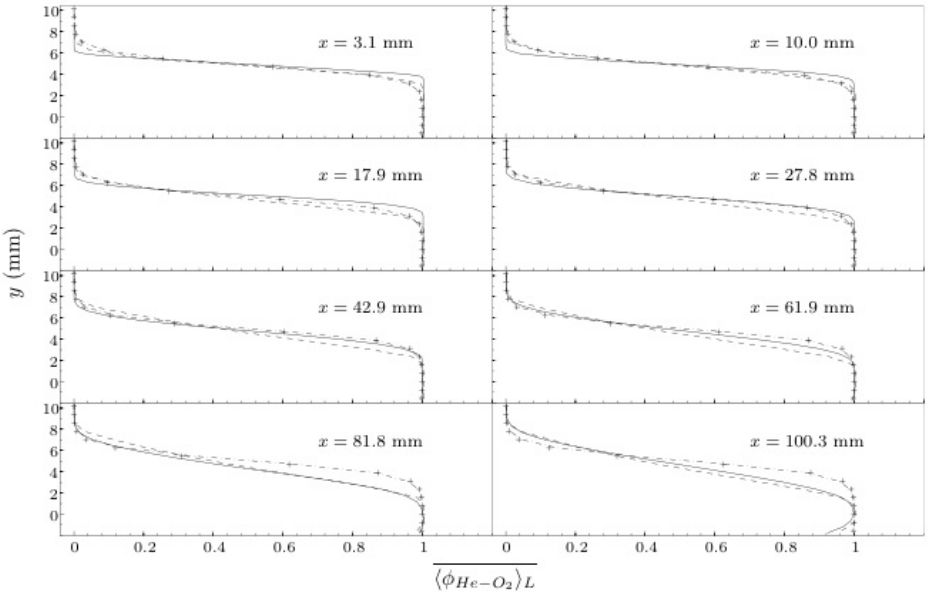

Figure 84. Profiles of average filtered mass fraction of center jet. − Experiment, −− Simulation I, −.− Simulation III.

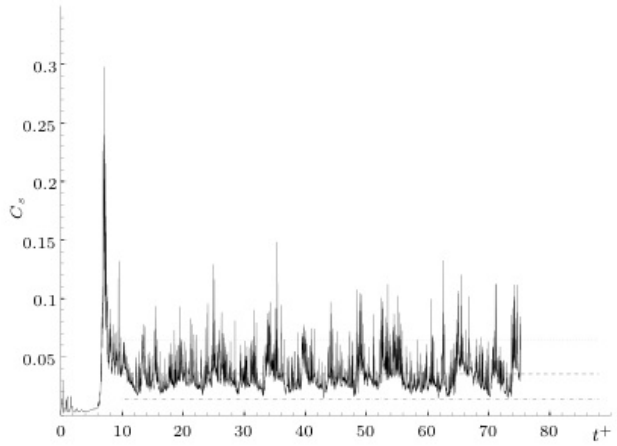

Figure 85. Computed values of the Smagorinsky coefficient versus time. − time history from Simulation III, −− average value from Simulation III, −.− average value from Simulation I, ⋯ value used by Rizzetta *et al.* [175].

values (obtained by averaging over time and the homogeneous azimuthal direction). Results of Simulation II are very similar to those of Simulation III and are not shown. It is seen that, in general, the dynamic model provides better agreement for velocity, while $\overline{\langle \phi_{He-O_2} \rangle_L}$ is predicted better in Simulation I. To investigate this issue, the values of C_s as obtained by dynamic models are given in Fig. 85. It is observed that C_s values from Simulation III are, in average, higher than those in Simulation I. Also shown in Fig. 85 is the value of C_s suggested by Rizzetta *et al.* [175]. This is higher than both of the values incorporated here. These results are to be compared with those of the general EPVS-FMDF formulation

currently underway.

8.4 Conclusions

The filtered mass density function (FMDF) is now *in vogue* because it has proven very effective for reliable and affordable prediction of turbulent combustion systems. Since its original development a decade ago, the scalar FMDF (SFMDF) has experienced widespread applications for LES of a variety of reacting flows. The methodology has found its way in industry, and is now covered as a powerful predictive tool in most modern text- and handbooks. This popularity is partially due to the demonstrated capability of the method to exactly account for the effects of chemical reactions. The extended methodology, the joint velocity-scalar FMDF (VSFMDF), is significantly more powerful as it also accounts for the effects of subgrid scale (SGS) convection in an exact manner.

The present work demonstrates the feasibility of SFMDF for LES of high speed reacting flows. In this case the effects of convection are modeled via conventional SGS closures which perform reasonably well. Therefore, the method is recommended for routine predictions of high speed reacting flows (for which LES is desired). Hopefully, the VSFMDF will be ready for such predictions in the near future. Given its potential, it is expected that VSFMDF will be the primary method of FDF predictions a decade or so from now.

9 Project Conclusions

This report describes work involving the development of phenomenological models for Reynolds averaged Navier-Stokes codes, subgrid scale models used in large-eddy simulation and reduced-kinetics models to study the effects of vitiation on engine testing in combustion heated facilities. Two fundamental experiments were performed to provide data used in the development and refinement of these models. Experimental data was extracted from the experiments using nonintrusive diagnostics that allowed simultaneous measurement of temperature, species, and two components of velocity in supersonic flow without changing the character of the flowfield. The data was analyzed using a response surface methodology that provided an efficient means of determining critical parameters in a chosen model. The models that were developed were then incorporated into four combustion codes used in fundamental combustion research and engine flowpath analysis and design.

In addition to advancing the capability of several combustion codes currently employed for propulsion system research and development in the United States, the OSD Test Media Effects Project should also serve as a model for future combustion research using the combined capabilities of experimental, diagnostic and computational approaches. The effort involved a close collaboration between researchers in each of the required disciplines with success in each discipline highly dependent upon the results obtained in the other two areas. This linkage resulted in enhanced communication between all of the researchers ensuring that nearly all needs in each area were met.

References

1. Cutler, A. D., Magnotti, G., Capriotti, D. P., and Mills, C. T., Supersonic Combusting Jet Experiments for Code Development and Validation, 55th JANNAF Propulsion Meeting, Boston, MA, 2008.

2. Baurle, R.A., Modeling of High Speed Reacting Flows: Established Practices and Future Challenges, AIAA Paper 2004-267, 42nd Aerospace Sciences Meeting and Exhibit, Reno, NV, Jan. 2004.

3. Cutler, A.D., Danehy, P.M., Springer, R.R., OByrne, S., Capriotti, D.P., DeLoach, R., Coherent Anti-Stokes Raman Spectroscopic Thermometry in a Supersonic Combustor, AIAA J., Vol. 41, No. 12, Dec. 2003.

4. Lucht, R.P., Three-laser coherent anti-Stokes Raman scattering measurements of two species, Optics Letters, Vol. 12, No. 2, February 1987, pp. 78-80.

5. Hancock, R.D., Schauer, F.R., Lucht, R.P. and Farrow, R.L., Dual-pump coherent anti-Stokes Raman scattering measurements of nitrogen and oxygen in a laminar jet diffusion flame, Applied Optics, Vol. 36, No. 15, 1997.

6. O'Byrne, S., Danehy, P.M., Cutler, A.D., Dual-Pump CARS Thermometry and Species Concentration Measurements in a Supersonic Combustor, AIAA Paper 2004-0710, 42nd Aerospace Sciences Meeting, Reno, NV, Jan. 2004.

7. Tedder, S. A., OByrne, S., Danehy, P. M., Cutler, A. D., CARS Temperature and Species Concentration Measurements in a Supersonic Combustor with Normal Injection, AIAA Paper 2005-0616, 43rd AIAA Aerospace Sciences Meeting, Reno, NV, Jan. 2005.

8. Goyne, C.P., McDaniel, J.C., Krauss, R.H., Day, S.W., Velocity measurement in a dual-mode supersonic combustor using particle image velocimetry, AIAA Paper 2001-1761, AIAA/NAL- NASDA-ISAS International Space Planes and Hypersonic Systems and Technologies Conference, 10th, Kyoto, Japan, Apr. 2001.

9. Bresson, A., Bouchardy, P., Magre, P., Grisch, F., OH/acetone PLIF and CARS thermometry in a supersonic reactive layer, AIAA Paper 2001-1759, AIAA/NAL-NASDA-ISAS International Space Planes and Hypersonic Systems and Technologies Conference, 10th, Kyoto, Japan, Apr. 2001.

10. Drummond, J.P., Danehy, P.M., Bivolaru, D., Gaffney, R.L., Parker, P., Chelliah, H.K., Cutler, A.D., Givi, P., Hassan, H.A., Predicting the Effects of Test Media in Ground-Based Propulsion Testing, 2006 Annual ITEA Technology Review, Cambridge, MA, August 710, 2006.

11. Drummond, J.P., Danehy, P.M., Bivolaru, D., Gaffney, R.L., Tedder, S.A., Cutler, A.D., Modeling Combustion in Supersonic Flows, Proceedings of 3rd International Symposium on Non-Equilibrium Processes, Plasma, Combustion, and Atmospheric Phenomena (NEPCAP 2007), Sochi, Russia, June 25-29, 2007.

12. Drummond, J.P., Danehy, P.M., Bivolaru, D., Gaffney, R.L., Tedder, S.A., Cutler, A.D., Supersonic combustion research at NASA, 2007 Fall Technical Meeting, Eastern States Section of the Combustion Institute, University of Virginia, Oct. 21-24, 2007.

13. Bivolaru, D., Danehy, P.M., Lee, J.W., Gaffney, R.L., Cutler, A.D., Single-pulse, Multi-point Multi-component Interferometric Rayleigh Scattering Velocimeter, AIAA-2006-836, 44th AIAA Aerospace Sciences Meeting, Reno, NV, 9-12 Jan., 2006.

14. Tedder, S., Bivolaru, D., Danehy, P. M., Weikl, M.C., Beyrau, F., Seeger, T., Cutler, A. D., Characterization of a Combined CARS and Interferometric Rayleigh Scattering System and Demonstration in a Mach 1.6 Combustion-Heated Jet, AIAA-2007-0871, 45th AIAA Aerospace Sciences Meeting and Exhibit, Reno, NV, Jan. 8-11, 2007.

15. Bivolaru, D., Grinstead, K. D., Tedder S., Lee, J. W., Danehy, P.M., Cutler A. D., Simultaneous Temperature, Concentration, and Velocity Measurements for Combustion Using CARS and Rayleigh Scattering, AIAA AMT-GT Technology Conference, San Francisco, June, 2007.

16. Bivolaru, D., Danehy, P.M., Gaffney, R.L., Jr., Cutler, A.D., Direct-View Multi-Point Two- Component Interferometric Rayleigh Scattering System, AIAA 2008-236, 46th Aerospace Sciences Meeting, Reno, NV, Jan 7-10, 2008.

17. Antcliff, R. R., Jarrett, O., Jr., Chitsomboon, T., Cutler, A. D., CARS Measurements of Temperature and Species Number Density in Supersonic Combusting Flow, AIAA-88-4662, AIAA/NASA/AFWAL Conference on Sensors and Measurement Techniques for Aeronautical Applications, Sep. 7-9, 1988.

18. Gaffney, R.L., Jr., Cutler, A.D., CFD Modeling Needs and What Makes a Good Supersonic Combustion Experiment, JANNAF Meeting, June 2005.

19. Guy, R.W., Rogers, R.C., Puster, R.L., Rock, K.E., Diskin, G.L., The NASA Langley Scramjet Test Complex, AIAA-96-3243, 32nd AIAA/ASME/SAE/ASEE Joint Propulsion Conference and Exhibit, Lake Buena Vista, Florida, July 1-3, 1996.

20. Danehy, P.M., Magnotti, G., Bivolaru, D., Tedder, S., Cutler, A.D., Simultaneous Temperature, Composition, and Velocity Measurements in a Large-scale, Supersonic, Heated Jet, 55th JANNAF Propulsion Meeting, Boston, MA, May 12-16, 2008.

21. Cutler, A.D., Magnotti, G., Baurle, R., Bivolaru, D., Tedder, S., Danehy, P.M., Weikl, M.C., Beyrau, F., and Seeger, T., Development of Supersonic Combustion Experiments for CFD Modeling, AIAA-2007-0978, 45th AIAA Aerospace Sciences Meeting and Exhibit, Reno, NV, Jan. 8-11, 2007.

22. Gaffney R. L., Jr., Numerical Simulation of a Co-Axial Supersonic-Combusting free-jet Experiment, JANNAF2008, Massachusetts, May, 2008

23. Bivolaru, D., Danehy, P.M., Lee, J.W., Gaffney, R.L., Cutler, A.D., "Single-pulse, Multi-point Multi-component Interferometric Rayleigh Scattering Velocimeter," AIAA 2006-836, January, 2006.

24. Drummond, J.P., Danehy, P.M., Bivolaru, D., Gaffney, R.L., Parker, P., Chelliah, H.K., Cutler, A.D., Givi, P., Hassan, H.A., "Predicting the Effects of Test Media in Ground-Based Propulsion Testing," 2006 Annual ITEA Technology Review, August, 2006.

25. Tedder, S., Bivolaru, D., Danehy, P. M., Weikl, M.C., Beyrau, F., Seeger, T., Cutler, A. D., "Characterization of a Combined CARS and Interferometric Rayleigh Scattering System and Demonstration in a Mach 1.6 Combustion-Heated Jet," AIAA 2007-0871, January, 2007.

26. Drummond, J.P., Danehy, P.M., Bivolaru, D., Gaffney, R.L., Tedder, S.A., Cutler, A.D., "Modeling Combustion in Supersonic Flows," Proceedings 3rd International Symposium on Non-Equilibrium Processes, Plasma, Combustion, and Atmospheric Phenomena (NEPCAP 2007), June, 2007.

27. Bivolaru, D., Grinstead, K. D., Tedder S., Lee, J. W., Danehy, P.M., Cutler A. D., "Simultaneous Temperature, Concentration, and Velocity Measurements for Combustion Using CARS and Rayleigh Scattering," AIAA AMT-GT Technology Conference, June, 2007.

28. Drummond, J.P., Danehy, P.M., Bivolaru, D., Gaffney, R.L., Tedder, S.A., Cutler, A.D., "Supersonic combustion research at NASA," 2007 Fall Technical Meeting, Eastern States Section of the Combustion Institute, October, 2007.

29. Bivolaru, D., Danehy, P.M., Gaffney, R.L., Jr., Cutler, A.D., "Direct-View Multi-Point Two-Component Interferometric Rayleigh Scattering System," AIAA 2008-236, January, 2008.

30. Danehy, P.M., Tedder, S., Magnotti, G., Bivolaru, D., Cutler, A.D., "Simultaneous Temperature, Composition, and Velocity Measurements in a Large-scale, Supersonic, Heated Jet," 55th JANNAF Propulsion Meeting, May, 2008.

31. Gaffney, R. L., Jr. and Cutler, A. D, "CFD Modeling Needs And What Makes A Good Supersonic Combustion Validation Experiment," JANNAF CS/APS/PSHS/MSS Joint Meeting, June, 2005.

32. Guy, Robert W., Rogers, R. Clayton, Puster, Richard L., Rock, Kenneth E. and Diskin, Glenn S., "The NASA Langley Scramjet Test Complex," AIAA 1996-3243.

33. White, J. A. and Morrison, J. H., "A Pseudo-Temporal Multi-Grid Relaxation Scheme for Solving the Parabolized Navier-Stokes Equations," AIAA 99-3360, June, 1999.

34. McBride, B. J., Gordon, S. and Reno, M. A., "Thermodynamic Data for Fifty Elements," NASA TP-3287, January, 1993.

35. Wilcox, D. C., *Turbulence Modeling for CFD*, 2^{nd} ed., San Diego, Ca.: DCW Industries, 2006.

36. Tedder, S., P. M. Danehy, Magnotti, G. and Cutler, A. D., CARS Temperature Measurements in a Combustion-Heated Mach 1.6 Jet, AIAA-2009-0524, 47th AIAA Aerospace Sciences Meeting, Orlando, FL, January, 2009.

37. OByrne, S., Danehy, P.M., Tedder, S.A., Cutler, A.D., Dual-Pump Coherent Anti-Stokes Raman Scattering Measurements in a Supersonic Combustor, AIAA J., Vol. 45, No. 4, p. 922-933, April 2007.

38. Anderson, T. J. and Eckbreth, A. C., Stimultaneous Coherent Anti-Stokes Raman Spectroscopy Measurements in Hydrogen-Feuled Supersonic Combustion, J. Propulsion, Vol 8, NO. 1, Jan. 1992.

39. Eckbreth, A. C., Anderson,T. J., and Dobbs, G. M., Multi-ColorCARS for Hydrogen-Fueled Scramjet Applications, Applied Physics B, Vol. 45, 1988, pp. 215223.

40. Magre, P., Collin, G., Pin, O., Badie, J.M., Olalde, G., Clement, M., Temperature measurements by CARS and intrusive probe in an air-hydrogen supersonic combustion Int. Journal of Heat and Mass Transfer, Vol. 44, pp. 4095-4105, 2001.

41. Smith, M. W., Jarratt, O., Jr., Antcliffe, R. R., Northam, G. B., Cutler, A. D., and Taylor, D. J., Coherent Anti-Stokes Raman Spectroscopy Temperature Measurements in a Hydrogen-Fueled Supersonic Combustor, Journal of Propulsion and Power, Vol. 9, No. 2, 1993,pp. 163168.

42. Yang, S. R., Zhau, J. R., Sung, G. J., and Yu, G., Multiplex CARS Measurements in Supersonic Hydrogen/Air Combustion, Applied Physics B, Lasers and Optics, Vol. 68, No. 2, 1999, pp. 257265.

43. Vereschagin, K. A., Smirnov, V. V., Stelmakh, O. M., Fabelinski, V. I., Sabelnikov, V. A., Ivanov, V. V., Clauss, W., and Oschwald, M., Temperature Measurements by Coherent Anti-Stokes Raman Spectroscopy in Hydrogen-Fuelled Scramjet Combustor, Aerospace Science and Technology, Vol. 5, No. 5, 2001, pp. 347355.

44. Tedder, S., OByrne, S., Danehy, P. M., and Cutler, A. D., CARS Temperature and Species Concentration Measurements in a Supersonic Combustor with Normal Injection, AIAA Paper 2005-616, Jan. 2005.

45. Bivolaru, D, Danehy, P.M., Grinstead, K.D., Jr., Tedder, S., and Cutler, A.D., Simultaneous CARS and Interferometric Rayleigh Scattering, AIAA-2006-2968, 25th AIAA Aerodynamic Measurement Technology and Ground Testing Conference, San Francisco, CA, June 5-8, 2006.

46. Bivolaru D. et al. Spatially and Temporally Resolved Measurements of Velocity in a H_2- Air Combustion- Heated Supersonic Jet AIAA Paper 2009-0027, Jan. 2009.

47. Bivolaru, D., Lee, J. W., Jones, S. B., Tedder, S., Danehy, P. M., Weikl, M. C., Magnotti, G., Cutler, A. D., Mobile CARS- IRS Instrument for Simultaneous Spectroscopic Measurement of Multiple Properties in Gaseous Flows, 22nd International Congress on Instrumentation in Aerospace Simulation Facilities, Asilomar Conference Center, Pacific Grove, California, June 10 14, 2007

48. Bivolaru, D., Danehy, P. M., Lee, J. W., Gaffney, Jr. R. L., and Cutler, A. D., Single-pulse Multi-point Multi-component Interferometric Rayleigh Scattering Velocimeter, AIAA-2006-0836, 44th Aerospace Sciences Meeting, Reno, NV, January 9-12,2006

49. Bivolaru, D., Danehy, P. M., and Lee, J. W, Intracavity Rayleigh-Mie Scattering for multipoint, two-component velocity measurement, Optics Letters, Vol. 31, No. 11, pp. 1645-1647, June, 2006.

50. Eckbreth, A.C., Laser Diagnostics for Combustion Temperature and Species (Gordon & Breach, Amsterdam, Nederland, 1996).

51. Palmer, R. E., The CARSFT Computer Code for Calculating Coherent Anti-Stokes Raman Spectra: User and Programmer Information, Sandia National Laboratories Report SAND89-8206, Livermore, CA,1989.

52. Hancock, R. D., Bertagnolli, K. E., and Lucht, R. P., Nitrogen and Hydrogen CARS Temperature Measurements in a Near-Adiabatic, Surface- Mixing (Hencken) Burner, Combustion and Flame, Vol.109,1997,pp.323331.

53. Hancock, R. D., Schauer, F. R., Lucht, R. P., and Farrow, R. L., Dual-Pump Coherent Anti-Stokes Raman Scattering (CARS) Measurements of Hydrogen and Oxygen in a Laminar Jet Diffusion Flame, Applied Optics, Vol. 36, 1997, pp. 32173226.

54. OByrne, S., Danehy, P. M., and Cutler, A. D., $N-2/O-2/H_2$ Dual-Pump CARS: Validation Experiments, 20th International Congress on Instrumentation in Aerospace Simulation Facilities, Gttingen, Germany, Aug. 2003.

55. Danehy, P. M., OByrne, S., Cutler, A. D., and Rodriguez, C. G., Coherent Anti-Stokes Raman Scattering (CARS) as a Probe for Supersonic Hydrogen-Fuel/Air Mixing, Proceedings of the JANNAF APS/CS/PSHS/MSS Joint Meeting [CD-ROM], CPIA, Columbia, MD, Dec. 2003.

56. Bivolaru, D., Danehy, P. M., Gaffney, Jr., R. L. and Cutler, A. D., Direct-View Multi-Point Two-Component Interferometric Rayleigh Scattering Velocimeter, AIAA Paper 2008-236, Jan. 2008.

57. Bivolaru, D., Danehy, P. M., Cutler, A. D., Multipoint Inteferometric Rayleigh Scattering using Light Recirculation, Paper Number 2008-3708, 26th AIAA Aerodynamic Measurement Technology and Ground Testing Conference, Seattle, WA June 23-26, 2008

58. Yuceil, K. B., Otugen, M. V., Scaling Parameters for Underexpanded Supersonic Jets, Physics of Fluids, Vol. 14, Nr. 12, December 2002.

59. Chelliah, H. K., Final OSD - Air Force Report on the Test Media Effects Project — Kinetics, 2009.

60. Drummond, J.P., A Two-Dimensional Numerical Simulation of a Supersonic, Chemically Reacting Mixing Layer, NASA TM 4055, 1988.

61. Singh, D.J. and Jachimowski, C.J., AIAA J. 32(1):213-216 (1993).

62. Lee, C. M. and Kundu, K., Simplified Jet-A Kinetic Mechanism for Combustion Application, AIAA Paper 1993-0001, Jan. 1993.

63. Tsang, W., Progress in the development of a combustion kinetics database for liquid fuels, 4th Joint Meeting of the U.S. Sections, March 20-23, 2005, Philadelphia, PA.

64. Qin, Z., Lissianski, V., Yang, H., Gardiner, W.C.Jr., Davis, S.G., and Wang, H., Proc. Combust. Inst., 28:1663-1669 (2000).

65. Westbrook, C., Lawrence-Livermore National Laboratory, private communication.

66. UCSanDiego Chemical Kinetic Mechanisms, http://maemail.ucsd.edu/ combustion/cermech/

67. GRI 3.0, http://www.me.berkeley.edu/mech/

68. Hughes, K.J., Turanyi, T., Clague, A.R., and Pilling, M.J., Int. J. Chem. Kinet. 33(9):513-538 (2001).

69. Carrierre, T., Westmorland, P.R., Kazakov, A., Stein, Y.S., and Dryer, F.L., Proc. Com- bust. Inst., 29:1257-1266 (2002).

70. Simmie, J., Prog. Energy Combust. Sci. 29:599-634 (2003).

71. Bodenstein, M., Z. Phys. Chem. 85:329 (1913).

72. Langmuir, I., J. Am. Chem. Soc. 37(5):1139 (1915)

73. Keck, J.C. and Gillespie, D., Combust. and Flame 17:237-241 (1971).

74. Jones, W.P. and Rigopoulos, S., Proc. Combust. Inst. 30:1325-1331 (2005).

75. Peters, N., in Numerical Simulation of Combustion Phenomena (R. Glowinski, B. Larrouturou, and T. Temam, eds.), Lecture Notes in Physics, Springer-Verlag, Vol. 214:90 (1985).

76. Zambon, A.C. and Chelliah, H.K., Development of a Skeletal Reaction Model for Igni- tion, Flame Propagation and Extinction of C3 Hydrocarbon Fuels, Fourth Joint Meeting of the U.S. Sections of the Combustion Institute, Philadelphia, PA, March, 2005.

77. Zambon, A.C. and Chelliah, H.K., Explicit Reduced Reaction Models for Ignition, Flame Propagation and Extinction of C_2 H_4 /CH_4 /H_2 and Air Systems, Combust. and Flame 150:71-91 (2007).

78. Williams, F.A., Combustion Theory, 2nd ed., Addison-Wesley (1985).

79. Peters, N. and Williams, F.A. Combust. and Falme 68:185 (1987).

80. Seshadri, K. and Peters, N. Combust. and Flame 73:23 (1988).

81. Chelliah, H.K. and Williams, F.A., Combust. and Flame 80, p.17 (1990).

82. Bilger, R. W., Starner, S. H., and Kee, R. J., Combust. Flame, 80:135149 (1990).

83. Wang, W. and Rogg, B., Premixed Ethylene/Air and Ethane/Air Flames: Reduced Mechanisms Based on Inner Iterations, in Reduced Kinetic Mechanisms for Applications in Combustion Systems, Lecture Notes in Physics, Vol. M15, Springer Verlag, 1993.

84. Lam, H., Singular Perturbation for Stiff Equations Using Numerical Methods, in Recent Advances in the Aerospace Sciences (C. Casci, Editor), Plenum Press, New York, 1985, pp. 3-20.

85. Lovas, T., Amneus, P., and Mauss, F., Proc. Combust. Inst. 28:1809-1815 (2000).

86. Lu, T., Ju, Y., and Law, C.K., Combust. and Flame 126:1445-1455 (2001).

87. Bhaskaran KA, Gupta MC, Just TH, Combust. and Flame, 21:45-48 (1973).

88. Baker, J.A. and Skinner, G.B., Combust. and Flame, 19:347-350 (1972).

89. Freeman, G. and Lefebrve, A.H., Combust. and Flame 58: 153-162 (1984).

90. Colket, M., et al. Development of an Experimental Database and Kinetic Models for Sur- rogate Jet Fuels, AIAA 2007-770, 45th AIAA Aerospace Sciences Meeting and Exhibit 8 - 11 January 2007, Reno, Nevada.

91. Sobel, D.R. and Spadaccini, L.J., Hydrocarbon Fuel Cooling Technologies for Advanced Propulsion, ASME-95-GT-226, June 1995.

92. Colket, M.B. and Spadaccini, L.J., J. Propulsion and Power 17(2):315-323 (2001).

93. Keistler, P. G. and Hassan, H. A., Simulation of Supersonic Combustion Involving H_2/Air and C_2H_4/Air, AIAA Paper 2009-0028, Jan. 2009.

94. Baurle, R. A., and Eklund, D. R., Analysis of Dual-Mode Hydrocarbon Scramjet Operation at Mach 4 6.5, Journal of Propulsion and Power, Vol. 18, No. 5, 2002, pp 990-1002.

95. Robinson, D. F. and Hassan, H. A., Further Development of the k-ζ (Enstrophy) Turbulence Closure Model, AIAA Journal, Vol. 36, No. 10, 1998, pp. 1825-1833.

96. Alexopoulos, G. A., A k-ζ (Enstrophy) Compressible Turbulence Model for Mixing Layers and Wall Bounded Flows, AIAA Journal, Vol. 35, No. 7, 1997, pp. 1221-1224.

97. Samimy, M., and Elliot, G. S., Effect of Compressibility on Characteristics of Free Shear Layers, AIAA Journal, Vol. 28, No.3, 1990, pp. 439-445.

98. Elliot, G. S., and Samimy, M., Compressible Effects in Free Shear Layers, Physics of Fluids A, Vol. 2, No. 7, 1990, pp. 1231-1240.

99. Goebel, S. G., and Dutton, J. C., Experimental Study of Compressible Turbulent Mixing Layers, AIAA Journal, Vol. 29, No. 4, 1991, pp 538-546.

100. Baurle, R. A., Hsu, A. T., and Hassan, H. A., Assumed and Evolution Probability Density Functions in Supersonic Turbulent Combustion Calculations, Journal of Propulsion and Power, Vol. 11, No. 6, 1995, pp. 1132-1138.

101. Xiao, X., Hassan, H. A., and Baurle, R. A., Modeling Scramjet Flows with Variable Turbulent Prandtl and Schmidt Numbers, AIAA Journal, Vol. 45, No. 6, 2007, pp. 1415-1423.

102. Jachimowski, C. J., An Analytic Study of the Hydrogen-Air Reaction Mechanism with Application to Scramjet Combustion, NASA Technical Paper 2791, February 1988.

103. Connaire, M. O., Curran, H. J., Simmie, J. M., Pitz, W. J., and Westbrook, C. K., A Comprehensive Modeling Study of Hydrogen Oxidation, International journal of Chemical Kinetics, Vol. 36, 2004, pp. 603-622.

104. Gokulakrishnan, P., Pal, S., Klassen, M. S., Hamer, A. J., Roby, R. J. Kozaka, O., and Menon, S., Supersonic Combustion Simulation of Cavity-Stabilized Hydrocarbon Flames Using Ethylene Reduced Kinetic Mechanism, AIAA Paper 2006-5092, July 2006.

105. Lin, K., Ryan, M. Carter, C., Gruber, M., and Raffoul, C., Scalability of Ethylene Gaseous Jets for Fueling Scramjet Combustors at Various Scales, AIAA Paper 2009-1423, Jan. 2009.

106. Launder, B. E., Heat and Mass Transport, Turbulent Topics in Applied Physics, edited by P. Bradshow, Vol. 12, Springer-Verlag, Berlin, 1978.

107. Wilcox, D. C., Turbulence Modeling for CFD, 2nd Edition, DCW Industries, Inc., La Caada, CA 1998.

108. Edwards, J. R., Advanced Implicit Algorithm for Hydrogen-Air Combustion Calculation, AIAA Paper 1996-3129, June, 1996.

109. Edwards, J. R., A Low Diffusion Flux Splitting Scheme for Navier-Stokes Calculation, Computers and Fluids, Vol. 26, No. 10, 1997, pp. 635-659.

110. Nik, M. B., Mohebbi, M., Sheikhi, M. R. H., and Givi, P., Progress in Large Eddy Simulation of High Speed Turbulent Mixing and Reaction, AIAA Paper 2009-0133, Jan. 2009.

111. Givi, P., "Filtered Density Function for Subgrid Scale Modeling of Turbulent Combustion," *AIAA J.*, Vol. 44, No. 1, 2006, pp. 16–23.

112. Poinsot, T. and Veynante, D., *Theoretical and Numerical Combustion*, Edwards, Philadelphia, PA, 2nd ed., 2005.

113. Pope, S. B., *Turbulent Flows*, Cambridge University Press, Cambridge, UK, 2000.

114. Libby, P. A. and Williams, F. A., editors, *Turbulent Reacting Flows*, Academic Press, London, UK, 1994.

115. Givi, P., "Model Free Simulations of Turbulent Reactive Flows," *Prog. Energy Combust. Sci.*, Vol. 15, 1989, pp. 1–107.

116. Pope, S. B., "Computations of Turbulent Combustion: Progress and Challenges," *Proc. Combust. Inst.*, Vol. 23, 1990, pp. 591–612.

117. Madnia, C. K. and Givi, P., "Direct Numerical Simulation and Large Eddy Simulation of Reacting Homogeneous Turbulence," *Large Eddy Simulations of Complex Engineering and Geophysical Flows*, edited by B. Galperin and S. A. Orszag, chap. 15, Cambridge University Press, Cambridge, England, 1993, pp. 315–346.

118. Frankel, S. H., Adumitroaie, V., Madnia, C. K., and Givi, P., "Large Eddy Simulations of Turbulent Reacting Flows by Assumed PDF Methods," *Engineering Applications of Large Eddy Simulations*, edited by S. A. Ragab and U. Piomelli, ASME, FED-Vol. 162, New York, NY, 1993, pp. 81–101.

119. Colucci, P. J., Jaberi, F. A., Givi, P., and Pope, S. B., "Filtered Density Function for Large Eddy Simulation of Turbulent Reacting Flows," *Phys. Fluids*, Vol. 10, No. 2, 1998, pp. 499–515.

120. Jaberi, F. A., Colucci, P. J., James, S., Givi, P., and Pope, S. B., "Filtered Mass Density Function for Large Eddy Simulation of Turbulent Reacting Flows," *J. Fluid Mech.*, Vol. 401, 1999, pp. 85–121.

121. James, S. and Jaberi, F. A., "Large Scale Simulations of Two-Dimensional Nonpremixed Methane Jet Flames," *Combust. Flame*, Vol. 123, 2000, pp. 465–487.

122. Garrick, S. C., Jaberi, F. A., and Givi, P., "Large Eddy Simulation of Scalar Transport in a Turbulent Jet Flow," *Recent Advances in DNS and LES*, edited by D. Knight and L. Sakell, Vol. 54 of *Fluid Mechanics and its Applications*, Kluwer Academic Publishers, The Netherlands, 1999, pp. 155–166.

123. Gicquel, L. Y. M., Givi, P., Jaberi, F. A., and Pope, S. B., "Velocity Filtered Density Function for Large Eddy Simulation of Turbulent Flows," *Phys. Fluids*, Vol. 14, No. 3, 2002, pp. 1196–1213.

124. Sheikhi, M. R. H., Drozda, T. G., Givi, P., and Pope, S. B., "Velocity-Scalar Filtered Density Function for Large Eddy Simulation of Turbulent Flows," *Phys. Fluids*, Vol. 15, No. 8, 2003, pp. 2321–2337.

125. Sheikhi, M. R. H., Givi, P., and Pope, S. B., "Velocity-Scalar Filtered Mass Density Function for Large Eddy Simulation of Turbulent Reacting Flows," *Phys. Fluids*, Vol. 19, No. 9, 2007, pp. 095196 1–21.

126. Sheikhi, M. R. H., Drozda, T. G., Givi, P., Jaberi, F. A., and Pope, S. B., "Large Eddy Simulation of a Turbulent Nonpremixed Piloted Methane Jet Flame (Sandia Flame D)," *Proc. Combust. Inst.*, Vol. 30, 2005, pp. 549–556.

127. Drozda, T. G., Sheikhi, M. R. H., Madnia, C. K., and Givi, P., "Developments in Formulation and Application of the Filtered Density Function," *Flow Turbul. Combust.*, Vol. 78, 2007, pp. 35–67.

128. James, S., Zhu, J., and Anand, M., "Large Eddy Simulations of Turbulent Flames Using the Filtered Density Function Model," *Proc. Combust. Inst.*, Vol. 31, No. 2, 2007, pp. 1737–1745.

129. Drozda, T. G., Wang, G., Sankaran, V., Mayo, J. R., Oefelein, J. C., and Barlow, R. S., "Scalar Filtered Mass Density Functions in Nonpremixed Turbulent Jet Flames," *Combust. Flame*, Vol. 155, No. 1-2, 2008, pp. 54–69.

130. Jones, W. P. and Navarro-Martinez, S., "Large Eddy Simulation of Autoignition with a Subgrid Probability Density Function Method," *Combust. Flame*, Vol. 150, 2007, pp. 170–187.

131. Raman, V. and Pitsch, H., "A Consistent LES/Filtered Density Function Formulation for the Simulation of Turbulent Flames with Detailed Chemistry," *Proc. Combust. Inst.*, Vol. 31, No. 2, 2007, pp. 1711–1719.

132. McDermott, R. and Pope, S. B., "A Particle Formulation for Treating Differential Diffusion in Filtered Density Function Methods," *J. Comput. Phys.*, Vol. 226, No. 1, 2007, pp. 947–993.

133. Chen, J. Y., "A Eulerian PDF Scheme for LES of Nonpremixed Turbulent Combustion with Second-Order Accurate Mixture Fraction," *Combust. Theor. Model.*, Vol. 11, No. 5, 2007, pp. 675–695.

134. Carrara, M. and DesJardin, P., "A Filtered Mass Density Function Approach for Modeling Separated Two-Phase Flows for LES I: Mathematical Formulation," *Int. J. Multiphas. Flow*, Vol. 32, No. 3, 2006, pp. 365–384.

135. Raman, V. and Pitsch, H., "Large-Eddy Simulation of a Bluff-Body-Stabilized Non-Premixed Flame Using a Recursive Filter-Refinement Procedure," *Combust. Flame*, Vol. 142, No. 4, 2005, pp. 329–347.

136. Zhou, X. Y. and Pereira, J. C. F., "Large Eddy Simulation (2D) of a Reacting Plan Mixing Layer Using Filtered Density Function," *Flow Turbul. Combust.*, Vol. 64, 2000, pp. 279–300.

137. Raman, V., Pitsch, H., and Fox, R. O., "Hybrid Large-Eddy Simulation/Lagrangian Filtered-Density-Function Approach for Simulating Turbulent Combustion," *Combust. Flame*, Vol. 143, No. 1-2, 2005, pp. 56–78.

138. Van Vliet, E., Derksen, J. J., and Van Den Akker, H. E. A., "Turbulent Mixing in a Tubular Reactor: Assessment of an FDF/LES Approach," *AIChE J.*, Vol. 51, No. 3, 2005, pp. 725–739.

139. Heinz, S., "On Fokker-Planck Equations for Turbulent Reacting Flows. Part 2. Filter Density Function for Large Eddy Simulation," *Flow Turbul. Combust.*, Vol. 70, No. 1-4, 2003, pp. 153–181.

140. Afshari, A., Jaberi, F. A., and Shih, T. I. P., "Large-Eddy Simulations of Turbulent Flows in an Axisymmetric Dump Combustor," *AIAA J.*, Vol. 46, No. 7, 2008, pp. 1576–1592.

141. Réveillon, J. and Vervisch, L., "Subgrid-Scale Turbulent Micromixing: Dynamic Approach," *AIAA J.*, Vol. 36, No. 3, 1998, pp. 336–341.

142. Cha, C. M. and Troullet, P., "A Subgrid-Scale Mixing Model for Large-Eddy Simulations of Turbulent Reacting Flows Using the Filtered Density Function," *Phys. Fluids*, Vol. 15, No. 6, 2003, pp. 1496–1504.

143. Heinz, S., "Unified Turbulence Models for LES and RANS, FDF and PDF Simulations," *Theor. Comp. Fluid Dyn.*, Vol. 21, 2007, pp. 99–118.

144. Tong, C., "Measurements of Conserved Scalar Filtered Density Function in a Turbulent Jet," *Phys. Fluids*, Vol. 13, No. 10, 2001, pp. 2923–2937.

145. Wang, D. and Tong, C., "Conditionally Filtered Scalar Dissipation, Scalar Diffusion, and Velocity in a Turbulent Jet," *Phys. Fluids*, Vol. 14, No. 7, 2002, pp. 2170–2185.

146. Rajagopalan, A. G. and Tong, C., "Experimental Investigation of Scalar-Scalar-Dissipation Filtered Joint Density Function and its Transport Equation," *Phys. Fluids*, Vol. 15, No. 1, 2003, pp. 227–244.

147. Wang, D. H., Tong, C. N., and Pope, S. B., "Experimental Study of Velocity Filtered Joint Density Function for Large Eddy Simulation," *Phys. Fluids*, Vol. 16, No. 10, 2004, pp. 3599–3613.

148. Wang, D. and Tong, C., "Experimental Study of Velocity-Scalar Filtered Joint Density Function for LES of Turbulent Combustion," *Proc. Combust. Inst.*, Vol. 30, 2005, pp. 567–574.

149. Fox, R. O., *Computational Models for Turbulent Reacting Flows*, Cambridge University Press, Cambridge, UK, 2003.

150. Heinz, S., "On Fokker-Planck Equations for Turbulent Reacting Flows. Part 1. Probability Density Function for Reynolds-Averaged Navier-Stokes Equations," *Flow Turbul. Combust.*, Vol. 70, No. 1-4, 2003, pp. 115–152.

151. Madnia, C. K., Jaberi, F. A., , and Givi, P., "Large Eddy Simulation of Heat and Mass Transport in Turbulent Flows," *Handbook of Numerical Heat Transfer*, edited by W. J. Minkowycz, E. M. Sparrow, and J. Y. Murthy, chap. 5, John Wiley & Sons, Inc., New York, NY, 2nd ed., 2006, pp. 167–189.

152. Givi, P., Sheikhi, M. R. H., Drozda, T. G., and Madnia, C. K., "Large Scale Simulation of Turbulent Combustion," *Combust. Plasma Chem.*, Vol. 6, No. 1, 2008, pp. 1–9.

153. Drummond, J. P., "Two-Dimensional Numerical Simulation of a Supersonic, Chemically Reacting Mixing Layer," NASA TM 4055, 1988.

154. Cutler, A. D., Danehy, P. M., Springer, R. R., O'Byrne, S., and Caprioti, D. P., "Coherent Anti-Stokes Raman Spectroscopic Thermometry in a Supersonic Combustor," *AIAA J.*, Vol. 41, No. 12, 2003, pp. 2451–2459.

155. Cutler, A. D., Diskin, G. S., Drummond, J. P., and White, J. A., "Supersonic Coaxial Jet Experiment for Computational Fluid Dynamics Code Validation," *AIAA J.*, Vol. 44, No. 3, 2006, pp. 585–592.

156. O'Brien, E. E., "The Probability Density Function (PDF) Approach to Reacting Turbulent Flows," *Turbulent Reacting Flows*, edited by P. A. Libby and F. A. Williams, Vol. 44 of *Topics in Applied Physics*, chap. 5, Springer-Verlag, Heidelberg, 1980, pp. 185–218.

157. Vreman, B., Geurts, B., and Kuerten, H., "Realizability Conditions for the Turbulent Stress Tensor in Large-Eddy Simulation," *J. Fluid Mech.*, Vol. 278, 1994, pp. 351–362.

158. Pope, S. B., "PDF Methods for Turbulent Reactive Flows," *Prog. Energy Combust. Sci.*, Vol. 11, 1985, pp. 119–192.

159. Karlin, S. and Taylor, H. M., *A Second Course in Stochastic Processes*, Academic Press, New York, NY, 1981.

160. Wax, N., *Selected Papers on Noise and Stochastic Processes*, Dover, New York, NY, 1954.

161. Gardiner, C. W., *Handbook of Stochastic Methods for Physics, Chemistry and the Natural Sciences*, Springer-Verlag, 2nd ed., 1990.

162. Haworth, D. C. and Pope, S. B., "A Generalized Langevin Model for Turbulent Flows," *Phys. Fluids*, Vol. 29, No. 2, 1986, pp. 387–405.

163. Dreeben, T. D. and Pope, S. B., "Probability Density Function and Reynolds-Stress Modeling of Near-Wall Turbulent Flows," *Phys. Fluids*, Vol. 9, No. 1, 1997, pp. 154–163.

164. Delarue, B. J. and Pope, S. B., "Application of PDF Methods to Compressible Turbulent Flows," *Phys. Fluids*, Vol. 9, No. 9, 1997, pp. 2704–2715.

165. Erlebacher, G., Hussaini, M. Y., Speziale, C. G., and Zang, T. A., "Toward the Large Eddy Simulation of Compressible Turbulent Flows," *J. Fluid Mech.*, Vol. 238, 1992, pp. 155–185.

166. Scotti, A., Meneveau, C., and Lilly, D. K., "Generalized Smagorinsky Model for Anisotropic Grids," *Phys. Fluids A*, Vol. 5, No. 9, 1993, pp. 2306–2308.

167. Yoshizawa, A., "Statistical Theory for Compressible Turbulent Shear Flows, with the Application to Subgrid Modeling," *Phys. Fluids*, Vol. 29, No. 7, 1986, pp. 2152–2164.

168. Eidson, T. M., "Numerical Simulation of the Turbulent Rayleigh-Benard Problem using Subgrid Modelling," *J. Fluid Mech.*, Vol. 158, 1985, pp. 245–268.

169. Cutler, A. D. and White, J. A., "An Experimental and CFD Study of a Supersonic Coaxial Jet," AIAA Paper 2001-0143, Jan. 2001.

170. Cutler, A. D., Diskin, G. S., Danehy, P. M., and Drummond, J. P., "Fundamental Mixing and Combustion Experiments for Propelled Hypersonic Flight," AIAA Paper 2002-3879, July 2002.

171. Ho, C. M. and Huerre, P., "Perturbed Free Shear Layers," *Ann. Rev. Fluid Mech.*, Vol. 16, 1984, pp. 365–424.

172. Drummond, J. P., "Supersonic Reacting Internal Flow Fields," *Numerical Approaches to Combustion Modeling*, edited by E. S. Oran and J. P. Boris, Vol. 135 of *Progress in Astronautics and Aeronautics*, chap. 12, AIAA Publishing Co., Washington, D.C., 1991, pp. 365–420.

173. Moin, P., Squires, K., Cabot, W., and Lee, S., "A Dynamic Subgrid-Scale Model for Compressible Turbulence and Scalar Transport," *Phys. Fluids A*, Vol. 3, No. 11, 1991, pp. 2746–2757.

174. Speziale, C. G., Erlebacher, G., Zang, T. A., and Hussaini, M. Y., "The Subgrid-Scale Modeling of Compressible Turbulence," *Phys. Fluids*, Vol. 31, No. 4, 1988, pp. 940–942.

175. Rizzetta, D. P. and Visbal, M. R., "Large-eddy Simulation of Supersonic Boundary-layer Flow by a High-order Method," *Int. J. Comput. Fluid D.*, Vol. 18, No. 1, 2004, pp. 15–27.

REPORT DOCUMENTATION PAGE

Form Approved
OMB No. 0704-0188

1. REPORT DATE *(DD-MM-YYYY)*	2. REPORT TYPE	3. DATES COVERED *(From - To)*
01- 06 - 2009	Technical Memorandum	

4. TITLE AND SUBTITLE

Development of Methods to Predict the Effects of Test Media in Ground-Based Propulsion Testing

5a. CONTRACT NUMBER

5b. GRANT NUMBER

5c. PROGRAM ELEMENT NUMBER

6. AUTHOR(S)

Drummond, J. Philip; Danehy, Paul M.; Gaffney, Richard L., Jr.; Parker, Peter A.; Tedder, Sarah A.; Chelliah, Harsha K.; Cutler, Andrew D.; Bivolaru, Daniel; Givi, Peyman; Hassan, Hassan A.

5d. PROJECT NUMBER

5e. TASK NUMBER

5f. WORK UNIT NUMBER

599489.02.07.07.03.02.01

7. PERFORMING ORGANIZATION NAME(S) AND ADDRESS(ES)

NASA Langley Research Center
Hampton, VA 23681-2199

8. PERFORMING ORGANIZATION REPORT NUMBER

L-19662

9. SPONSORING/MONITORING AGENCY NAME(S) AND ADDRESS(ES)

National Aeronautics and Space Administration
Washington, DC 20546-0001

10. SPONSOR/MONITOR'S ACRONYM(S)

NASA

11. SPONSOR/MONITOR'S REPORT NUMBER(S)

NASA/TM-2009-215766

12. DISTRIBUTION/AVAILABILITY STATEMENT

Unclassified - Unlimited
Subject Category 34
Availability: NASA CASI (443) 757-5802

13. SUPPLEMENTARY NOTES

14. ABSTRACT

This report discusses work that began in mid-2004 sponsored by the Office of the Secretary of Defense (OSD) Test & Evaluation/Science & Technology (T&E/S&T) Program. The work was undertaken to improve the state of the art of CFD capabilities for predicting the effects of the test media on the flameholding characteristics in scramjet engines. The program had several components including the development of advanced algorithms and models for simulating engine flowpaths as well as a fundamental experimental and diagnostic development effort to support the formulation and validation of the mathematical models. This report provides details of the completed work, involving the development of phenomenological models for Reynolds averaged Navier-Stokes codes, large-eddy simulation techniques and reduced-kinetics models. Experiments that provided data for the modeling efforts are also described, along with the associated nonintrusive diagnostics used to collect the data.

15. SUBJECT TERMS

Fluid mechanics; Combustion; Kinetics; Facility testing; Computational fluid dynamics

16. SECURITY CLASSIFICATION OF:			17. LIMITATION OF ABSTRACT	18. NUMBER OF PAGES	19a. NAME OF RESPONSIBLE PERSON
a. REPORT	b. ABSTRACT	c. THIS PAGE			STI Help Desk (email: help@sti.nasa.gov)
					19b. TELEPHONE NUMBER *(Include area code)*
U	U	U	UU	111	(443) 757-5802